First star signatures on high-z GRBs and DLAs

Qingbo Ma

München 2017

First star signatures on high-z GRBs and DLAs

Qingbo Ma

Dissertation
an der Fakultät für Physik
der Ludwig–Maximilians–Universität
München

vorgelegt von
Qingbo Ma
aus Henan, China

München, den 13.03.2017

Erstgutachter: Prof. Dr. Simon WHITE
Zweitgutachter: Prof. Dr. Gerhard BÖRNER
Tag der mündlichen Prüfung: 21.07.2017

Contents

List of Figures

List of Tables

Zusammenfassung

Am Ende des dunklen Zeitalters des Universums entstanden die ersten Sterne. Sie brachten das erste Licht und die ersten Metalle in das Universum. Es gibt seit langem theoretische Vorhersagen dieses Vorgangs, aber bisher keine direkten Beobachtungen davon. In dieser Arbeit untersuche ich Spuren der ersten Sterne in Gamma-ray Bursts von Population-II-Sternen (GRBIIs) bei hohen Rotverschiebungen, sowie in Damped Lymanα-Absorbern (DLAs). Dafür verwende ich numerische N-body/hydrodynamische Simulationen mit Modellen für atomare und molekulare Kühlungsprozesse, sowie für Sternentstehung und Metallanreicherung durch stellare Populationen mit verschiedenen ursprünglichen Massenfunktionen.

Zuerst verwende ich eine Simulation basierend auf einem Modell mit sehr massiven ersten Sternen ($m_* = [100, 500]\,\mathrm{M}_\odot$) um GRBIIs zu untersuchen, die sich in einem von den ersten Sternen angereicherten Medium befinden (PopIII-dominiert). Die Ergebnisse zeigen, dass ein großer Anteil der GRBIIs bei hohen Rotverschiebungen PopIII-dominiert ist, z.B. $\sim$10% bei $z = 10$, aber dass dieser Anteil mit sinkender Rotverschiebung schnell abnimmt, z.B. nur $\sim$1% bei $z = 6$.

Dann untersuche ich ob es möglich ist verschiedene Modelle für die ersten Sterne mit Hilfe von Beobachtungen von GRBs bei hohen Rotverschiebungen zu unterscheiden, indem ich drei Simulationen mit verschiedenen Massenbereichen und den dazugehörigen Lebensdauern und Metallproduktionsraten der ersten Sterne vergleiche. Es ergibt sich, dass der Anteil an GRBs, der PopIII-dominiert ist, unabhängig von den Modellen für die ersten Sterne ist. Gleichermaßen befinden sich PopIII-dominierte GRBIIs meistens in Galaxien mit niedriger Metallizität, Sternentstehungsrate und stellarer Masse. Aufgrund der speziellen Metallproduktionsraten von metallfreien Sternen könnten die Signale erster Sterne mit Hilfe von Häufigkeitsverhältnissen verschiedener Metalle identifiziert werden, die sich aus den Absorptionslinien der GRBII afterglow-Spektren ableiten lassen. So würden beispielsweise die Relationen [Si/O] gegen [C/O] oder [Fe/C] gegen [Si/C] es ermöglichen, Spuren von massiven und sehr massiven ersten Sternen zu unterscheiden. Allerdings zeigen die bisher beobachteten GRBs bei hohen Rotverschiebungen, z.B. GRB 130606A bei $z = 5.91$ und GRB 111008A bei $z = 5.0$, keine offensichtlichen Metallspuren von ersten Sternen. Das ist konsistent mit dem kleinen Anteil an PopIII-dominierten GRBs in diesem Rotverschiebungsbereich.

Außerdem untersuche ich die Spuren der ersten Sterne in DLAs bei hohen Rotverschiebungen und analysiere, wie sich die Beobachtungen von DLAs dazu nutzen lassen,

die Modelle erster Sterne einzugrenzen. Da DLAs sich durch sehr hohe Dichten neutralen Wasserstoffs, sowie niedrige Gastemperaturen und Ionisationsraten auszeichen, könnte ein großer Anteil von ihnen bei $z > 5.5$ Spuren der ersten Sterne enthalten. In meinen Simulationen finde ich, dass $\sim 40\%$ der DLAs solche Spuren enthalten, wenn sie als Galaxien mit Temperaturen $< 10^4\,\mathrm{K}$ ausgewählt werden, während der Anteil auf $\sim 3\%$ sinkt, wenn die DLAs auf Basis des Wirkungsquerschnitts neutralen Wasserstoffs definiert sind. Durch Vergleich der Simulationsergebnisse mit aktuellen Beobachtungen ergibt sich, dass bei $z > 5$ beobachtete DLAs konsistenter mit einem Modell sind, in dem die ersten Sterne Massen im Bereich $m_* = [0.1, 100]\,\mathrm{M}_\odot$ haben, als mit einem Modell mit sehr massiven ersten Sternen. Allerdings sind diese Ergebnisse nicht endgültig und enthalten noch einige Unsicherheiten.

Summary

First stars were born after the dark age era of the Universe. They produced the first light and metal pollution in the Universe. This was predicted in theory a long time ago, but no direct observation is available. In this thesis I study the first star signatures in high-z Gamma-ray Bursts from Population II stars (GRBIIs) and in Damped Lymanα Absorbers (DLAs), using numerical N-body/hydrodynamic simulations that include atomic and molecular cooling, star formation and metal enrichment from stellar populations with different initial mass functions.

I first use one simulation based on a very massive first star model ($m_* = [100, 500]\,\mathrm{M}_\odot$) to study the GRBIIs hosted in a medium enriched by first stars (PopIII-dominated). I find that a high fraction of high-z GRBIIs are PopIII-dominated, e.g. $\sim$10% at $z = 10$, but this fraction decreases quickly with redshift, e.g. only $\sim$1% at $z = 6$. Then I study the possibility to distinguish different first star models using observations of high-z GRBs by running three simulations with different mass ranges and the corresponding lifetimes and metal yields for first stars. I find that the fraction of GRBs that are PopIII-dominated is independent from the first star models. Similarly, PopIII-dominated GRBIIs are mostly hosted in galaxies with low metallicity, star formation rate and stellar mass. Because of the special metal yields of metal-free stars, the first star signals could be identified with the metal abundance ratios derived from the absorption lines in the GRBII afterglow spectra, e.g. the [Si/O] vs [C/O] or [Fe/C] vs [Si/C] would distinguish an imprint from very massive and massive first stars. However, the currently observed high-z GRBs, e.g. GRB 130606A at $z = 5.91$ and GRB 111008A at $z = 5.0$, do not display obvious metal features from first stars, which is also consistent with the low fraction of PopIII-dominated GRBs in this redshift range. I also study the imprint of first stars on high-z DLAs, and explore how to use the observations of DLAs to constrain the first star models. Since DLAs are characterized by very high neutral hydrogen density, low gas temperature and ionization fraction, a high fraction of DLAs at $z > 5.5$ could contain first stars signatures. From my simulations, I find that $\sim$ 40% of DLAs contain such imprint if they are selected as galaxies with temperature $< 10^4$ K, while the percentage drops to $\sim$ 3% if DLAs are defined based on the cross-section of neutral hydrogen. By comparing the simulation results with current observations, I find that DLAs observed at $z > 5$ are more consistent with a model in which the first stars have a mass in the range $m_* = [0.1, 100]\,\mathrm{M}_\odot$, rather than one with very massive first stars, although the comparison is not conclusive and still subject to some uncertainty.

Chapter 1

Introduction

In the last century, humans went through an era of quickly growing of science and technology. With the help of modern techniques developed, astronomical research is much easier and more precise. It results in abundant achievements in the astronomy, from the field of cosmology to planetary science. Specifically, with the bigger and bigger telescopes built on the ground, people can observe more and more objects on the sky. Many very distant, faint and strange objects are discovered, that never happened before. With the developing of rocket technology, people also send the telescopes into outer space, and observe the sky with a better view. The bigger rockets carry detectors and analyzers further away from earth, allowing to explore the celestial bodies directly e.g Moon, Mars and comets. Thanks to the development of supercomputers, people now can precisely simulate and study the universe even without a direct observation. Together with the developing of analytical skills, supercomputers also help to analyse the numerous data from astronomical observations. With these technological innovations, people have built standard models of cosmology, galaxy formation and stellar evolution, found extrasolar planets, detected gravitational waves and so on.

To avoid being lost in the sea of abundant astronomical knowledge and new discoveries, in this chapter I will briefly introduce the modern cosmological model and the structure formation, then I will focus on the recent study about the first stars (also referred to as PopIII stars) in the very early Universe, and the possible ways to detect them.

1.1 Cosmological Model

Thousands of years ago, without too much scientific knowledge, ancient Chinese believed that our Universe was born like an egg full of gas and dust, until one day the god called "Pangu" separated them with an axe, then dust formed the earth and gas formed the sky. After that, he died and created everything on earth using his body. Although it is not scientific, this ancient cosmological model actually solved many questions of our ancestors.

Modern astronomy was started five hundred years ago, after Nicolas Copernicus published his book, *On the Revolutions of the Heavenly Spheres*, before his death, that claimed

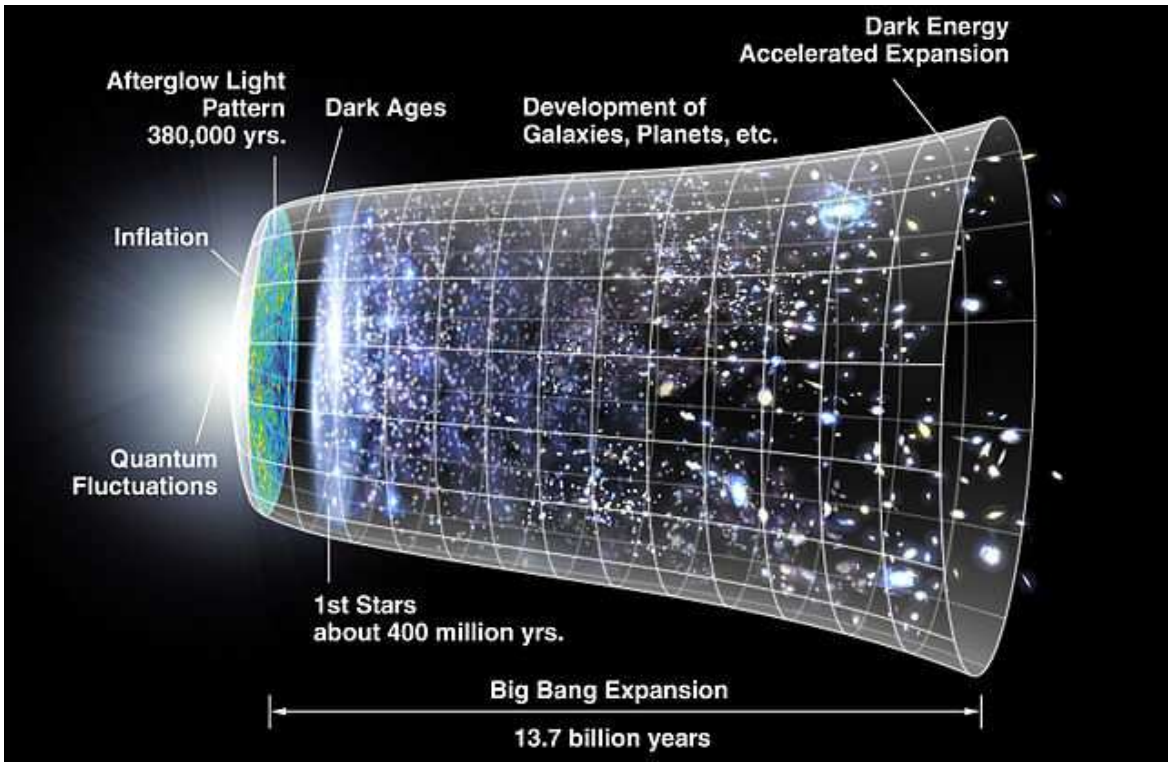

Figure 1.1: A timeline of the Universe over 13.7 billion years. The left white spot denotes the big bang, starting with the quantum fluctuations. Then the Universe underwent the inflation. The earliest moment we can now observe is the afterglow light pattern at 380,000 years, i.e. the CMB radiation. After a short period of dark ages, the first stars and galaxies started to form. The next several billion years are the era of development of galaxies and stars. In the more recent moment, we observed that the expansion of Universe sped up again due to the dark energy.
Credit: NASA/WMAP Science Team.

that the Sun must be the center of the Universe and the earth is just one planet of solar system. Although the theory is still wrong, it was the first time that humans studied the Universe with a scientific method. After that, astronomy grew up quickly, going from our solar system to the Milky Way and even further away. Modern cosmology originated from the development of the general theory of relativity by Albert Einstein in 1915, and some observational discoveries in the 1920s that show an expanding Universe. Now, the most popular cosmological model is the Big Bang theory established by Georges Lemaitre, and the ΛCDM model is the most well-known and accepted version.

In Fig. 1.1, I show a diagram from NASA/WMAP that describes the history of universe within the Big Bang theory, based on the ΛCDM model. In this theory, the Universe began with a big bang that happened ~ 13.7 billion years ago, although the origin of the big bang is still not clear now. Then the Universe underwent a period of inflation that produced a burst of exponential growth of the cosmic volume. With the inflation, the Universe also

cooled itself down and formed the basic elements e.g. protons, electrons, neutrons, and neutrino. 380,000 years later, i.e. at redshift $z \sim 1100$, the Universe was cold enough for the recombination of nuclei and electrons to form atoms, and then the light decoupled from the baryonic matter and fled to the space. The remnant light is still visible now, known as cosmic microwave background radiation (CMB). After that, the Universe was full of hydrogen, helium and a little lithium, but no heavy metal elements, no stars and galaxies, and no light were produced. This era is known as the dark ages. Meanwhile, with the self-gravity of matter, cosmic structures begin to form. When the Universe was about 400 million years old, the first star was formed in minihalos. The rising of the first stars, that produced abundant ionizing photons and heavy chemical elements, lights the Universe again, and transforms the early simple Universe into the modern, complex one. Together with the continuing growth of structures, more stars and galaxies are formed. Then the X-ray and UV photons from stars and accreting black holes started to reionize the Universe, until it was fully ionized at $z > 5$, $\sim$1 billion years later after the big bang. Then the Universe continued to expand, and more and more stars and galaxies were formed.

In the ΛCDM model, the expanding rate of the Universe after recombination is described by the time-dependent Hubble parameter $H(t)$ that is defined as:

$$H \equiv \frac{\dot{a}}{a} = H_0 \sqrt{\Omega_m a^{-3} + \Omega_\Lambda} \tag{1.1}$$

where $a = 1/(1+z)$ is the cosmic scale factor, $\dot{a} = \mathrm{d}a/\mathrm{d}t$, H_0 is the Hubble constant at redshift $z = 0$, $\Omega_m \approx 0.3$ and $\Omega_\Lambda \approx 0.7$ denote the matter and dark energy density respectively. From eq. 1.1, the expansion of the Universe at early times was dominated by matter, both in its baryonic and dark form, while in the near local Universe, the matter contribution became much lower than the dark energy, then the expansion is dominated by dark energy. Because of the negative pressure of dark energy, the Universe has an accelerated expansion now.

The big bang theory and ΛCDM model have been proved by many measurements, e.g. the CMB power spectrum, the ratio of hydrogen and helium in the total baryonic matter, the large scale structure, and the accelerated expansion has been proved with the surveys of Type Ia supernovae.

1.2 Structure Formation

The formation of cosmic structure was originated from the quantum fluctuations in the big bang. With the fast growth of the scale factor during inflation, the small fluctuations were frozen in, and then reentered the horizon after the inflation. Theoretically, the relation of current matter distribution with primordial fluctuations can be described in Fourier space as (see details in Dodelson, 2003):

$$\delta(\vec{k}, a) = \frac{3}{5} \frac{k^2}{\Omega_m H_0^2} \Phi_\mathrm{p}(\vec{k}) T(k) D(a) \tag{1.2}$$

where k denotes the wave number in Fourier space, $\Phi_{\rm p}$ is the primordial potential set up during inflation, $T(k)$ is the transfer function that describes the evolution of perturbations through the epochs of horizon crossing and radiation/matter transition, and $D(a)$ is the growth function that describes the evolution after the transfer function regime.

In the inflation theory, $\Phi_{\rm p}(\vec{k})$ is described as a Gaussian distribution with a mean value zero, and its power spectra can be conventionally described as (Dodelson, 2003):

$$P_\Phi(k) = \frac{50\pi^2}{9k^3}(\frac{k}{H_0})^{n-1}\delta_H^2(\frac{\Omega_m}{D(a=1)})^2 \tag{1.3}$$

where δ_H indicates the amplitude of perturbation at horizon crossing, n is the spectral index ($n = 1$ corresponds to a scale-free scalar spectrum), and $D(a = 1)$ is the growth factor at $z = 0$.

Fluctuations that entered the horizon before the equality of matter and radiation, would have their amplitude strongly reduced by the radiation field. However, fluctuations at very large scale, that entered the horizon after the decoupling of matter and radiation, could still keep their original form. Because of the mixed process for the perturbations crossing horizon and the transition of radiation and matter, the transfer function T is a complicated function of wave number k. One available fitting form for the exact solution is (Bardeen et al., 1986):

$$T(x \equiv k/k_{\rm eq}) = \frac{ln(1+0.171x)}{0.171x}[1+0.284x+(1.18x)^2+(0.399x)^3+(0.490x)^4]^{-0.25} \tag{1.4}$$

where $k_{\rm eq}$ is the wave number of the mode entering horizon at the time of equality of radiation and matter. When $k \ll k_{\rm eq}$, $T(K) \propto 1$ indicates that the large scale structure of primordial perturbations would be retained after the transfer. If $k \gg k_{\rm eq}$, $T(K) \propto 1/k^2$ means the small scale perturbations would be reduced by a factor $1/k^2$.

After all the modes entered the horizon, the fluctuations would not be smoothed out and all modes evolve identically, thanks to the zero pressure of cold, dark matter. Thus the growth function is a function of scale factor a, which is expressed as (Dodelson, 2003):

$$D(a) = \frac{5\Omega_m}{2}\frac{H(a)}{H_0}\int_0^a \frac{{\rm d}a'}{(a'H(a')/H_0)^3}. \tag{1.5}$$

This equation is also available when considering the dark energy, that leads to a different Hubble constant from eq. 1.1.

With the primordial power spectrum, $T(k)$ and $D(a)$, one could compute the power spectrum of matter distribution, defined as $P(k) \equiv 1/(2\pi)^3 < \delta(\vec{k})\delta_*(\vec{k}) >$. By combing eq. 1.3, 1.4 and 1.5, it is not difficult to find that the matter power spectrum $P(k)$ is $\propto k$ at large scale, but $\propto k^{-3}$ at small scale. However, the non-linear evolution caused by the self-gravity would increase the small scale perturbations, which is very important in the local Universe.

When the density of a peak region caused by perturbation is high enough, the matter will collapse to form halos. In a Gaussian field, the expected mass fluctuations for a given

scale, i.e. the halo with mass M, is characterised by the power spectrum $P(k)$:

$$\sigma^2(M,a) = \int \Delta^2(k,a)(W(kR)k)^2 \mathrm{d}k \tag{1.6}$$

where $\Delta(k,a) = k^3P(k,a)/(2\pi^2)$ indicates the dimensionless power spectrum, and $W(kR)$ is the Fourier transfer of the filtering function. In the case of top hat filtering in real space, $W(kR) = 3[\sin(kR) - kR\cos(kR)]/(kR)^3$, where R is the smoothing radius corresponding to the halo mass $M \equiv 4\pi/3R^3\bar{\rho}$, and $\bar{\rho}$ is the cosmic mean density. Then the galaxy mass function could be expressed with a Press-Schetchter (PS) formalism (Press & Schechter, 1974):

$$n(M,t)\mathrm{d}M = \sqrt{\frac{2}{\pi}}\frac{\delta_\mathrm{c}\bar{\rho}}{\sigma M^2}\exp(-\frac{\delta_c^2}{2\sigma^2})\Big|\frac{\mathrm{d}\ln\sigma}{\mathrm{d}\ln M}\Big|\mathrm{d}M \tag{1.7}$$

where $n(M,t)$ denotes the galaxy number in the range $M \to M + \mathrm{d}M$, and $\delta_\mathrm{c} = 1.69$ is the critical density that allows a region collapsing into a halo.

The evolution of structure and galaxy formation are better studied with numerical simulations (e.g. Springel et al., 2006; Schaye et al., 2015), that give results much closer to observations of the real universe.

1.3 Star Formation

With the growing of halos, the baryon material would fall within the halos because of the strong potential of gravity, and form gas clouds. Once the gas is dense enough, molecular and atomic (also metal, once the gas has been polluted) cooling would lower its temperature, allowing the cloud to further collapse and form stars. In this section, I will firstly introduce the modeling of star formation in simulations, and then review the recent progress made in the investigation of high-z Star Formation Rate (SFR), both from simulations and observations.

1.3.1 Modeling star formation

Because of the poor understanding of the complex processes in molecular clouds that form stars, star formation in cosmological simulations is usually computed with empirical star formation laws, e.g. the theoretical Schmidt law (Schmidt, 1959), in which SFR $\propto \rho_\mathrm{g}^{n_\mathrm{s}}$ if $\rho_\mathrm{g} > \rho_\mathrm{c}$ and SFR $= 0$ if $\rho_\mathrm{g} < \rho_\mathrm{c}$, where ρ_g indicates the volume density of gas particles, ρ_c is a threshold density for star formation, and n_s is the power-law index of the Schmidt law. One common form adopted in numerical simulations of galaxy formation (e.g. Marri & White, 2003) is:

$$\dot{m}_* = \frac{x \times m_\mathrm{g}}{\tau_*} \tag{1.8}$$

where $\dot{m}_*$ indicates the star mass formed per unit time in the gas particle, m_g is the mass of gas particle, x (with typical value ≈ 0.1) is the gas fraction converted into stars and τ_*

denotes the star formation time scale. Since $\tau_* \propto \rho_{\rm g}^{-0.5}$, SFR $\propto \rho_{\rm g}^{1.5}$, i.e with a Schmidt law index $n_{\rm s} = 1.5$.

Alternatively, the Kennicutt−Schmidt (KS) law is also widely used in numerical simulations. It is a relation between the SFR per unit area ($\dot{\Sigma}_*$) and the gas surface density ($\Sigma_{\rm g}$) obtained from observations of nearby galaxies:

$$\dot{\Sigma}_* = \begin{cases} 0 & \text{if } \Sigma_{\rm g} < \Sigma_{\rm c} \\ A(\Sigma_{\rm g}/(1\,{\rm M}_\odot\,{\rm pc}^{-2}))^{\rm n_{ks}} & \text{if } \Sigma_{\rm g} > \Sigma_{\rm c} \end{cases} \tag{1.9}$$

where A is a constant factor, $\rm M_\odot$ indicates the mass of the Sun, Σ_c is the threshold surface density for star formation, and $n_{\rm ks}$ denotes the index of the KS law. Caused by its self-gravity, the density of the gas cloud will fluctuate around the local Jeans scale, i.e. $\Sigma_{\rm g} \approx \Sigma_{\rm g,J} \propto (P_{\rm tot})^{1/2}$, where $P_{\rm tot}$ is the total pressure of the gas cloud. Thus the typical time scale τ_* for star formation $\propto \Sigma_g/\dot{\Sigma}_* \propto P_{\rm tot}^{(1-n_{\rm ks})/2}$. Then the SFR of a gas particle can be described as $\dot{m}_* \propto m_{\rm g}/\tau_* \propto m_{\rm g} P_{\rm tot}^{(n_{\rm ks}-1)/2}$, that relates to the mass of the gas particle and to the gas pressure (see more details in Schaye & Dalla Vecchia, 2008). Because this approach is directly related to the observed KS law and has no dependence on the specific equation of state of star forming gas, it is commonly used in the EAGLE (e.g. Rahmati et al., 2016) and APOSTLE (Starkenburg et al., 2017) simulations.

Considering that the unstable clouds might collapse to form stars on a very short, some simulations only take care of the total stellar mass formed when star formation happened in a gas particle, e.g. forming a star particle of mass $x \times m_{\rm g}$ (e.g. Booth et al., 2007; Wise & Abel, 2008; Wise et al., 2012), or randomly generating star particles with mass $m_{\rm g}/N_*$ from a probability function (Tornatore et al., 2007a):

$$p = N_*[1 - \exp(-\frac{x\Delta\tau}{\tau_*})], \tag{1.10}$$

where N_* is the number of stellar generations, which is set to 3 in Tornatore et al. (2007a). The SFR then be computed with eq. 1.8. This approach is convenient to follow the stellar evolution and the transition from PopIII to PopII star formation (Maio et al., 2010; Wise et al., 2012), and it is the method which is used in my thesis.

1.3.2 SFR from simulations

The cosmic SFR has been studied in many hydrodynamical simulations. As an example, in Fig. 1.2 I show the SFR density from Campisi et al. (2011), including the total SFR and the PopIII SFR, as obtained from simulations with different comoving sides. From Fig. 1.2, the PopIII SFR is much lower than the PopII/I SFR, as a result of the lower efficiency of molecular hydrogen cooling in the metal-free medium in comparison to that of metal cooling in a metal-rich medium. Indeed, the PopII/I star formation quickly dominates the cosmic SFR after a very short PopIII phase (Maio et al., 2010; Xu et al., 2013), since the metal enrichment from PopIII stars is very efficient and thus the transition from PopIII to

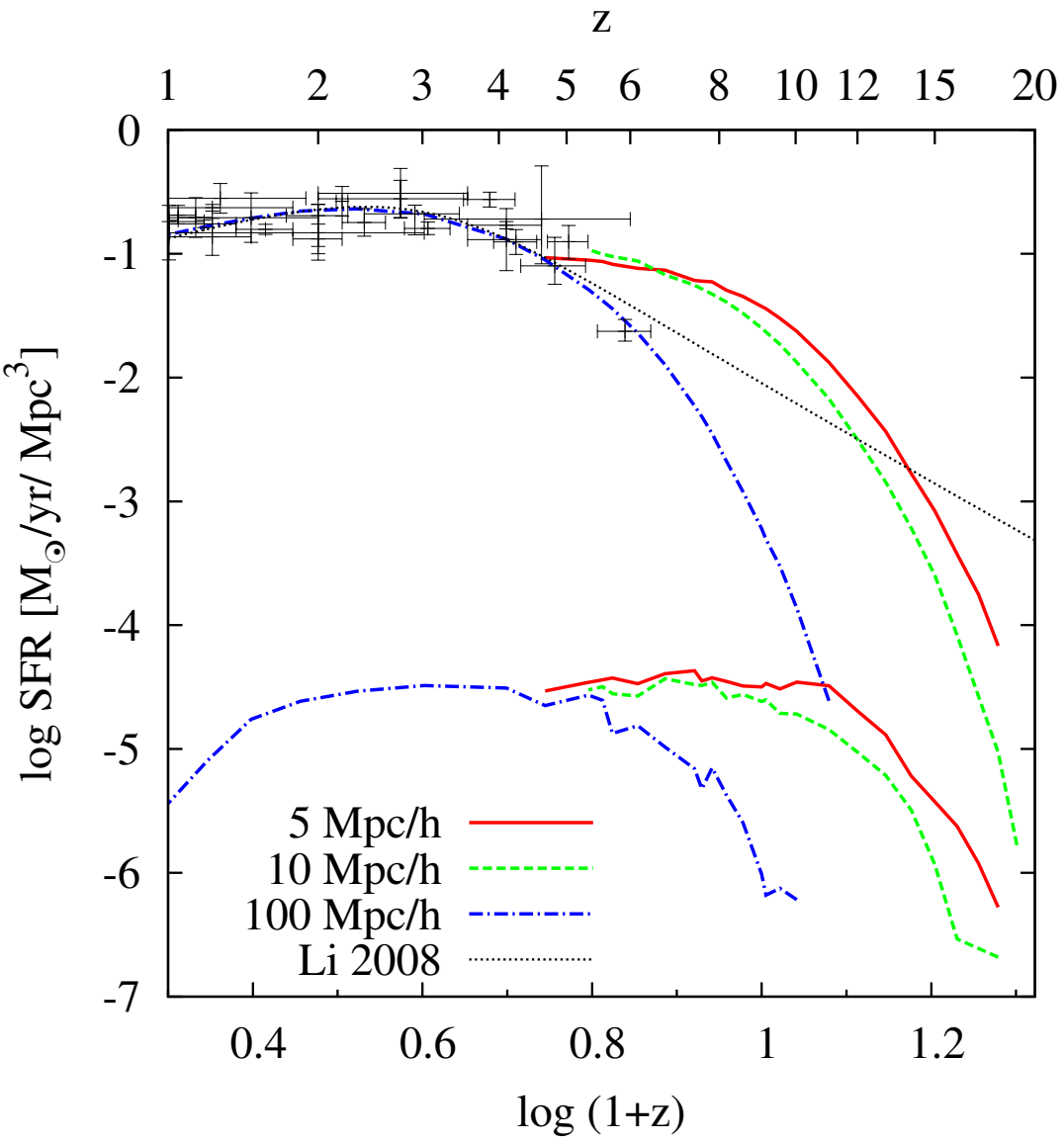

Figure 1.2: SFR density as a function of redshift from simulations with different comoving sides: $5\,\mathrm{Mpc}\,h^1$ (red solid line), $10\,\mathrm{Mpc}\,h^1$ (green dashed line) and $100\,\mathrm{Mpc}\,h^1$ (blue dotâĂŞdashed line). The upper lines indicate the total SFR density, and bottom lines denote the PopIII SFR. Symbols with error bars show the observational data, with the best fit as black dotted line.
Credit: Fig. 1 in Campisi et al. (2011).

PopII is very fast (Campisi et al., 2011). Besides, the SFR in the simulations is sensitive to the resolution of the simulation box. A higher resolution leads to a higher SFR density, because of the limited capabilities of the bigger SPH particles to condense, cool and then collapse (Maio et al., 2010). However, Fig. 1.2 shows that the SFR in different simulations converges at low redshift. Their simulated SFR are comparable with observations at $z < 6$.

From the literature, the SFR of first stars is also affected by several factors that might have little effects on PopII/I SFR. For example, the first star model significantly changes the PopIII SFR, e.g. in the case of a very massive first star model the PopIII SFR is much lower than that of a small mass first star model (Maio et al., 2010), since the more massive stars have shorter lifetimes but stronger supernovae explosions that would efficiently enrich the medium. The PopIII SFR is also affected by the uncertainties on the critical metallicity of the transition from PopIII to PopII/I stars (Maio et al., 2010). Different dark matter models could produce different environments for the star formation and thus the PopIII SFR would be different, e.g. the SFR of first stars under the warm dark matter (WDM) model is much lower than that of cold dark matter (CDM) model (Maio & Viel, 2015). The supersonic coherent baryonic flows originated from the cosmic recombination era reduce the gas mass in minihalos and thus delay the formation of the first stars and reduce the associated SFR (Tseliakhovich & Hirata, 2010). This effect is very sensitive to the strength of the velocity shift between dark matter and baryonic gas (Maio et al., 2011; Naoz et al., 2012). Finally, the heating of X-ray photons from very early first stars could suppress the following PopIII star formation by increasing the Jeans mass in minihalos, while the electron fraction increased by ionization from X-ray photons would promote H^2 formation via the catalyst H^- and thus increase the PopIII star formation. Considering these two opposite effects of the X-ray radiation, Ricotti (2016) found that the hypernovae explosion of intermediate PopIII stars with mass $\sim 20 - 40\,M_\odot$ would produce the largest number of PopIII stars.

1.3.3 SFR from observations

As the luminosity of young stars is dominated by the Ultraviolet (UV) emission from massive stars, the SFR in a star forming cloud has a simple relation with the UV luminosity $L_{\rm UV}$ (Madau & Dickinson, 2014):

$$\mathrm{SFR}_{\rm UV} = \kappa_{\rm UV} \times L_{\rm UV} \tag{1.11}$$

where $\kappa_{\rm UV}$ is the conversion factor from UV luminosity to SFR, which depends on the metal-enrichment history and the IMF. With the help of UV surveys, the observation of cosmic SFR has been extended to very high redshift, e.g. up to $z \sim 11$ (Coe et al., 2013; Bouwens et al., 2014, 2015). Nevertheless, because of the strong absorption of UV photons by dust, the SFR estimated from UV luminosity should be dust corrected (Duncan et al., 2014).

Since the UV photons absorbed by dust are re-radiated at infrared (IR) wavelength, IR survey is another important tool to measure the high-z SFR. Similar to eq. 1.11, the

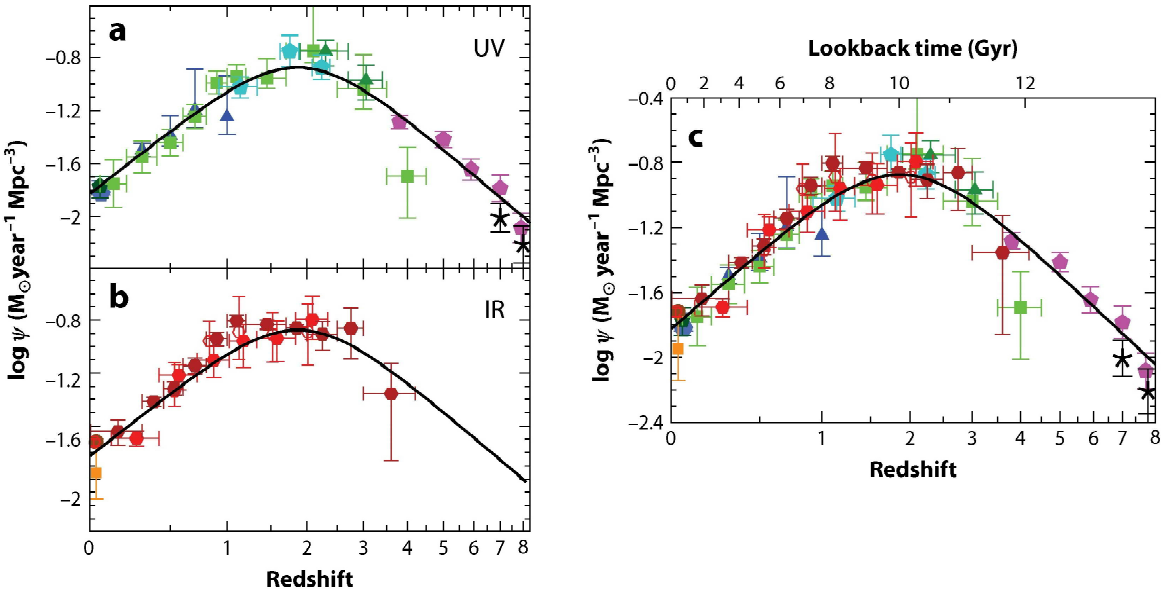

Figure 1.3: Star formation history obtained from measurements of the galaxy luminosity in the rest-frame (a) far-ultraviolet (FUV), (b) infrared (IR), and (c) FUV+IR.
The SFR from UV measurements are already dust corrected. The data points with different color and symbols denote the SFR measurements in the literature that are listed in Table 1 of Madau & Dickinson (2014). The solid curve in each panel is the best-fit SFR density with eq. 1.13.
Credit: Fig. 9 in Madau & Dickinson (2014).

relation of SFR and IR luminosity is expressed as:

$$\mathrm{SFR}_{\mathrm{IR}} = \kappa_{\mathrm{IR}} \times L_{\mathrm{IR}}, \tag{1.12}$$

where κ_{IR} is the conversion factor from IR luminosity to SFR. The currently highest redshift of SFR obtained from IR survey is $z = 6$ (Rowan-Robinson et al., 2016). Rowan-Robinson et al. (2016) also concluded that the estimates of star formation from UV survey may seriously underestimated the contribution of dust extinction.

Fig. 1.3 shows the cosmic SFR history both from UV and IR surveys (Madau & Dickinson, 2014), with the best-fitting function:

$$\psi(z) = 0.015 \frac{(1+z)^{2.7}}{1+[(1+z)/2.9]^{5.6}} \mathrm{M}_{\odot}\,\mathrm{year}^{-1}\,\mathrm{Mpc}^{-3}, \tag{1.13}$$

where the SFR density from UV surveys has been dust corrected. Fig. 1.3 clearly displays two phases for the cosmic SFR evolution, both from UV and IR surveys, i.e. a rising phase evolving as $\psi(z) \propto (1+z)^{-2.9}$ at $3 < z < 8$, and a declining phase $\psi(z) \propto (1+z)^{2.7}$ at $z < 1.5$ (Madau & Dickinson, 2014). The rising phase of SFR is related to the structure growth in the early Universe, while the declining one is the result of active galactic nuclei (AGN) and supernovae feedback.

The SFR at different cosmological epochs is also measured from observations of transient events, e.g. core-collapse supernovae (CCSNe) (Dahlen et al., 2004) and gamma ray bursts (GRBs) (Le Floc'h et al., 2006; Wang & Dai, 2009; Wei et al., 2014), as these events originate from the death of massive short-lived stars and thus have a rate directly related to the cosmic SFR. Especially, the GRBs are observed both at low-z and very high-z, that makes GRB as an excellent probe of SFR history in the Universe. However, the SFR derived from GRBs depends on the modeling of the relation between SFR and GRB rate (Wang & Dai, 2009; Kistler et al., 2009; Wei et al., 2014), which is still not clear in this moment.

1.4 First stars

While the first stars are responsible for the first light after the dark age era, and the earliest metal pollution that triggers the formation of PopII/I stars, they are still very mysterious objects, without any direct observations until now. With the help of numerical simulations, abundant studies about the first stars have been done in the literature. They are believed to have formed at redshift $z \sim 20 - 30$ (Bromm, 2013), probably in minihalos with total mass $\sim 10^6\,\mathrm{M}_\odot$ via molecular hydrogen cooling. In this section, I will review recent studies about the stellar mass of the first stars from small scale simulations, and their final fate from simulations of stellar evolution.

1.4.1 Stellar mass

PopIII stars were predicted to be very massive in the first theoretical models to appear in the literature (Abel et al., 2002; McKee & Tan, 2008), with a top-heavy initial mass function (IMF) (Larson, 1998). Recently, some high resolution simulations found that the disks around the first young stars are gravitational unstable due to a rapid accretion (Clark et al., 2011; Stacy & Bromm, 2014), suggesting that the unstable disks would fragment and form multiple low mass PopIII stars. Besides, several physical effects might also affect the predicted mass for first stars. Firstly, the feedback from the early first stars can have an important effect on the formation of the following primordial stars. Considering the influence of far-ultraviolet (FUV) radiation (the Lyman-Werner bands), Hirano et al. (2015) found that two kinds of PopIII stars existed, i.e. the very early PopIII stars (PopIII.1) that might be only a few $\times 10\,\mathrm{M}_\odot$ due to the efficient radiative cooling of molecular hydrogen, and the later PopIII.2_D stars with typical mass $> 100\,\mathrm{M}_\odot$ since the strong FUV field from earlier formed stars would destroy the molecular hydrogen and decrease the cooling efficiency. Secondly, Smith et al. (2012) found that the dark matter annihilation with the weakly interacting massive particle (WIMP) model could heat the gas and suppress disc fragmentation in the first protostars. On the other hand, Stacy et al. (2014) claimed that the interaction between the dark matter and the rotating gaseous disc would flatten the central peak of dark matter density gradually and weaken the dark matter annihilation effect on suppressing gas collapsing and fragmentation. Finally, the primordial magnetic

fields would also have an effect on the formation of first stars, although its extent is still highly debated (Widrow et al., 2012; Bromm, 2013).

Despite the large uncertanties in the prodiction of the mass of the first stars, some attempts are made to study the PopIII IMF. From a statistical sample of 100 first stars obtained by a large set of radiation hydrodynamic simulations, Hirano et al. (2014) found that the first stars have a very wide mass distribution, i.e. from $10 - 1000\,\mathrm{M}_\odot$. Fig. 1.4 (i.e. Fig. 3 in Hirano et al. 2014) presents five primordial star forming clouds in a 15 kpc ($1\,\mathrm{pc} \approx 3.0857 \times 10^{18}\,\mathrm{cm}$) cube at $z \sim 20$, two with mass $< 100\,\mathrm{M}_\odot$, one with mass $= 125\,\mathrm{M}_\odot$ and two with mass $> 300\,\mathrm{M}_\odot$. Hirano et al. (2015) confirmed this result again with their updated simulations having 1540 cosmological halos, but show that the PopIII IMF might have two peaks, one is around stellar mass $\sim 25\,\mathrm{M}_\odot$ and the other one is at $300\,\mathrm{M}_\odot$.

1.4.2 Final fate

The age of a star can be estimated simply from the empirical mass-luminosity relationship $L_\star = L_\odot(m_\star/\mathrm{M}_\odot)^{3.5}$, where $L_\star$ and $m_\star$ indicate the stellar luminosity and mass respectively, and $L_\odot$ is the solar luminosity. The stellar lifetime $\tau \propto m_\star/L_\star \approx 10^{10} \times (m_\star/\mathrm{M}_\odot)^{-2.5}\,\mathrm{yr}$, assuming that all the stellar mass undergoes nuclear fusion. The lifetime of a star is thus very sensitive to its mass. The very massive first stars would die quickly after their birth, e.g. the stellar lifetime of a $100\,\mathrm{M}_\odot$ star is $< 10^6\,\mathrm{yr}$, while the low mass ones, e.g. $0.8\,\mathrm{M}_\odot$ stars with $\tau \sim 1.75 \times 10^{10}\,\mathrm{yr}$, should still survive even now.

The final fate of the massive first stars also depends on their stellar mass (Woosley & Weaver, 1995; Heger & Woosley, 2002). The very massive first stars with stellar mass $> 260\,\mathrm{M}_\odot$ would collapse into black holes directly without too much ejection, while the ones with mass $\sim [140 - 260]\,\mathrm{M}_\odot$ would explode as pair instability supernovae (PISN) without any remnant and contribute abundant heavy elements (Heger & Woosley, 2010). The massive first stars with mass $\sim [25-140]\,\mathrm{M}_\odot$ would end with black holes. If the angular momentum of the formed black hole is very low, a faint supernovae is produced, while the one with high angular momentum would generate a hypernovae (Nomoto et al., 2013).

1.5 Metal Enrichment

Because of their short lifetimes, the massive and very massive first stars ending with supernova explosions would quickly pollute their surrounding gas medium and increase the cosmic metallicity (Maio et al., 2010; Chen et al., 2015). Indeed, PISN could easily enrich a large volume of gas above the metallicity $10^{-4}\,\mathrm{Z}_\odot$ (Campisi et al., 2011), where $\mathrm{Z}_\odot \approx 0.02$ is the solar metallicity. The less massive first stars have smaller metal yields, but their metal pollution would be strongly increased and present effects similar to those of PISN if they were binaries (Chen et al., 2015). The metal pollution of first stars increases the cooling efficiency of the surrounding gas, and PopII stars are formed soon. Because of their very long lifetimes, the low mass PopII stars formed in this medium would still exist

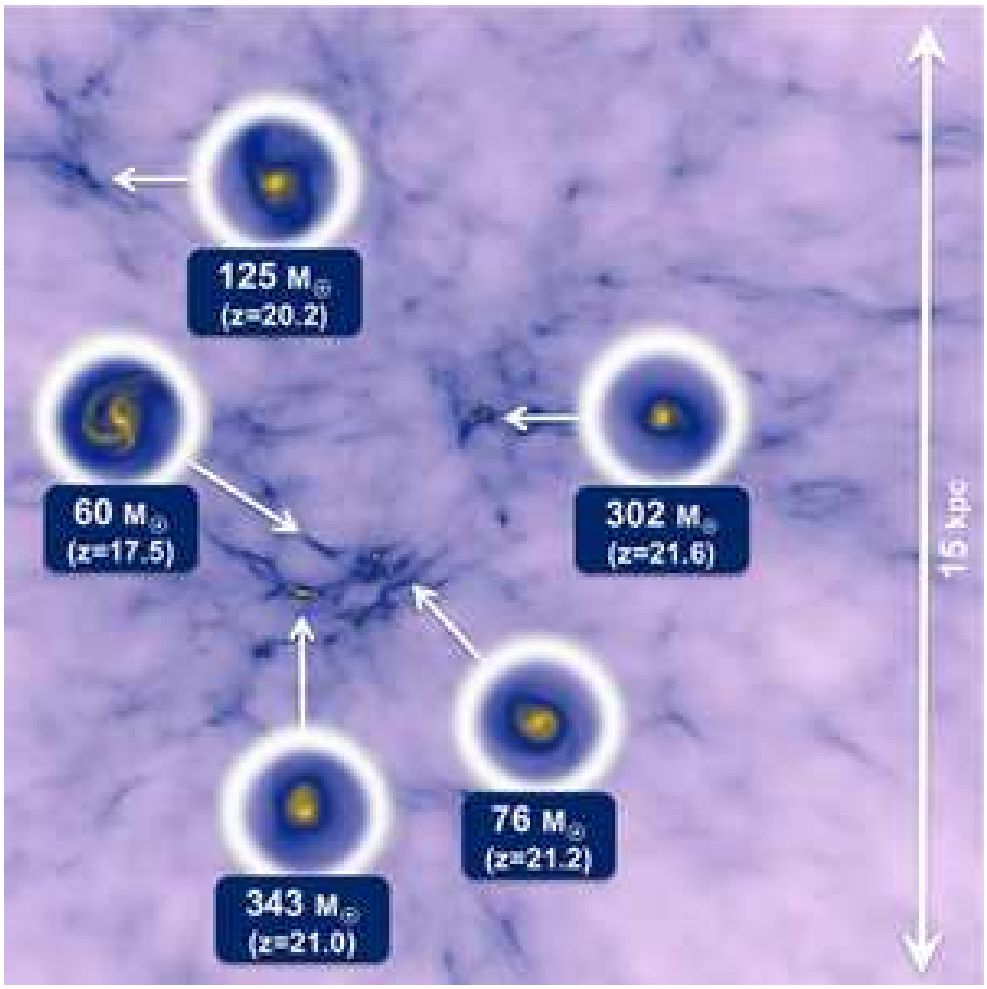

Figure 1.4: Five primordial star forming clouds in a cube of 15 kpc, with gas density background projected at $z = 25$. Each circle is the zoom-in to the central 1 pc region of the cloud, with the corresponding mass and the formation epoch showed.
Credit: Fig. 3 in Hirano et al. (2014).

in the local Universe. By observing the spectra of these stars, one could obtain the metal imprint left by primordial stars and try to set constraints on first star models. A same observational method could also be applied to high-z GRBs and DLAs, which have a high probability to retain the first star metal yields (see more details in Sec. 1.6). However, the final pattern of metallicities and relative abundance ratios from these observing approaches depends on the specific components of metal yields from supernovae, the metal releasing rate of stars and the metal spreading processes, which will be reviewed in this section. In the numerical simulations, all these features should be properly modelled both for PopIII and PopII stars.

1.5.1 Metal yields

The theoretical metal yields of stars are very sensitive to their stellar mass and metallicity. In addition, some other physical properties can also affect the final metal yields (Heger & Woosley, 2010; Nomoto et al., 2013), e.g. the magnetic field, rotation, explosion mechanism and so on.

Population III stars

If PopIII stars are very massive e.g. $> 140\,\mathrm{M}_\odot$, those with mass $< 260\,\mathrm{M}_\odot$ (Heger & Woosley, 2002) or $< 300\,\mathrm{M}_\odot$ (Nomoto et al., 2013) would eject a large amount of heavy elements when exploding as PISN. Because of the explosive oxygen burning, the yields of PISN are expected to have a high [Si/O] and [S/O] (~ 0.6), while the [C/Fe] is relatively low (~ -0.5), as shown in Fig. 1.5 (solid black line). The stars with mass $[300, 3.5\times10^5]\,\mathrm{M}_\odot$ would also suffer the pair-instability burning but they are too massive to be PISN (Nomoto et al., 2013). If such stars end with rapidly rotating black holes (Ohkubo et al., 2006), the formed jet could eject metal materials into the surrounding medium with lower [O/Fe] but higher [Si/Fe] and [C/Si] than the normal PISN. Ohkubo et al. (2006) showed that the metal features of such stars are consistent with the observations of metal ratios of intracluster medium and M82. However, no obvious PISN signals have been found up to now (Nomoto et al., 2013).

The metal yields of massive PopIII stars (with mass $[20, 140]\,\mathrm{M}_\odot$) depend on the rotation of the formed black holes. If the black holes are with little angular momentum, the supernovae would be very faint and have little mass ejection. Since the explosions with lower energy would have more fallback and thus less heavy elements but more α elements to come out, the metal yields from these faint supernovae present very high [C/Fe] (see the dashed black line in Fig. 1.5), that could explain the abundance patterns of carbon-enriched metal-poor (CEMP) stars (Nomoto et al., 2013). Instead, the formed jet of rotating black holes would eject abundant metals and energy, that could be observed as hypernovae. The highly energetic supernovae would prevent the fallback of all ejected materials, thus the hypernovae produce higher [Zn/Fe] and [Co/Fe] but smaller [Mn/Fe], that might explain the metal ratios of observed very metal poor stars (Umeda & Nomoto, 2005). However, this simple spherical explosion model is challenged by the observed [α/Fe] and [(Co,Zn)/Fe]

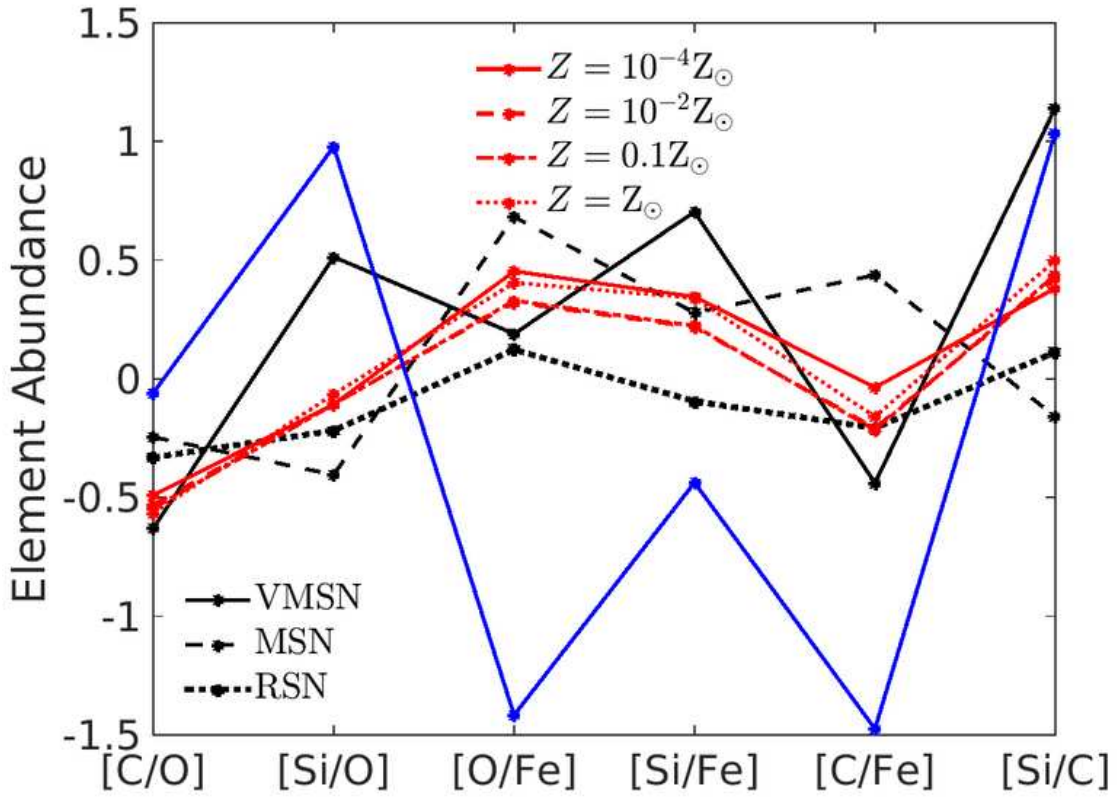

Figure 1.5: IMF integrated abundance ratios of metal yields from PopIII supernovae (black lines), Type II supernovae from PopII stars (red) and Type Ia supernovae (blue). The VMSN, MSN and RSN (see the definitions in Chapter 3) denote PISN, faint supernovae and normal supernovae respectively. The different line styles of red lines indicate the metals from PopII stars with different metallicity: $Z = 10^{-4}\,Z_\odot$ (solid red line), $Z = 10^{-2}\,Z_\odot$ (dashed red), $Z = 0.1\,Z_\odot$ (dot-dashed red), $Z = Z_\odot$ (dotted red).

of extremely metal poor stars (Nomoto et al., 2013), so the fallback should also happen in high energy explosions.

The small mass first stars would end with normal supernovae and produce metals similarly to normal PopII supernovae (Nomoto et al., 2006; Heger & Woosley, 2010), see the dotted black line showed in Fig. 1.5. In this case, metal abundance observations would not be able to identify the first star signatures.

Population II/I stars

The metal contribution from PopII/I stars comes mostly from core collapse supernovae (i.e. Type II supernovae) and Type Ia supernovae (SNIa). The asymptotic giant branch (AGB) stars also contribute some light metal elements, e.g. carbon, oxygen and nitrogen. Because

of the longer lifetimes of their progenitors, SNIa and AGB only have non-negligible metal contribution at low redshift, thus some authors just ignore them in the studies of high-z universe (e.g. Wise et al., 2012; Kulkarni et al., 2013).

The common model of Type II supernovae used for the chemical evolution in cosmological simulations is from Woosley & Weaver (1995), that gave a yields table as a function of stellar mass and metallicity, shown as red lines in Fig. 1.5. However, the iron yields from Woosley & Weaver (1995) are much higher (by a factor ~ 2) than the observations, e.g. SN 1987A. This issue is solved self-consistently in recent versions of nucleosynthesis yields for core-collapse supernovae by considering the mixing and fallback (see the yields table in Nomoto et al., 2013).

Currently, it is still not clear how SNIa formed, and both a single- and double-degenerate model (i.e. the white dwarf accretion model and the two white dwarves merger model) are supported by some indirect evidences (Dilday et al., 2012; Schaefer & Pagnotta, 2012). However, in any case, SNIa should originate from binaries of low mass stars. In cosmological simulations (e.g. Schaye et al., 2015; Tornatore et al., 2007a), the commonly used metal yields of SNIa are from the white dwarf accretion model (Thielemann et al., 2003), see the blue line in Fig. 1.5, that has very high [Si/C,O] but very low [C,O/Fe].

1.5.2 Metal releasing rate

For one single star, the metals are mostly released at the time of supernova explosion, while for a star cluster the releasing of metals is expected to be smoother, so that the releasing rate is the most appropriate quantity to describe metal enrichment from stars. In cosmological simulations, where stars are generated with the same birth time and metallicity in a star particle, the releasing rate for element i at time t is computed as (Tornatore et al., 2007a):

$$\dot{\rho}_i(t) = N p_i(m_\star, Z)\phi(m_\star)\frac{\mathrm{d}m_\star}{\mathrm{d}\tau}\Big|_{\tau=t} \tag{1.14}$$

where N denotes the number of stars produced, $p_i(m_\star, Z)$ is the yields mass of element i from stars with stellar mass $m_\star$ and metallicity Z, $\phi(m_\star)$ denotes the IMF, τ is the stellar lifetime which is a function of $m_\star$ (see Sec. 1.4.2), and t is the time elapsed since the birth of the stars. From eq. 1.14, the metal releasing rate not only relates to the stellar metal yields and the number of formed stars, but also to the IMF and the lifetimes of stars. Usually, massive stars contribute more metal pollution because of their high metal yields and short lifetimes, while, although in larger numbers, low mass stars have a smaller metal contribution. Eq. 1.14 can be used to compute metal yields from e.g. PISN, Type II supernovae, and AGB.

As binary stars evolve differently from single stars, to compute the metal releasing rate from SNIa, one should also consider the fraction of stars that are binaries, and the time delay of the supernovae after the main sequence of stars (Maoz & Mannucci, 2012). For example, in the EAGLE simulations (Schaye et al., 2015), the SNIa rate, that relates to

the stellar mass and an exponential delay time, is expressed as:

$$\dot{N}_{\rm SNIa} = \nu \frac{e^{-t/t_{\rm delay}}}{t_{\rm delay}} \tag{1.15}$$

where $\dot{N}_{\rm SNIa}$ indicates the SNIa rate per unit initial stellar mass, ν is the estimated total number of SNIa per $\rm M_\odot$ which is set to $2 \times 10^{-3}\,\rm M_\odot^{-1}$, and $t_{\rm delay}$ is the empirical delay time (equals 2 Gyr in Schaye et al. (2015)).

1.5.3 Metal spreading

The spreading process of metals is determined by many physical processes in the medium around the star forming regions (Tornatore et al., 2007a), e.g. thermal motions of ions, turbulence, ram-pressure stripping and so on, while in cosmological simulations the diffusion of metals is usually modelled with a simple empirical model without a self-consistent description of these processes (e.g. Tornatore et al., 2007a; Maio et al., 2010; Wise et al., 2012; Xu et al., 2013; Schaye et al., 2015).

For example, in Tornatore et al. (2007a) and Schaye et al. (2015) that use the GADGET code (Springel, 2005), the spreading of metals is done by assigning the metals of a star particle to its neighbour particles with a fraction:

$$w_i = \frac{\frac{m_{\rm g}}{\rho_i} W(r_i)}{\sum_{j=1}^{N_{\rm nb}} \frac{m_{\rm g}}{\rho_j} W(r_j)}, \tag{1.16}$$

where $i(j)$ denotes the $i(j)$th neighbour particle, $W(r_{i(j)})$ is the SPH kernel for the $i(j)$th particle at position $r_{i(j)}$, and $N_{\rm nb}$ is the number of neighbours which is usually chosen as 48 or 64.

In Wise & Abel (2008) and Wise et al. (2012) that use the ENZO code, the metals and also the energy are injected into a sphere with radius $r_{\rm SN}$ from the stars' position when the stars die, by a function:

$$f(r) = A\big\{0.5 - 0.5\tanh[B(\frac{r}{r_{\rm SN}} - 1)]\big\} \tag{1.17}$$

where A is a normalization factor, B controls the transition rate to the ambient medium, and $r_{\rm SN}$ describes the maximal distance that can be reached by metals, which equals 1 pc in Wise & Abel (2008) and 10 pc in Wise et al. (2012).

Besides, the galactic winds, which are triggered by the supernova energy release (Springel & Hernquist, 2003), would also help to spread the metals outside star forming regions. Tornatore et al. (2007a) found that the increasing of winds efficiently distribute the metals in the gas, that turns into a more diffused enrichment pattern than the case without winds.

1.6 Observational Approaches to Detect First Stars

Some PopIII explosions might be very energetic and bright, so that the next generation space telescopes, e.g. James Webb Space Telescope (JWST), could be able to detect them

and give a direct observational constraint on the properties of the first stars (Whalen et al., 2013a; Hummel et al., 2012; Whalen et al., 2013b). On the other hand, PopIII stars themselves might be very difficult to detect (Rydberg et al., 2013). In this section, I will review popular approaches that have been proposed to study the first stars: metal poor stars in our Milky Way (Nomoto et al., 2013; Frebel & Norris, 2015), high-z Gama Ray Bursts (GRB), and also Damped Lyman-alpha Absorbers (DLA; Kulkarni et al., 2013; Maio & Tescari, 2015). In addition, in the last subsection, I will give a review of other proposed approaches present in the literature.

1.6.1 Metal poor stars

The low-mass PopII stars formed in the medium polluted by PopIII stars would retain a metal imprint from the first stars, and appear as metal poor (MP) stars ([Fe/H] < -2) in the Galactic halo and in the nearby dwarf spheroidal satellites (dSphs). Observing these MP stars gives a first glimpse onto the first stars (e.g. Beers & Christlieb, 2005; Tolstoy et al., 2009).

Based on their [Fe/H] content, MP stars are classified into (see recent review, Nomoto et al., 2013): very metal poor (VMP) stars with [Fe/H] $\sim [-3, -2]$, extremely metal poor (EMP) stars with [Fe/H] $\sim [-4, -3]$, ultra metal poor (UMP) stars with [Fe/H] $\sim [-5, -4]$, hyper metal poor (HMP) stars with [Fe/H] $\sim [-6, -5]$ and mega metal poor (MMP) stars with [Fe/H] < -6 (Beers & Christlieb, 2005). The VMP stars are probably enriched by many supernovae because of their high metallicity, and their abundance pattern is also similar to that of well-mixed ejecta of many supernovae (Nomoto et al., 2013). The metal components of EMP stars are likely from one single or a small number of PopIII supernova explosions (Tumlinson, 2006). Only few samples are available for UMP and HMP stars and only one for MMP stars (Frebel & Norris, 2015). It is not clear if they are survived small mass PopIII stars, or PopII stars formed by gas enriched by a single PopIII supernova (Umeda & Nomoto, 2003). In any case, the UMP, HMP and MMP stars should be the most convincing candidates to study first stars.

The observed MP stars (with the exception of VMP stars) are presented in Fig. 1.6 (Fig. 8 in Frebel & Norris, 2015), that shows the distribution of [C/Fe], [N/Fe] and [O/Fe] of MP stars as a function of [Fe/H] ([C/Fe]). These stars (red points) present very significant CEMP feature, i.e. their [C/Fe] increases dramatically with decreasing [Fe/H] from the top left panel. As the α-elements nitrogen and oxygen share a similar nuclear synthesis mechanism with carbon, they show very similar distributions with [C/Fe] on these panels, i.e. [N/Fe] and [O/Fe] increase as [Fe/H] decreases. Besides, the [C/Fe] of MP stars displays a linear relation with [O/Fe] and [N/Fe], but no relation with [C/N]. Some MP stars (black points) also show a normal abundance for carbon, but they are typically with [Fe/H] > -4.5.

The typical CEMP feature of MP stars is usually explained by the yields of faint, black hole forming supernovae originated from the massive first stars (Iwamoto et al., 2005), while the carbon-normal MP stars might be explained by the pollution from hypernovae (Umeda & Nomoto, 2005). However, although a lot of MP stars are observed, no one

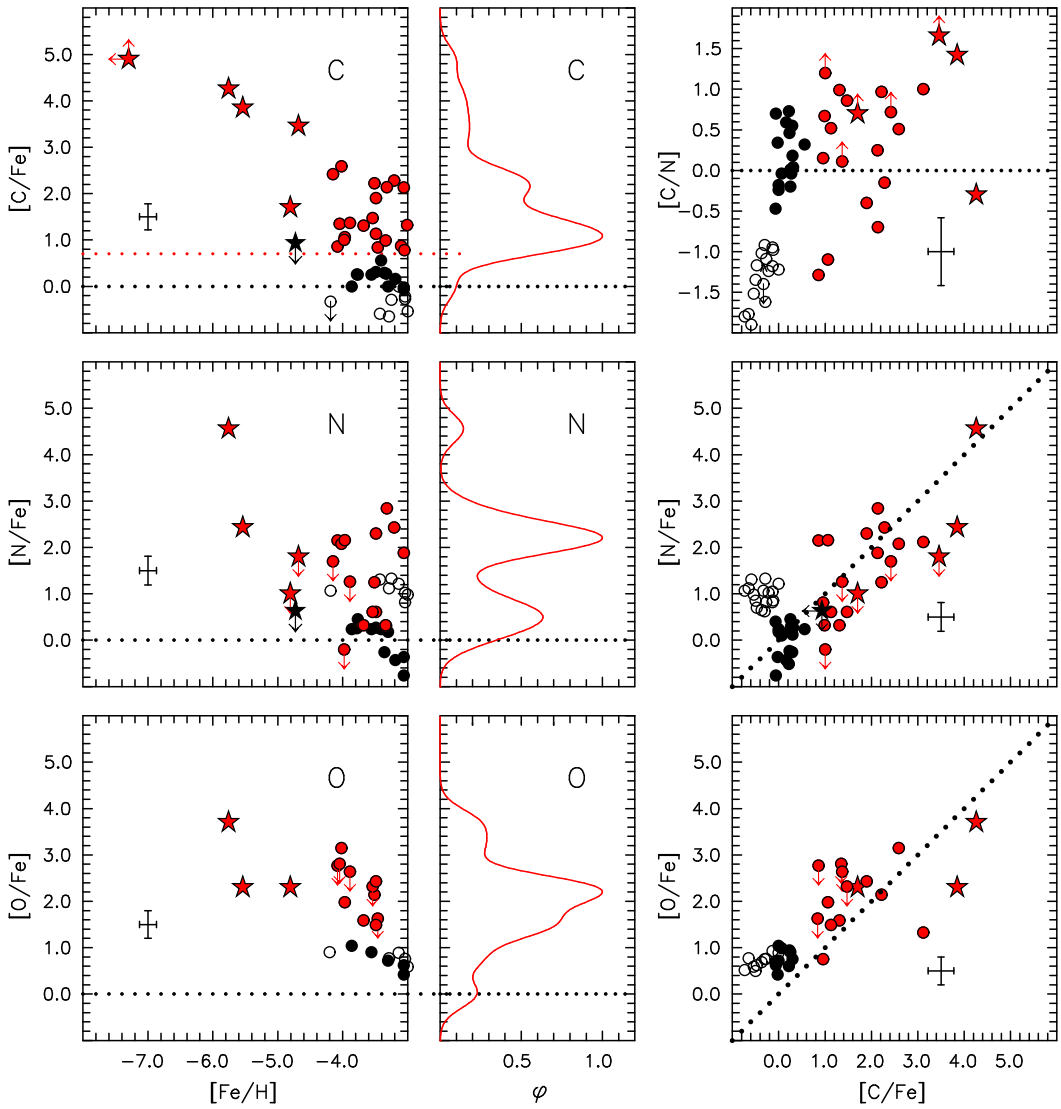

Figure 1.6: From top to bottom, [C/Fe] ([C/N] in the right column), [N/Fe], and [O/Fe] of observed metal poor stars as a function of [Fe/H] (left) and [C/Fe] (right). The middle column shows the generalized histograms to the abundances in the left, with a Gaussian kernel ($\sigma = 0.3$). Red and black symbols denote the C-rich and C-normal stars respectively. The circles (star symbols) indicates the [Fe/H] of objects above (below) -4.5.
Credit: Fig. 8 in Frebel & Norris (2015).

presents obvious features of PISN or of small mass first stars, that means the first stars can only be massive ($20 - 140\,M_\odot$), or the CEMP feature is caused by other physical effects, e.g. the mass transfer from an AGB star with a binary companion (Suda et al., 2004; Suda & Fujimoto, 2010), the mass loss from a rotating star (Meynet et al., 2006), or even the self-enrichment of those MP stars (Campbell et al., 2010).

1.6.2 Gamma ray bursts

After the death of massive stars, the accretion of material onto formed black holes would generate a powerful magnetic field, that ejects part of falling material with a relativistic velocity. The relativistic electrons inside would energize pre-existing low-energy photons into gamma-rays by inverse-Compton scattering (Woźniak et al., 2009), and generate powerful flashes of gamma ray radiation with a long duration (larger than two seconds). This is one of the most common long-GRBs forming models, although it is still challenging to match all the observations. When the relativistic jet goes on and hits the ambient medium, it forms a shock wave. The acceleration of energetic electrons within the shock wave by strong local magnetic fields radiates as synchrotron emission that ranges from X-ray to radio radiation (Mészáros & Rees, 1997). This is the so called GRB afterglow. Fig. 1.7 shows a diagram to explain where and how the GRB and the GRB afterglow form.

Because of their high luminosity, GRBs have been detected at very high redshift, such as GRB 080913 at $z = 6.7$ (Greiner et al., 2009), GRB 090423 at $z = 8.2$ (Salvaterra et al., 2009) and GRB 090429B at $z = 9.4$ (Cucchiara et al., 2011). As they are expected to be observable at even higher redshift, GRBs could be the most promising way to probe the first stars (Ciardi & Loeb, 2000; Campisi et al., 2011). The signatures of first stars might be found in two kinds of high-z GRBs, i.e. the GRBs forming directly from primordial stars (GRBIII) (Suwa & Ioka, 2011; Wang et al., 2012; Toma et al., 2016), and PopII GRBs (GRBII) hosted in a medium enriched by first stars. For the GRBs happened after the death of very massive PopIII stars, Suwa & Ioka (2011) showed that the relativistic GRB jets could break out even if their hydrogen envelope is supergiant, because of their long-lived powerful accretion. Such GRBs would be characterized by a very long duration, $\sim 1000(1 + z)$ s, and an isotropic luminosity in excess of $\sim 10^{54}\,\mathrm{erg\,s^{-1}}$. Their afterglow spectra could be easily detected with Swift Burst Alert Telescope (BAT)/XRT and Fermi Large Area Telescope (LAT) (Toma et al., 2011).

Nevertheless, not so many such works are done for the low-mass and massive first stars. In this case, the triggered GRBs are probably not so luminous. PopII GRBs that might retain the first star signatures are studied in this thesis (see Chapter 2, and 3).

Although a lot of theoretical studies showed that there is a high probability to find first stars signatures in high-z GRBs, until now no GRBs has been proved to relate to PopIII stars. In fact, although several high-z GRBs have high precise metal ratio measurements, no first star metal pollution signature has been found.

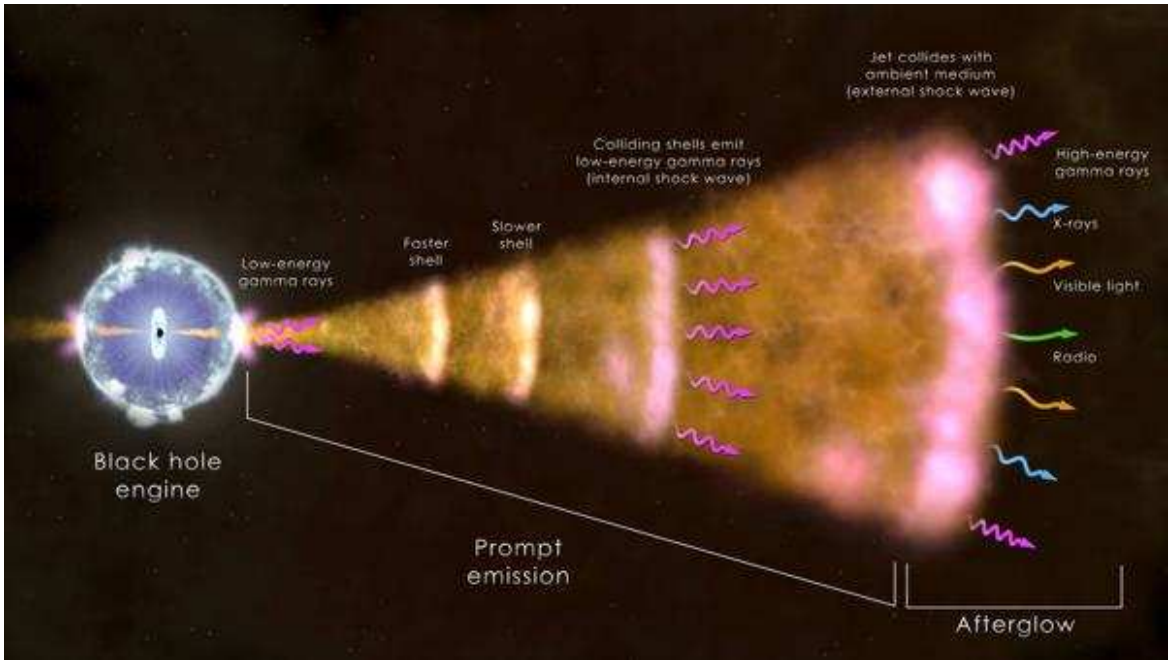

Figure 1.7: A diagram to explain how gamma-ray burst and afterglow formed. Left is the central black hole formed after the collapse of a massive star. It would launch a jet moving nearly at the speed of light. When the jet collides with the ambient medium the GRB and the afterglow are formed (right).
Credit: NASA's Goddard Space Flight Center.

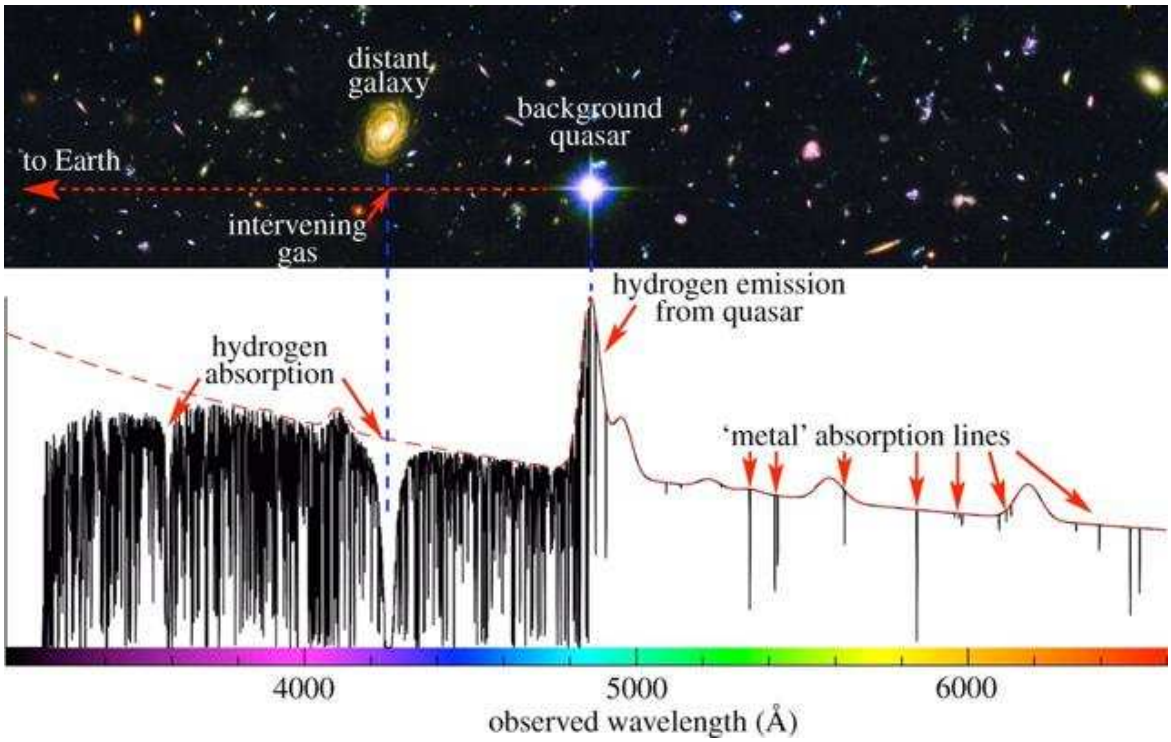

Figure 1.8: An illustration to describe how DLAs formed and what their typical features are. When the light of a QSO (in the middle of the top panel) goes through the Universe to the observer, the gas within galaxies located along the path would imprint on the QSO spectrum e.g. hydrogen absorption troughs and metal absorption lines (bottom panel). *Credit:* Fig. 3 in Pettini (2011).

1.6.3 Damped lyman-alpha absorbers

When the light of powerful sources, e.g. quasars (QSO) or GRBs (Wolfe et al., 2005; Ledoux et al., 2009), goes though a gas cloud, the neutral hydrogen encountered imprints a Lyα absorption on its spectrum. At the same time, each metal element would also have its specific absorption. Fig. 1.8 presents an illustration of how this works and of the typical features left by the various absorbers on the QSO spectrum, e.g. the hydrogen absorption troughs and the metal absorption lines (Pettini, 2011). By analyzing these features, one could obtain the chemical abundances, metallicity, SFR and kinematics of the gas cloud. DLAs are defined as those clouds with HI column densities $N_{\rm HI} \geq 2\times10^{20}\,{\rm cm}^{-2}$. While $2\times10^{20}\,{\rm cm}^{-2}$ is just a historical threshold set by the HI properties of nearby spiral galaxies, it is also the column density that could distinguish neutral from ionized gas at high redshift, i.e. the gas is likely ionized (neutral) if $N_{\rm HI} < (>) 2\times10^{20}\,{\rm cm}^{-2}$ (Wolfe et al., 2005). QSO surveys have found DLA samples both at low and very high redshift, e.g. the highest redshift of a DLA is $z\sim7$ (Simcoe et al., 2012), and several samples at $z\sim6$ are published with high precision relative abundance ratio observations (Becker et al., 2012). These DLA systems present a chemical evolution with redshift (Rafelski et al., 2012), i.e.

the metallicities of DLAs reduce quickly with increasing redshift.

Considering that the cool and neutral gas, especially in the low-mass galaxies, might not suffer too much star formation and thus might retain signatures of metal pollution from primordial stars, DLAs have been proposed to study the first stars (Pettini, 2011; Kulkarni et al., 2013). An advantage of using DLAs is that, from a theoretical point of view, it is easier to model physical systems of cool and neutral gas than stellar atmospheres of MP stars (Pettini, 2011).

With an excellent analytic modelling for the coupled evolution of galaxies and the intergalactic medium, Kulkarni et al. (2013) found that a sample of DLAs at high redshift should confidently constrain the first star enrichment and the PopIII IMF, by measuring the metallicity and relative abundance ratios. These conclusions are also confirmed in this thesis with N-body/hydrodynamic simulations, shown in Chapter 4.

Currently, only a metal poor DLA system at $z \approx 3$ is observed with a CEMP feature (Cooke et al., 2012), and no observed DLA at $z > 5$ shows clear signatures of metal pollution from the first stars (Becker et al., 2012). One potential challenge is that the currently observed DLAs have metallicities $> 10^{-3}\,\mathrm{Z}_\odot$ (Rafelski et al., 2012), and Pettini (2011) suggested that DLAs with lower metallicity might be beyond the limit of current observations, while DLAs with significant PopIII star signatures should have a metallicity lower than $10^{-3.5}\,\mathrm{Z}_\odot$.

1.6.4 Other approaches

In addition to those already discussed above, some other methods are also proposed to study PopIII stars.

If the first stars are super massive, they could form direct collapse black holes (DCBHs). The accretion of DCBHs in metal-free halos would have very strong radiation emission but still too faint to be detected individually in current surveys. Their cumulative effect, though, could be detected as contribution to the near-infrared background and could be used to provide a hint for the first star model (Yue et al., 2013).

The Ultra faint dSphs, which are mostly dark matter dominated, are the oldest systems in the Milky Way, with typical mass $10^{78}\,\mathrm{M}_\odot$ and [Fe/H] < -2 (Kirby et al., 2008; Salvadori & Ferrara, 2009). Salvadori & Ferrara (2009) concluded that they were probably formed at $z > 8.5$ and might still keep the information about the first stars. Thus observations of these old systems would help to understand the early Universe, especially the formation of first stars.

When the metals were blown out from the galaxies where first stars formed, they could remain in the intracluster medium (ICM). Since the ICM is more hardly affected by the star formation in the galaxies than the interstellar medium (ISM), the observation of metal ratios in the ICM might be another opinion to study first stars. Actually, through a stacked analysis of all the galaxy clusters observed by the X-ray telescope ASCA, Baumgartner et al. (2005) found that the metal abundances in the ICM are hardly explained by the normal Type II and SNIa supernovae, but consistent with the metal yields of very massive, metal-poor stars.

Some authors also claim that signatures of the first stars could leave an imprint in the 21cm signal from neutral hydrogen at high redshift, which could be detected by e.g. SKA and used to derive constraints on their properties (Chen & Miralda-Escudé, 2008; Yajima & Khochfar, 2015).

1.7 Outline of This Thesis

Although a lot of effort has been done, understanding the properties of the first stars remain an open issue issue in modern astronomy. As the signatures of first stars should be prominent at high redshift than in our local Universe, in thesis I studied the possibility of using high-z GRBs and DLAs to indirectly probe the first stars. Specifically, this thesis is organised as follows.

In Chapter 2, I study the high-z GRBs hosted in a medium enriched by first stars using one hydrodynamic simulation with a very massive first star model, and present the results on e.g. the fraction of such GRBs, their predicted observable rate, and also the properties of GRB host galaxies.

Chapter 3 deals with a similar topic but including three simulations with different mass ranges for the PopIII stars. I show the effects of first star models on the GRB rates and the host galaxies. Besides, I also discuss how to distinguish the first star models from observations.

In Chapter 4, I present the results of high-z DLAs which may retain signatures from the first stars, with three mass ranges considered for the PopIII stars. I study the fraction of DLAs that have metal pollution dominated by first stars and the evolution with redshift, and also the properties of these DLAs. I also compare my simulated results with the observations at $z \sim 6$ and give my conclusions.

I summarize the major results and conclusions in Chapter 5, together with the discussion and outlook for further works on the detection of first stars.

Throughout this thesis, a standard ΛCDM cosmological model is adopted with the following parameters: cosmological constant density parameter $\Omega_{0,\Lambda} = 0.7$, total matter density parameter $\Omega_{0,M} = 0.3$, baryon matter density $\Omega_b = 0.04$, primordial spectral index $n = 1$, cosmic variance within a sphere of 8 Mpc/h radius $\sigma_8 = 0.9$ and Hubble expansion parameter $h = 0.7$ in units of 100 $\mathrm{km\,s^{-1}\,Mpc^{-1}}$.

Chapter 2

PopIII signatures in the spectra of PopII/I GRBs

In this chapter, I use numerical simulations to investigate signatures of very massive PopIII stars in the metal-enriched environment of GRBs originating from PopII/I stars. This chapter is organized as follows: in Section 2.1 I describe the employed simulations; in Section 2.2 I discuss the results in term of rate of GRBs, metal signatures and properties of the host galaxies; in Section 2.3 I give the discussions and the major conclusions of this chapter.

2.1 Simulations and metal abundances

The simulation code used here is a modified version of the GADGET2 code (Springel, 2005) based on previous works (see e.g. Maio et al., 2007; Tornatore et al., 2007a; Maio et al., 2010, 2013a, for further details). The same simulations are also used in Campisi et al. (2011) and Salvaterra et al. (2013) to study the properties of high-z GRBs and their host galaxies. In the following, I will refer to the previous papers as C2011 and S2013, respectively. Here I describe the essential features of the simulations, while I refer the reader to the original paper for more details. The box side length is $10\,\mathrm{Mpc}\,h^{-1}$ with particles number 2×320^3, yielding a gas and dark matter particle mass of $3.39 \times 10^5\,\mathrm{M}_\odot\,h^{-1}$ and $2.20 \times 10^6\,\mathrm{M}_\odot\,h^{-1}$, respectively. In the N-body hydrodynamical chemistry calculations, the transition from a primordial (PopIII) to a PopII/I star formation regime is determined by the metallicity, Z, of the star forming gas. More specifically, a Salpeter initial mass function (IMF; $\phi(m_\star) \propto m_\star^{-2.35}$ is the number fraction of stars per unit stellar mass) with mass range $[100 - 500]$ $\mathrm{M}_\odot$ is adopted if $Z < Z_{crit} = 10^{-4} Z_\odot$, while a Salpeter IMF with mass range $[0.1 - 100]$ $\mathrm{M}_\odot$ is used at larger metallicities.

Besides gravity and hydrodynamics, the code follows early chemistry evolution, cooling, star formation and metal spreading from all the phases of stellar evolution according to the suited metal-dependent stellar yields (for He, C, N, O, S, Si, Mg, Fe, etc.) and mass-dependent stellar lifetimes for both the pristine PopIII regime and the metal-

X	$\log_{10}(N_X/N_H)_\odot$	X	$\log_{10}(N_X/N_H)_\odot$
C	-3.57	Si	-4.49
N	-4.17	S	-4.86
O	-3.31	Ca	-5.66
Mg	-4.4	Fe	-4.53

Table 2.1: Solar element abundance adopted for calculating the chemical element abundance (Asplund et al. 2009).

enriched PopII/I regime (Tornatore et al., 2007a; Maio et al., 2007, 2010). Yields for massive pair-instability supernovae (PISN) in the stellar mass range $[140 - 260]\,M_\odot$ are taken by Heger & Woosley (2002). Standard type-II supernova (SNII) yields for progenitors with different metallicities and masses of $[8 - 40]\,M_\odot$ are from Woosley & Weaver (1995), AGB metal production for lower-mass stars is followed according to van den Hoek & Groenewegen (1997) and type-Ia SN (SNIa) yields are from Thielemann et al. (2003). Several models for stellar nucleosynthesis are available in the literature and can give different yields; however, the overall metallicity is usually affected in a minor way (as already discussed in e.g. Maio et al., 2010).

In general, to better characterize the metal content of gas, stars or galaxies, it is convenient to define abundance ratios between two arbitrary species A and B as follows:

$$[\mathrm{A/B}] = \log_{10}\left(\frac{N_\mathrm{A}}{N_\mathrm{B}}\right) - \log_{10}\left(\frac{N_\mathrm{A}}{N_\mathrm{B}}\right)_\odot , \tag{2.1}$$

where N_A and N_B are the number densities of the two species and the subscript $_\odot$ refers to the corresponding solar content (Table 2.1; Asplund et al. 2009). Abundance ratios are powerful tools to investigate the pollution history and to probe stellar evolution models against observational data.

2.2 Results

In this Section I will show results on the rate of GRBs originated from PopII/I stars exploding in a gas enriched by PopIII stars, together with a discussion on the properties of the galaxies hosting such GRBs and observational strategies to identify them. This is an interesting issue, because high-redshift PopII/I GRBs exploding in a medium pre-enriched by former star formation episodes can reveal features of primordial PopIII generations through the metallicity patterns of their hosting galaxy.

2.2.1 Rate of GRBs

I calculate the rate of GRBs as described in C2011. Here I provide only the essential information, while I refer the reader to the original paper for more details. The comoving

GRB formation rate density, ρ_{GRBi}, can be calculated as:

$$\rho_{GRBi} = f_{GRBi}\zeta_{BH,i}\rho_{*,i}, \tag{2.2}$$

where i indicates the subsample of GRBs considered, f_{GRBi} is the fraction of BHs that can produce a GRB, $\zeta_{BH,i}$ is the fraction of BHs formed per unit stellar mass and $\rho_{*,i}$ is the comoving star formation rate density. I select star forming particles associated to PopII/I stars based on the criterium that $Z > Z_{crit}$, i.e. without an upper metallicity cut, as the GRB1 in C2011. For the sake of clarity though, here I change the nomenclature and refer to GRBII (GRBIII) as those GRBs originating from PopII/I (PopIII) stars. These are called GRB1 (GRB3) in C2011. Following the original paper, I adopt $\zeta_{BH,II} = 0.002$ and $f_{GRBII} = 0.028$ for GRBII (which correspond to a minimum stellar mass of stars dying as BHs of 20 $M_\odot$), and $\zeta_{BH,III} = 0.0032$ for GRBIII. $f_{GRBIII_{up2}} = 0.0116$ is obtained assuming that no GRBIII is present among the 266 GRBs with measured redshift, while the more stringent value $f_{GRBIII_{up1}} = 0.0039$ is found imposing that none of the 773 GRBs observed by `Swift` is a GRBIII. I additionally study a third class of GRBs, namely the GRBII that explode in a medium enriched by PopIII stars, which I indicate as GRBII→III. Here, $\zeta_{BH,II\to III} = \zeta_{BH,II}$, $f_{GRBII\to III} = f_{GRBII}$, and $\rho_{*,II\to III}$ is explicitly calculated by selecting only those star forming particles which have been enriched by PopIII stars. This task is accomplished by using indicative metal ratios (see also next) for PopIII enrichment, consistently with the mentioned yield tables. In particular, PopIII PISN enrichment results characterized by: [Fe/O] < 0, [Si/O] > 0, [S/O] > 0 and [C/O] < -0.5. These limits are used as reference selection criteria for PopII/I star forming regions enriched by PopIII stars (see Sec. 2.2.2 for further discussion).

Figure 2.1 shows the redshift evolution of the quantity $r_{GRBi} = \rho_{GRBi}/(\rho_{GRBtot})$, where ρ_{GRBtot} is the total GRB rate. As expected, both r_{GRBIII} and $r_{GRBII\to III}$ decrease with decreasing redshift, as the number of PopIII stars and their impact on the gas metal enrichment become less relevant. As a consequence, while $r_{GRBII\to III}$ is as high as $\sim 50\%$ at $z \sim 16$, it becomes less than 1% at $z < 5$. On the other hand, r_{GRBIII} is always negligible, consistently with previous studies, as the transition from PopIII to PopII/I stars is very rapid.

The (physical) observable rate of GRBi (in units of $\mathrm{yr}^{-1}\mathrm{sr}^{-1}$) at redshift larger than z can be written as (e.g. C2011):

$$\begin{aligned} R_{GRBi}(>z) &= \gamma_b \int_z dz' \frac{dV(z')}{dz'} \frac{1}{4\pi} \frac{\rho_{GRBi}(z')}{(1+z')} \\ &\times \int_{L_{th}(z')} dL' \psi_i(L'), \end{aligned} \tag{2.3}$$

where $\gamma_b = 5.5 \times 10^{-3}$ is the beaming fraction for an average jet opening angle of $\sim 6^\circ$ (Ghirlanda et al., 2007, 2013), $dV(z)/dz$ is the comoving volume element and ψ_i is the normalized GRB luminosity function. The factor $(1+z)^{-1}$ accounts for the cosmological time dilation. The last integral gives the fraction of GRBs with isotropic equivalent peak luminosities above L_{th}, corresponding to an observed photon flux of ~ 0.4 ph s^{-1} cm^{-2} in

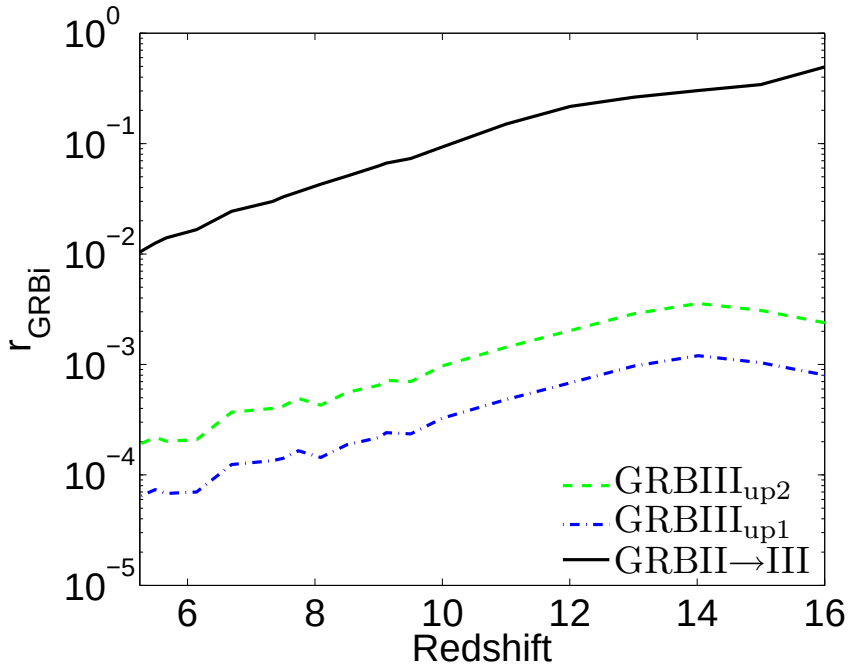

Figure 2.1: Redshift evolution of the ratio between the rate of GRBi and the total GRB rate. i=II→III (black solid) and III (blue dotted-dashed for GRBIII$_{up1}$ and green dashed for GRBIII$_{up2}$).

the 15-150 keV band of the `Swift/BAT`. I refer the reader to C2011 for a more exhaustive discussion on the choice of L_{th} and ψ_i (see also Salvaterra et al., 2012).

Interestingly, while there are much less GRBIII than GRBII→III (Fig. 2.1), the former can be more easily detected because of their larger luminosity, as can be seen from Figure 2.2, resulting in very similar observable rates. Nevertheless, I should note that R_{GRBIII} has to be considered as an upper limit to the expected number of detections, as I have assumed here (as in C2011) that all GRBIII can be detected by `Swift/BAT` thanks to their expected extreme brightness. This should be true for GRBs originating from very massive PopIII stars, while in case of more standard masses luminosities should be similar to those from regular PopII stars[1].

2.2.2 Metal signatures

I now discuss the metal signatures which could help in identifying a GRBII→III. Since the contribution to the metal enrichment from different stellar types is explicitly included in the simulations, the final abundance of each heavy element can be computed from the metal masses as traced at each output time.

[1] GRBIII rates from C2011 have been updated by taking into account the new GRBs detected by `Swift` after the publication of C2011. These lead to a decrease of the C2011's PopIII GRB rate by a factor of 773/500 = 1.546 for the 'up1' case and by a factor of 266/140 = 1.9 for the 'up2' case.

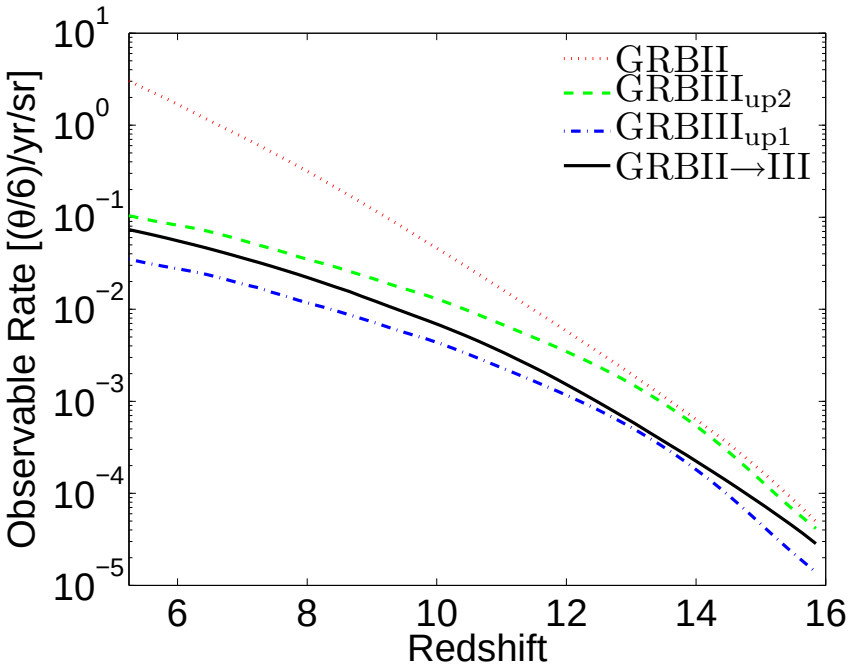

Figure 2.2: Rate of GRBi with redshift larger than z observable by `Swift/BAT` (see text for details). i=II (red dotted line), II→III (black solid) and III (blue dotted-dashed for GRBIII$_{up1}$ and green dashed for GRBIII$_{up2}$).

I use abundances normalized to oxygen, because this species is not very sensitive to theoretical yield uncertainties and is widely adopted in the literature. Additional reference species will be discussed in the following, though. For a given species X, I calculate the abundance ratio [X/O] in eq. 2.1 with $N_{\rm X}/N_{\rm O} = (A_{\rm O} m_{\rm X}) / (A_{\rm X} m_{\rm O})$, where $A_{\rm X}$ is the atomic mass number of element X and $m_{\rm X}$ is the mass of X in a particle as given by the simulation. Moreover, it is possible to write $\log_{10}(N_{\rm X}/N_{\rm O})_{\odot} = \left[\log_{10}(N_{\rm X}/N_{\rm H})_{\odot} - \log_{10}(N_{\rm O}/N_{\rm H})_{\odot}\right]$. Since GRBs are usually found in actively star forming environments, only gas particles with non-zero SFR are considered while performing the calculations of the various chemical abundances.

Before discussing the element abundances obtained from the simulations, it is instructive to look at Figure 2.3, which shows the metal abundance of some elements from different stellar types of a simple stellar population, as expected by averaging over the corresponding IMF. More specifically, [X/O] in eq. 2.1 is obtained using

$$[{\rm X/O}] = \frac{N_{\rm X}}{N_{\rm O}} = \frac{A_{\rm O} \int M_{\rm X}(m_\star)\phi(m_\star)dm_\star}{A_{\rm X} \int M_{\rm O}(m_\star)\phi(m_\star)dm_\star} \tag{2.4}$$

where $M_{\rm X}$ is the stellar mass yield of element X for a given stellar population and the integration is performed over the relevant mass range for each stellar type. In the Figure, I do not show AGB stars, as their contribution to the metal enrichment is negligible for all shown elements, with the exception of C and O, which are produced in different amounts

according to progenitor masses and metallicities, although typically [C/O]$\gtrsim 0$.

It is evident that each stellar phase is characterized by specific yields, that can be used to exclude or identify their contribution to metal enrichment. In particular, a positive and large value of [Fe/O] would indicate a strong contribution from SNIa, while a negative value could be due both to SNII and to PopIII stars (PISN). On the other hand, while SNII contribute with negative [Si/O] and [S/O], PopIII stars and SNIa contribute with positive ratios of the same elements. As mentioned above, AGB stars are the only ones to contribute with a usually positive [C/O] ratio. It is then clear that we can easily exclude gas enriched by SNIa as the one with [Fe/O]>0. Similarly, [S/O]<0 and [Si/O]<0 indicates gas enriched by SNII, and [C/O]>0 by AGB stars. It should be noted that the gas metallicity, Z, can affect the outflow of SNII and of AGB stars[2], but the considerations above still apply. So, to ensure that gas enriched by a stellar type other than PopIII stars is excluded, criteria such as [Fe/O]<0, [S/O]>0, [Si/O]>0 and [C/O]<0, could be adopted, although, as mentioned previously, the more stringent condition [C/O]<-0.5 has been chosen (see Sec. 2.2.1).

Figure 2.4 shows the distribution at various redshifts of some relevant elements in star forming particles with $Z > Z_{crit}$. With the exception of the highest redshift, when there are only a handful of star forming particles, two peaks can be clearly identified in each curve. The broader peak increases with decreasing redshift, and its metallicity abundance is similar to the one from SNII, so that metal enrichment of the particles in this peak might be led by gas expelled during SNII explosions. The increase of the peak with z is due to the time and metallicity evolution of the involved stellar systems. Indeed the relative shift in carbon abundance [C/O] is due to the metallicity-dependent carbon yields of massive stars augmented by the delayed release of carbon from low- and intermediate-mass stars (e.g. Akerman et al., 2004; Cescutti et al., 2009; Cooke et al., 2011). Thus, the low values observed at $z \sim 17 - 13$ are caused by SNII exploding in increasingly enriched gas (i.e. producing increasingly lower [C/O], as depicted in Fig. 2.3) and a subsequent rise at $z \sim 13 - 5$ led by AGB stars. The similar trend observed in [Fe/O] is a result of cosmic metal evolution as well, and at $z \sim 5 - 6$ the ratio is sustained also by the very first SNIa starting to explode after ~ 1 Gyr lifetime. Conversely, there is little variation in the distribution of the α ratios ([Si/O], [S/O], [Mg/O]), as the nuclear reactions leading to their formation path are directly linked to O production. The element abundance of the narrow peaks seems more consistent with the yields from PopIII stars. Below $z \sim 9$ the peak stops increasing as a result of the extremely small PopIII SFR.

Because some metallicity limits are equivalent in excluding particles enriched by a specific stellar type (e.g. [Si/O], [S/O] and [Mg/O] can be equally used to exclude particles with metallicity dominated by SNII, while [C/O] or [Fe/O] can be used for SNIa), GRBII→III can be identified also using less stringent criteria, and typically only two conditions are enough, such as [C/O] plus [Si/O], [C/O] plus [Mg/O], [Mg/O] plus [Fe/O]

[2]SNIa yields are weakly dependent on metallicities because they all derive from a white dwarf growing towards the Chandrasekhar mass and burning (in electron-degenerate gas) C and O in equal proportions (Thielemann et al., 2004).

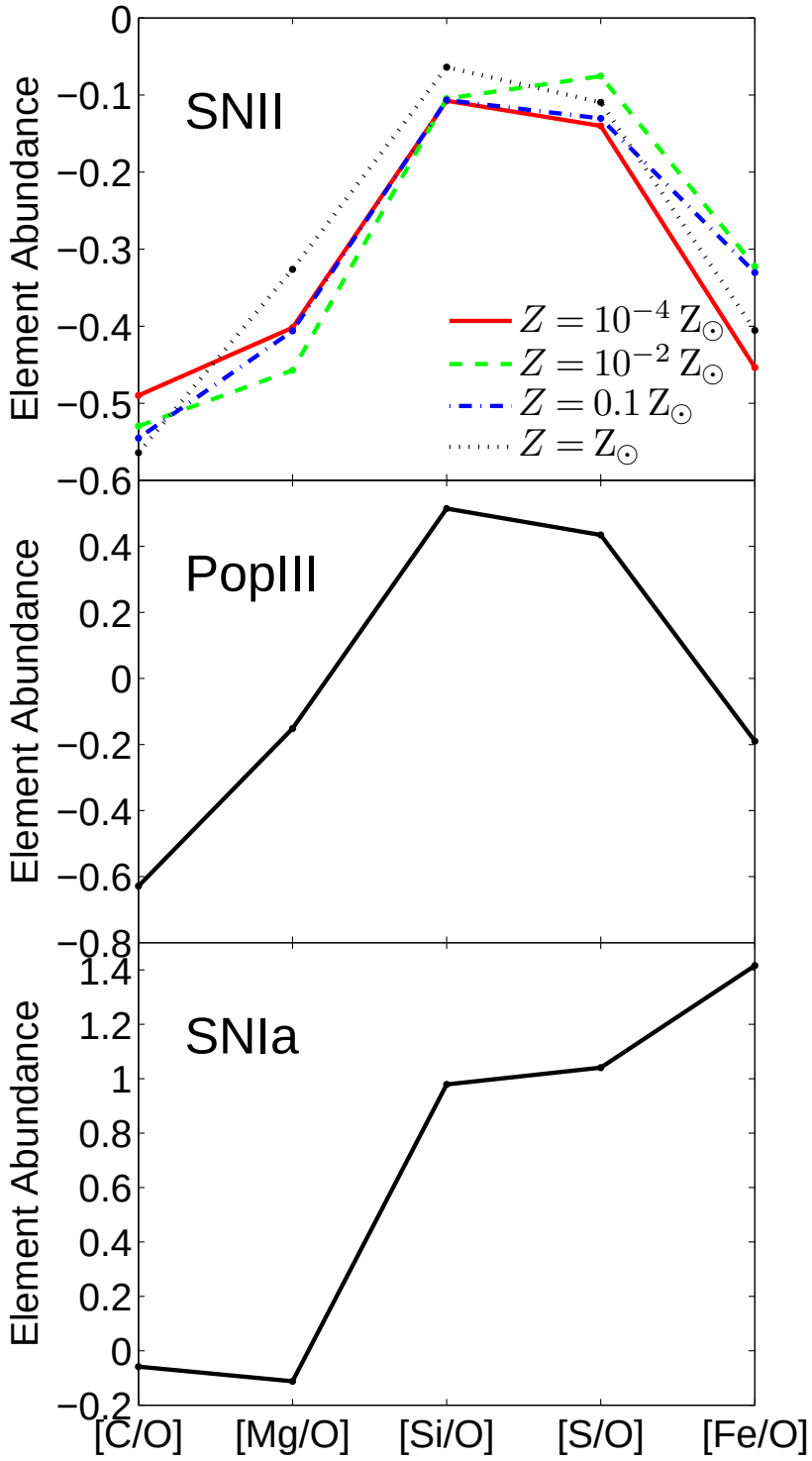

Figure 2.3: Element abundance as produced by: SNII (upper panel), PISN (middle) and SNIa (lower). The contribution from SNII depends on the gas metallicity, Z, as indicated in the legend.

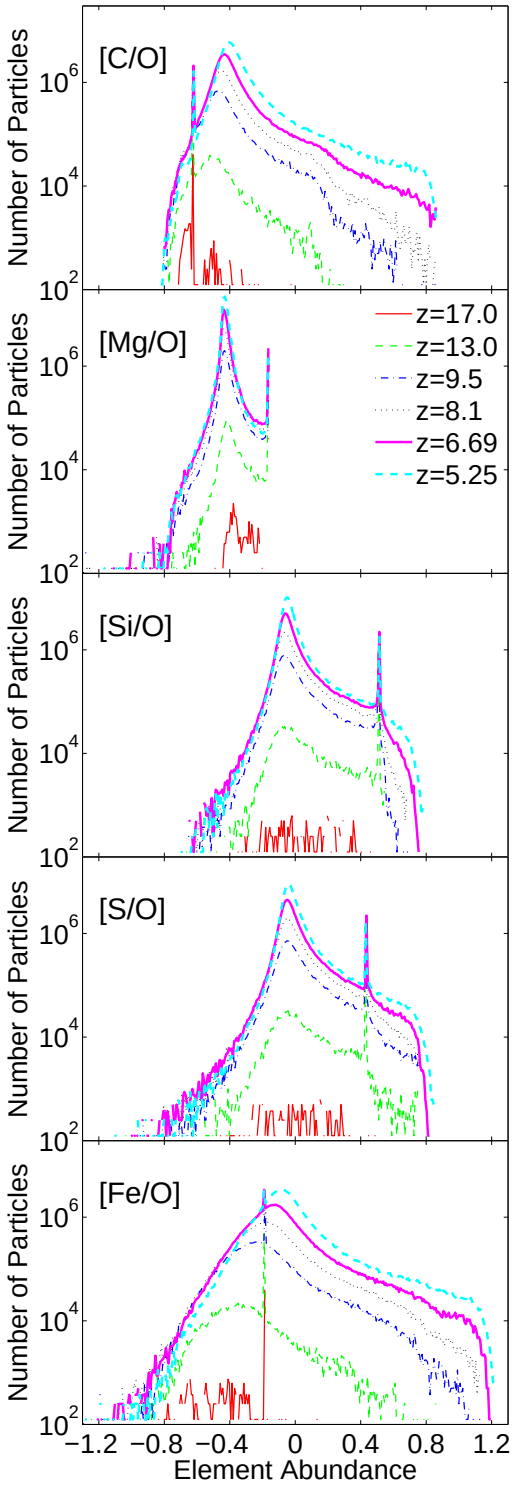

Figure 2.4: Abundance distribution (in number of particles) of, from top to bottom, C, Mg, Si, S and Fe of star forming particles with $Z > Z_{crit}$. The distributions are shown at $z = 17$ (solid red lines), 13 (green), 9.5 (blue), 8.1 (black), 6.69 (magenta) and 5.25 (cyan).

or [Si/O] plus [Fe/O]. I find that if adopt [C/O]<-0.5 and [Si/O]>0, or [C/O]<-0.5 and [Mg/O]>-0.4 the ratio $r_{GRBII\rightarrow III}$ is $\sim$ 1% (4%) and $\sim$ 20% (50%) larger then the one shown in Figure 2.1 at $z = 17$ (5). At $z > 12$ the following criteria give similar results: [C/O]<-0.5 and [Mg/O]>-0.4, [Fe/O]<-0.1 and [Si/O]>0, [Fe/O]<-0.1 and [Mg/O]>-0.4. Finally, [S/O] and [Si/O] have similar selection effects, i.e. the same particles are selected if use either [S/O]>0 or [Si/O]>0.

2.2.3 Host galaxies

In this Section I discuss some properties of galaxies hosting a GRBII→III. Both observations and theoretical studies suggest that high-redshift ($z > 5$) long GRBs occur in objects with a SFR lower than the one of the local Universe ($z \sim 0$). Salvaterra et al. (2013), for example, find that such host galaxies have typically a stellar mass $M_\star \sim 10^6 - 10^8$ M$_\odot$ and a SFR $\sim 0.003 - 0.3$ M$_\odot$ yr^{-1}. In general, metal enrichment from primordial star forming regions is efficient in polluting the structures hosting GRB episodes and in bringing typical metallicities above the critical value for stellar population transition. This is in agreement with recent theoretical studies of primordial galaxies (Maio et al., 2011; Biffi & Maio, 2013; Wise et al., 2012, 2014) and of GRB hosts (Campisi et al., 2011; Salvaterra et al., 2013), that suggest a typical metallicity range between $\sim 10^{-4}$ Z$_\odot$ and $\sim 10^{-1}$ Z$_\odot$ at $z > 6$. However, it is not clear yet how these statistical trends change when considering the sample of GRBII episodes in regions polluted by previous PopIII events. In order to discuss this issue, I compute the metallicity distributions at different redshift for both the whole galaxy population and for the GRBII→III hosting population.

In Figure 2.5 I show the metallicity distribution of halos hosting a GRBII→III (solid black line) and of all PopII/I star forming halos (dotted red line) at different redshift. While at the highest redshift both distributions are very similar in terms of halo number fractions (left panels), differences are visible at later times, when the typical metallicity of GRBII hosts increases. The simplest interpretation of these trends relies on the fact that primordial GRBII events take place in environments that have been previously enriched by the first PopIII generation and hence the two distributions almost coincide at early epochs, when only PopIII stars had time to explode and pollute the gas. At later stages, PopIII stars play an increasingly minor role in the global star (and GRB) formation rate, which is dominated by PopII/I stars. This means that successive GRBII events will happen in gas that has been enriched by several generations of PopII/I stars, as already visible in the high-Z tail of the distributions at $z = 8.1$. Consequently, GRBII→III can survive only in the low-Z tail, where there is still some probability of having residual PopIII pollution in galaxies with weak star formation. This can be more clearly seen from the panels in the right columns, where I show a SFR "weighted" metallicity distribution, i.e. the fraction SFR$_{i,j}$/SFR$_{i,tot}$, where SFR$_{i,j}$ is the SFR of halos in the j-th metallicity bin calculated for the component i =II, II→III, and SFR$_{i,tot}$ is the SFR of all halos for the same component. This explains the distributions at $z = 5.25$ and, more quantitatively, suggests a metallicity of roughly $Z < 10^{-2.8}$ Z$_\odot$ to highlight the presence of a GRBII→III (or possibly a GRBIII) in the early Universe. Another distinctive feature is the presence of two peaks at $Z \sim 10^{-4}$ Z$_\odot$

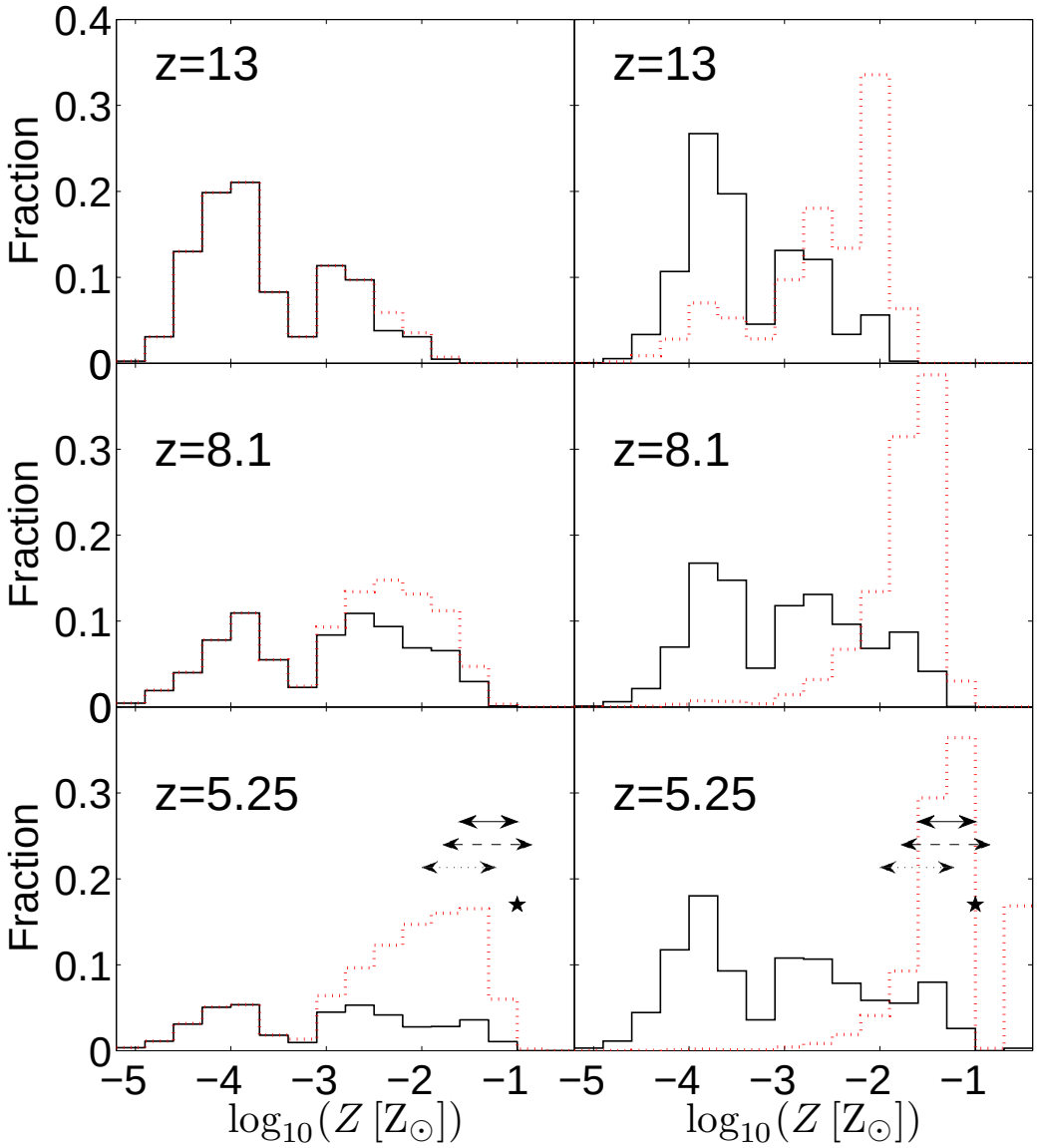

Figure 2.5: Metallicity distribution of halos hosting a GRBII→III (solid black line) and of all PopII/I star forming halos (dotted red) at redshift $z = 13$ (top), 8.1 (middle) and 5.25 (bottom). *Left panels:* halos number fraction distribution normalized to the total number of star forming halos. *Right panels:* the distributions are "weighted" by their respective SFRs and normalized to the total SFR (see text for more details). The double arrows denote the Z range of GRB 050904 (solid black), GRB 130606A (dashed black) and GRB 111008A (dotted black). The black solid star denotes the Z of GRB 100219A.

and $10^{-2.8}$ $Z_\odot$, found also in C2011 for GRBIII host galaxies (see their Fig. 3). This may be an indication that GRBII→IIIs reside in galaxies similar to those hosting GRBIII, albeit with a higher star formation activity, as better highlighted by weighting the distribution of the host metallicities by the SFR (right panels). Finally, I should note that a comparison with the metallicity range of the host galaxy of GRB 130606A (Castro-Tirado et al., 2013; Chornock et al., 2013) seems to indicate that this is not a GRBII→III. Although the redshift of GRB 130606A is 5.91, i.e. slightly higher than what shown in the Figure, this does not change my conclusion because of the small redshift evolution of the peak at $Z \sim 10^{-2} - 10^{-1}$ $Z_\odot$. A similar conclusion can be drawn for GRB 050904 at $z = 6.3$ (Kawai et al., 2006), GRB 111008A at $z = 5.0$ (Sparre et al., 2014) and GRB 100219A at $z = 4.7$ (Thöne et al., 2013).

The corresponding SFR distributions, shown in Figure 2.6, span the range $\sim 10^{-4.5} - 10\,M_\odot\ yr^{-1}$ and neatly support the interpretation, giving an upper limit of $\sim 10^{-2}\,M_\odot\ yr^{-1}$ for GRBII→III host galaxies (higher values of the SFR are found, but with a much lower probability). More specifically, the SFR displays a trend similar to the one of the metallicity, with GRBII→III forming preferentially in halos with a SFR smaller than the one of GRBII hosts, and a large fraction of halos with SFR $\sim 10^{-4} - 10^{-3}$ $M_\odot\ yr^{-1}$ hosting a GRBII→III at all redshifts. The highest probability of detecting a GRBII→III, though, is in halos with a slightly higher SFR, i.e. $\sim 10^{-2.5}$ $M_\odot\ yr^{-1}$, as shown in the right column (note that here the distributions are calculated as in Fig. 2.5, where Z bins are substituted by SFR bins).

Finally, in Figure 2.7 I show the stellar mass distribution of halos hosting a GRBII→III (solid black line) and of all PopII/I star forming halos (dotted red) at different redshift. Despite both distributions being very similar in terms of halo number fraction at the highest redshift (left panels) as z decreases GRBII→III are still preferentially hosted by halos with $M_\star \sim 10^5$ $M_\odot$, while the typical host of a GRB has a stellar mass about one or two orders of magnitude larger. The right panels of the Figure, showing the distributions of the host stellar masses "weighted" by their respective halo SFR (note that here the distributions are calculated as in Fig. 2.5 where Z bins are substituted by $M_\star$ bins), confirm that the highest probability of detecting a GRBII→III is, as above, in structures with $M_\star \sim 10^5$ $M_\odot$ at all redshifts.

2.3 Discussions and Conclusions

The results presented in this chapter are based on numerical calculations including detailed chemistry evolution, gas cooling according to suited metal-dependent stellar yields (for He, C, N, O, S, Si, Mg, Fe, etc.) and mass-dependent stellar lifetimes for both the pristine PopIII regime and the metal-enriched PopII/I regime (Tornatore et al., 2007a; Maio et al., 2007, 2010). Metal pollution proceeds from dense star forming regions to surrounding lower-density environments and is responsible for the enrichment of the Universe already in the first billion years, when early massive stars die and possibly generate GRB events. Numerical limitations (see a more complete discussion in e.g. Maio et al., 2010, and ref-

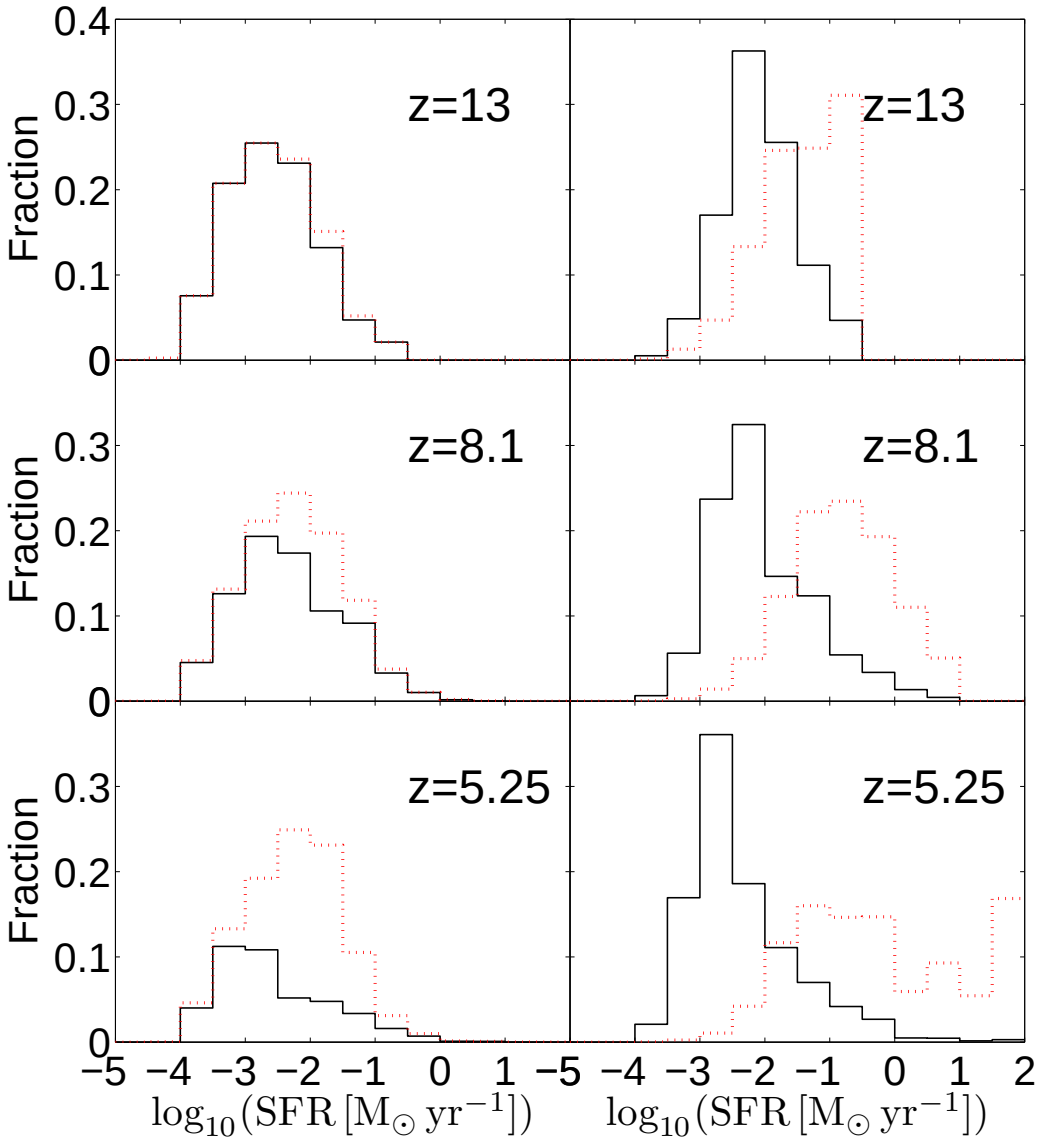

Figure 2.6: SFR distribution of halos hosting a GRBII→III (solid black line) and of all PopII/I star forming halos (dotted red) at redshift $z = 13$ (top), 8.1 (middle) and 5.25 (bottom). *Left panels:* halos number fraction distribution normalized to the total number of star forming halos. *Right panels:* the distributions are "weighted" by their respective SFRs and normalized to the total SFR (see text for more detail).

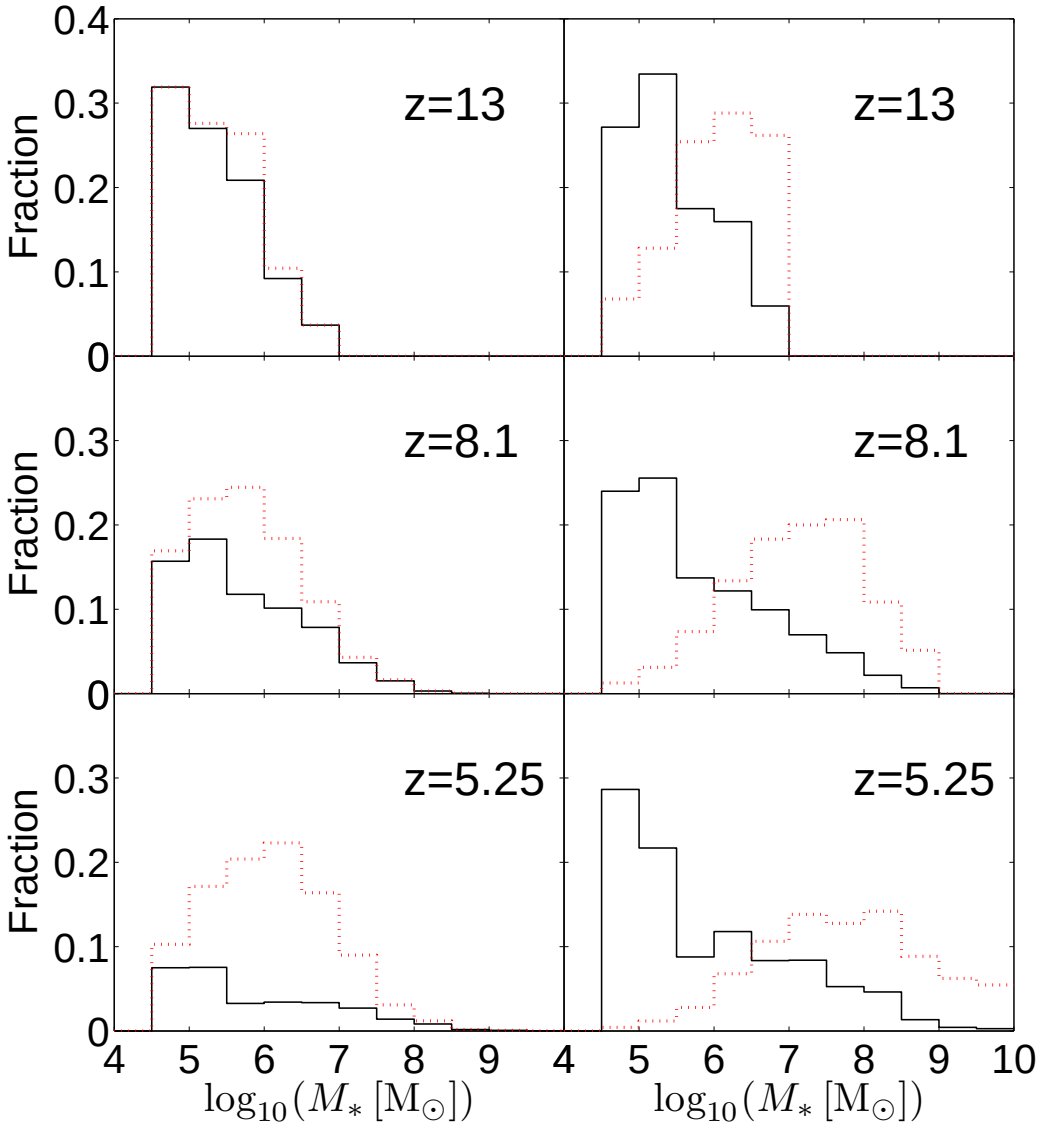

Figure 2.7: Stellar mass distribution of halos hosting a GRBII→III (solid black line) and of all PopII/I star forming halos (dotted red line) at redshift $z = 13$ (top), 8.1 (middle) and 5.25 (bottom). *Left panels:* halos number fraction distribution normalized to the total number of star forming halos. *Right panels:* the distributions are "weighted" by their respective SFRs and normalized to the total SFR (see text for more details).

erences therein) in addressing such issues might lie in the uncertainties of metal-diffusion modeling (both in SPH and grid-base approaches). Effects due to the PopII/I IMF slope and features or to the particular critical metallicity adopted in the range $\sim 10^{-6} - 10^{-3}\,Z_{\odot}$ are minor.

On the other hand, a PopIII IMF shifted towards lower masses as recently suggested by some authors (Yoshida et al., 2007; Suda & Fujimoto, 2010; Clark et al., 2011; Stacy & Bromm, 2014) is expected to have a larger impact on my results. In this case, in fact, the metal yields from PopIII stars are expected to be more similar to those from PopII/I stars and thus it would be increasingly difficult (if at all possible) to discriminate gas enriched by primordial stars based on metal abundances. I explicitly checked this issue by re-running the same box with a PopIII IMF in the $0.1 - 100 M_{\odot}$ mass range and I found results consistent with analogous studies based on DLA observations and employing low-mass pristine IMFs (e.g. Kulkarni et al., 2014). More specifically, I found that while assuming a SN mass range of 8-40$M_{\odot}$ it would be extremely difficult to distinguish GRBII→III because the metal yields of PopIII stars are too similar to those of PopII/I stars, including stars as massive as 100$M_{\odot}$ would induce extremely high Oxygen and Carbon yields (Heger & Woosley, 2010). In the latter case, GRBII→III could be identified e.g. using the condition [Si/O]<-0.6, [S/O]<-0.6 and [C/O]>-0.4.

Possibly different metal yields as predicted by different stellar structure models could slightly shift the resulting abundance ratios according to the specific input yield tables, but no major changes are expected, mostly at low metallicities (Cescutti et al., 2009). Resolution effects are generally unavoidable, but they are likely to play a minor role for the abundance ratios explored here and for the star formation regime transition, since these processes are predominantly determined by stellar evolution timescales, which are constrained relatively well. The cosmology adopted is ΛCDM, but changes in the background cosmological scenario and the introduction of high-order non-linear effects would not affect dramatically the baryonic properties within bound structures (see e.g. Maio et al., 2006, 2011, 2012; Maio & Iannuzzi, 2011; Maio & Khochfar, 2012; de Souza et al., 2013; Maio & Viel, 2015). Despite that, some particular dark-matter models might cause a delay in early structure formation (as is the case for warm dark matter; de Souza et al., 2013; Maio & Viel, 2015).

I have found that the rate of GRBII→III rapidly decreases with cosmic time from $\sim 50\%$ at $z = 16$ down to less than 1% at $z < 5$, and one tenth of the GRBs exploding at $z = 10$ should report the metal signature of the enrichment by a PopIII supernova explosion. By convolving the intrinsic rate of these events with the GRB luminosity function, I found that ~ 0.06 GRBII→III yr^{-1} sr^{-1} should be sufficiently bright to trigger `Swift/BAT`. This means that ~ 0.8 GRBII→III should be present in the entire `Swift` database.

The identification of such events can be obtained by looking at peculiar metal abundance ratios. I showed that [C/O] and [Si/O] alone could be enough to distinguish GRBII→III from other GRB populations. However, in practice, the detection of more elements (such as S and Fe) could help observers in further confirming the nature of the source. While I have presented all my results with respect to abundance ratios normalized to oxygen, because O is not very sensitive to theoretical yield uncertainties, it is possible

to get particularly interesting hints by referring metal abundances to Si, as well. In this case, PopII star forming particles enriched by PopIII stars can be identified as those with [C/Si] < -0.5, [O/Si] < 0 and [Fe/Si] < -0.4, where the first two conditions exclude gas enriched by SNII, while the last one excludes pollution from SNIa. AGB stars produce no Si and thus they are excluded in any case from such analysis. I find that the above conditions give results very similar to those obtained using my reference criteria in the entire redshift range.

It should be noticed that it is hard to get accurate Fe abundances from observations at high redshift, while C, Si and O are usually easier to probe (Castro-Tirado et al., 2013; Kawai et al., 2006). In addition, Fe yields might be overestimated of up to a factor of ~ 2 (Cescutti et al., 2009). Thus, Fe is not the best suited element to identify GRBII→IIIs.

I also explored the properties of galaxies hosting GRBII→III in my simulations. These are very similar to those that have a high probability to host a GBRIII (Salvaterra et al., 2013), i.e. GRBII→III are typically found in galaxies with stellar mass ($\sim 10^{4.5} - 10^{7} \mathrm{M}_{\odot}$), SFR ($\sim 10^{-3} - 0.1 \mathrm{M}_{\odot}\mathrm{yr}^{-1}$) and metallicity ($\sim 10^{-4} - 10^{-2} Z_{\odot}$) lower than those of galaxies hosting a GRBII. It is worth to note that galaxies with $\log_{10}(Z/Z_{\odot}) < -2.8$ most probably host GRBII→III and GRBIII. A GRB with measured metallicity below this Z limit should be considered as a strong candidate for being originated in a PopIII enriched environment (or by a PopIII progenitor).

From an observational point of view, GRBII→III signatures can be directly investigated for the currently known high-z GRBs. At $z \gtrsim 6$ metal absorption lines in the optical-NIR spectrum have been detected and metal abundance ratios measured only for two bursts, namely GRB 050904 at $z = 6.3$ (Kawai et al., 2006) and GRB 130606A at $z = 5.91$ (Castro-Tirado et al., 2013).

The observed abundances for GRB 050904 are [C/H]=-2.4, [O/H]=-2.3, [Si/H]=-2.6 and [S/H]=-1.0 translating into [C/O]=-0.1, [Si/O]=-0.3 and [S/O]=0.7. On this basis, I can exclude GRB 050904 to be a GRBII→III. Recent studies by Thöne et al. (2013) have reported an updated abundance for S of [S/H]$= -1.6 \pm 0.3$ and a corresponding metallicity of $\log(\mathrm{Z/Z}_{\odot}) = -1.6 \pm 0.1$, instead of $\log(\mathrm{Z/Z}_{\odot}) = -1.3 \pm 0.3$ (Kawai et al., 2006) as inferred from Si absorption lines of the afterglow spectrum. However, such variations do not affect my conclusion on GRB 050904.

For GRB 130606A Castro-Tirado et al. (2013) reported a 3σ upper limit of [S/H] < -0.82 and determined the lower limits of the oxygen and silicon abundance as [Si/H] > -1.80 and [O/H] > -2.06, and metallicity Z as $\sim (1/60 - 1/7)\,\mathrm{Z}_{\odot}$. Results from Chornock et al. (2013) give [Si/H] > -1.7 and [S/H] < -0.5, while Hartoog et al. (2015) find [C/H] > -1.29, [O/H] > -1.88, [Si/H] $= -1.33 \pm 0.08$, [S/H] < -0.63 and [Fe/H] $= -2.12 \pm 0.08$. Using these information, it is possible to estimate corresponding limits of [S/O] < 1.24, [Si/O] < 0.55, and [Fe/O] < -0.24. These are too weak, though, to probe the nature of the environment in which the burst explodes. I also note that the lower limits on the total metallicity based on Si and O (Chornock et al., 2013) suggest a moderately enriched environment where GRBII are likely to dominate. However, the possibility that GRB 130606A is associated to a PopIII enriched environment can not be completely excluded, although a comparison with the metallicity expected for a galaxy hosting a GRBII→III seems to

indicate otherwise.

Another possible candidate at $z = 4.7$ could be GRB 100219A, for which Thöne et al. (2013) reported the following measurements: [C/H] $= -2.0 \pm 0.2$, [O/H] $= -0.9 \pm 0.5$, [Si/H] $= -1.4 \pm 0.3$, [S/H] $= -1.1 \pm 0.2$ and [Fe/H] $= -1.9 \pm 0.2$. Metallicity is about $0.1\,Z_\odot$ and is derived from the abundance of sulphur. From such values one can get [C/O] $= -1.1 \pm 0.7$, [Si/O] $= -0.5 \pm 0.8$, [S/O] $= -0.2 \pm 0.7$ and [Fe/O] $= -1 \pm 0.7$. The precision at 1σ-level is not enough to draw robust conclusions, though.

I also note that preliminary analyses are available for GRB 111008A at $z = 5.0$ (Sparre et al., 2014), which is the highest-redshift GRB with precise measurements of metallicity, column densities and iron, nickel, silicon and carbon fine-structure emissions. Reported abundance ratios within 2σ-error bars are: [Si/H] > -1.97, [S/H] $= -1.70 \pm 0.10$, [Cr/H] $= -1.76 \pm 0.11$, [Mn/H] $= -2.01 \pm 0.10$, [Fe/H] $= -1.74 \pm 0.08$, [Ni/H] $= -1.64 \pm 0.19$, [Zn/H] $= -1.58 \pm 0.21$. The authors do not give carbon and oxygen values, but they note that [Fe/H], [Ni/H] and [Si/H] measurements suggest metallicities around $\sim 1-6$ per cent solar, well above the $10^{-2.8} Z_\odot$ limit for GRBIII and GRBII→III. Morevover, the inferred reddening ($A_V = 0.11 \pm 0.04$ mag) of the afterglow indicates that the dust-to-metal ratio of the host galaxy is 0.57 ± 0.26, similar to typical values of the Local Group. Hence, the GRB environment should be strongly dominated by PopII/I enrichment, while it is unlikely that it has been pre-enriched by massive PopIII stars.

Finally, the metallicity inferred from X-ray measures at higher z (Campana et al., 2011; Starling et al., 2013) suggests values above a few percent solar. These might not be reliable though, as the X-ray value of the H column density they are based on is likely affected by intervening metals along the line-of-sight (Campana et al., 2012, 2015). With future X-ray facilities like the *Athena* satellite (Nandra et al., 2013)[3] it will become possible to directly measure the abundance patterns for a variety of ions (e.g. S, Si, Fe) superimposed on bright X-ray afterglows. This, in principle, will allow to discriminate between different nucleo-synthesis sources (Jonker et al., 2013) and identify GRBII→IIIs.

[3] http://www.the-athena-x-ray-observatory.eu/

Chapter 3

Constraining the PopIII IMF with high redshift GRBs

Considering that the metal yields from PopIII supernova explosions depend strongly on the mass of their progenitor star (Heger & Woosley, 2002, 2010), which in the current literature is predicted to be both large (e.g. Schneider et al. 2002; Heger & Woosley 2002; Suda & Fujimoto 2010) and small (e.g. Clark et al. 2011; Stacy & Bromm 2014), in this chapter I run numerical hydrodynamical chemistry simulations with different PopIII initial mass functions (IMFs) and study how gas pollution of GRBII hosts is affected by these changes. This chapter is organised as follows: the simulations used are described in Sec. 3.1, as well as the classification for gas particles; the results are presented in Sec. 3.2; I will critically discuss the caveats of approach adopted and give major conclusions in Sec. 3.3.

3.1 Simulations

I run three simulations with different PopIII IMFs using the same simulation code described in Chapter 2. The runs are referred to as Very Massive SN (VMSN), Massive SN (MSN) and Regular SN (RSN), as listed in Table 3.1. All models adopt IMFs with Salpeter slope, but they differ in the lower/upper mass limits and the range of masses contributing to metal pollution. The VMSN model is the same one described in Chapter 2, i.e. the first stars are assumed to be very massive, in the range [100, 500] $M_{\odot}$, while the stars contributing to metal spreading are the progenitors of PISN in the mass range [140, 260] $M_{\odot}$ (Heger & Woosley, 2002). Both MSN and RSN models have a PopIII IMF covering masses over [0.1, 100] $M_{\odot}$. In the RSN case, PopIII stars with mass [40, 100] $M_{\odot}$ are assumed to collapse directly into BHs, so that the only contribution to metal enrichment comes from the mass range [10, 40] $M_{\odot}$ (Woosley & Weaver, 1995; Heger & Woosley, 2002). In the MSN scenario, instead, stars with masses in the range [40, 100] $M_{\odot}$ also contribute to metal pollution by exploding as core-collapse SNe (Heger & Woosley, 2010).

Besides, metal pollution by PopIII stars is followed separately from that by PopII/I stars. More specifically, for each gas particle in the simulated boxes, the fraction of metals

Model	PopIII range [$M_\odot$]	SN range [$M_\odot$]	PopII range [$M_\odot$]
VMSN	$100 - 500$	$140 - 260$	$0.1 - 100$
MSN	$0.1 - 100$	$10 - 100$	$0.1 - 100$
RSN	$0.1 - 100$	$10 - 40$	$0.1 - 100$

Table 3.1: From left to right the columns refer to: model name, stellar mass range for the PopIII IMF, stellar mass range for SN explosions and stellar mass range for the PopII IMF.

produced by PopIII stars is defined as:

$$f_{\rm III} = \frac{\sum_j m_{Z_j,{\rm III}}}{\sum_j m_{Z_j}}, \tag{3.1}$$

where m_{Z_j} is the mass of metal element Z_j in the gas particle, while $m_{Z_j,{\rm III}}$ is the mass coming from PopIII stars. Here Z_j indicates all heavy elements except from hydrogen and helium. According to the value of $f_{\rm III}$, I assign each gas particle with non-zero Z to one of the following three classes:

- PopII-dominated, if $f_{\rm III} < 20\%$;
- intermediate, if $20\% < f_{\rm III} < 60\%$;
- PopIII-dominated, if $f_{\rm III} > 60\%$.

I have verified that the exact boundaries chosen for the class definition (e.g. $\pm 10\%$) do not have a relevant impact on the results presented in the paper.

As a sanity check, I display in Fig. 3.1 the history of the comoving star formation rate (SFR) density, ρ_*, for both PopIII and PopII/I stars, as derived from the three simulations considered. I also over-plot observational determinations inferred from data in different bands (Zheng et al., 2012; Coe et al., 2013; McLure et al., 2013; Ellis et al., 2013; Oesch et al., 2013, 2014; Duncan et al., 2014; Bouwens et al., 2014, 2015; Rowan-Robinson et al., 2016). While the simulations have very similar PopII/I SFR, the contribution from PopIII stars differs as a consequence of the different PopIII modeling (Maio et al., 2010). The PopII/I SFR density is comparable to the one estimated from observations in the infrared (IR) at $z \approx 6$ (Rowan-Robinson et al., 2016), but higher than most of the data points derived from the UV magnitudes of galaxies at $5 < z < 11$ (e.g. Bouwens et al., 2014, 2015; Duncan et al., 2014). These latter values may give an incomplete picture, though, since UV determinations could underestimate the contribution of embedded star formation (Rowan-Robinson et al., 2016) of up to 1 dex (Kennicutt & Evans, 2012; Madau & Dickinson, 2014). Despite the lower dust content of early galaxies in comparison to $z < 3$ objects expected by e.g. Capak et al. (2015), the critical issues on high-z IR luminosities (Bouwens et al., 2016; Laporte et al., 2016) and the origin of dust grains (Mancini et al., 2015; Ferrara et al., 2016; Bocchio et al., 2016) still persist. Hence, dust extinction might be important already at $z \sim 7$ and could hide the existence of dusty, UV-faint galaxies at early epochs (Salvaterra et al., 2013; Mancini et al., 2016; Mancuso et al., 2016).

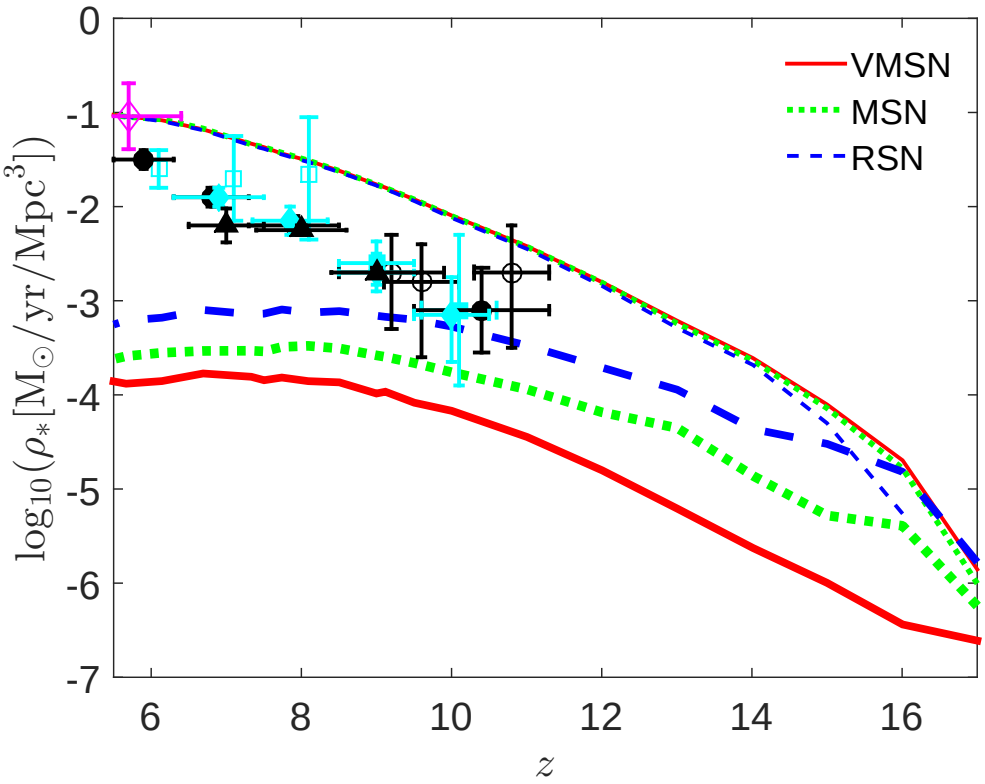

Figure 3.1: Redshift evolution of the intrinsic SFR comoving density in model VMSN (solid red lines), MSN (dotted green) and RSN (dashed blue). The lower set of thick lines denotes the SFR density of PopIII stars, while the upper set of thin lines is the SFR density of PopII/I stars. The data points with error bars show SFR densities derived by UV determinations from: Bouwens et al. (2015) (filled black circles); CLASH data in Zheng et al. (2012), Coe et al. (2013) and Bouwens et al. (2014) (open black circles); McLure et al. (2013); Ellis et al. (2013) (filled cyan diamonds); Oesch et al. (2013, 2014) (filled cyan squares); Duncan et al. (2014) (empty cyan squares) and Laporte et al. (2016) (filled black triangles). IR determinations (empty magenta diamond) are from Rowan-Robinson et al. (2016).

3.2 Results

In the following, I analyse the simulations and show results of the GRB rate evolution, the probability distribution of different class of GRBIIs given one or two metal abundance ratios, and also the properties of GRB host galaxies in the three models[1]. For the metal abundance, I only consider selected elements, such as carbon (C), oxygen (O), silicon (Si) and iron (Fe), since these are the most abundant in the Universe and easier to detect in the spectra of high-z GRB afterglows (Kawai et al., 2006; Castro-Tirado et al., 2013). Sulfur (S) always follows Si and shows a similar behaviour.

3.2.1 GRB rate evolution

In Figure 3.2 I show the redshift evolution of the fraction r_i of GRBII rate which is class i (i.e. PopII-dominated, intermediate or PopIII-dominated):

$$r_i(z) = \frac{\rho_{\mathrm{GRBII},i}(z)}{\rho_{\mathrm{GRBII,tot}}(z)}, \tag{3.2}$$

where $\rho_{\mathrm{GRBII},i}(z)$ is the comoving GRBII rate density in class i sub-sample at redshift z, and $\rho_{\mathrm{GRBII,tot}}(z)$ is the total comoving GRBII rate density at z. In the figure, solid, dashed and dotted lines refer to VMSN, MSN and RSN respectively. The three models show a similar evolution, with the contribution of the PopIII-dominated class decreasing dramatically with redshift, with a fraction of about 1 at $z \gtrsim 17$, but only $\sim 10^{-2}$ at $z = 6$. This is a consequence of the efficient metal enrichment in the early episodes of structure formation. Indeed, after a first short period in which PopIII events in pristine molecular-driven star forming regions dominate, they rapidly leave room to following generations formed in the recently polluted material. Interestingly, although the PopIII SFR is somewhat affected by the PopIII stellar properties (Maio et al., 2010, 2016), the resulting trends are not very sensitive to the scenarios adopted for the first stars IMF. The three cases evolve quite closely, with only a minor delay in the RSN scenario, due to the longer stellar lifetimes and later spreading events (consistently with SN ranges in Table 3.1). The small differences between the trends for VMSN and MSN are due to the different SN explosion energies (lifetimes are comparable), which imply slightly more local enrichment (hence lower PopIII contribution) in the MSN case. For VMSN metals are spread further away from star forming sites and more diluted within the hosting halo.

The contribution of the intermediate class is always between a few per cents and $\sim$ 20%, with a sharp peak at $z \sim 13 - 15$ and a subsequent mild drop. This shape is led by the quick, although transitory, phase of early PopIII enrichment ($f_{\mathrm{III}} > 60\%$) at $z \gtrsim 15$. The first explosions from short-lived stars rapidly enrich the local medium, and the ongoing spreading events from the newly born PopII stars push f_{III} below the 60% threshold (eq. 3.1), causing the steep increase in the figure (green lines). Due to the

[1]While in principle metal absorption observed in the afterglow of GRBs may be due to either the IGM or the ISM, here I assume that it is representative of the host physical properties.

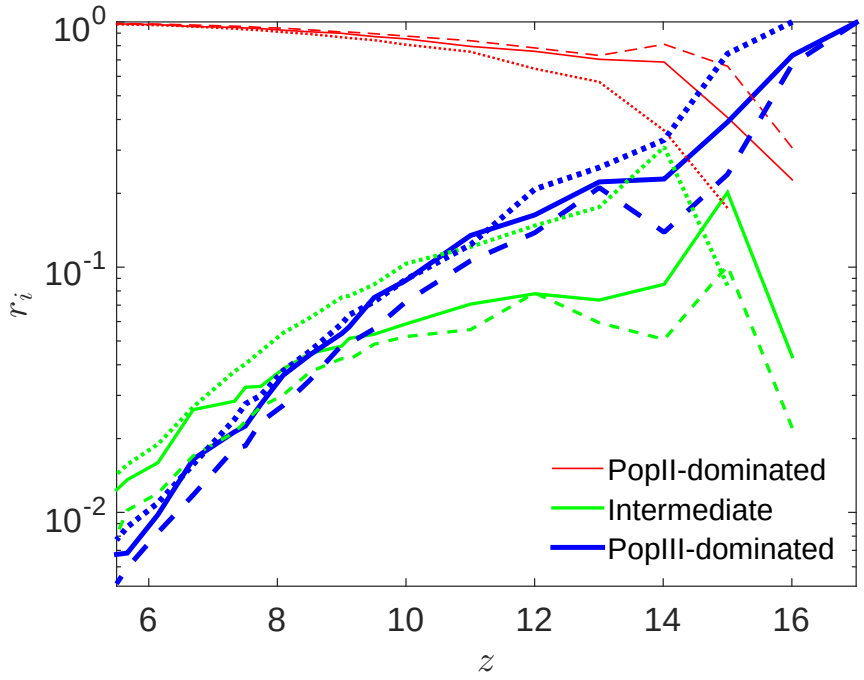

Figure 3.2: Fraction of GRBII rate which comes from PopII-dominated (thin red lines), intermediate (green) and PopIII-dominated (thick blue) gas as a function of redshift z. Solid, dashed and dotted lines denote VMSN, MSN and RSN.

increasingly larger amount of metals being expelled from PopII/I stars with decreasing redshift, the values of $f_{\rm III}$ for many star forming gas particles drop below 20%. Thus, the contribution associated to the intermediate class ($20\% < f_{\rm III} < 60\%$) start to smoothly decrease at $z < 15$.

The trend of the PopII-dominated class is complementary to that of the intermediate and PopIII-dominated ones, and gradually kicks in as an increasingly larger fraction of the gas has PopII progenitors due to metal spreading and stellar evolution, i.e. $r_{\rm PopII-dominated}$ increases quickly with decreasing redshift, and it approaches unity for $z \lesssim 6$.

I note that current data at $z \sim 6$ do not show clear signatures of PopIII-dominated GRBIIs as discussed in chapter 2, and this is in agreement with the results of Figure 3.2 for $r_{\rm PopIII-dominated}$.

With the integration of $\rho_{{\rm GRBII},i}(z)$ along the line of sight, I get the total GRBII number of each class at $z > 5.5$, which is listed in Table 3.2. The three simulations show very similar results, i.e. $\sim 2.8 \times 10^5 {\rm yr}^{-1}{\rm sr}^{-1}$ PopII-dominated GRBIIs, $\sim 8 \times 10^3 {\rm yr}^{-1}{\rm sr}^{-1}$ intermediate GRBIIs and $\sim 6 \times 10^3 {\rm yr}^{-1}{\rm sr}^{-1}$ PopIII-dominated GRBIIs at $z > 5.5$. Because of the limited jet angle of GRBs and also the sensitivity threshold of telescopes, only a small fraction of bright GRBs is observable at high redshift (see further discussion in Campisi et al., 2011), but even if only 0.1% or less of such GRBs were detected, they would open an important observational window on the first stars.

	VMSN	MSN	RSN
PopIII-dominated [$yr^{-1}sr^{-1}$]	6.8×10^3	5.5×10^3	7.0×10^3
intermediate [$yr^{-1}sr^{-1}$]	7.7×10^3	6.0×10^3	9.9×10^3
PopII-dominated [$yr^{-1}sr^{-1}$]	2.8×10^5	2.8×10^5	2.7×10^5

Table 3.2: Number of class i GRBIIs at $z > 5.5$ predicted in model VMSN, MSN and RSN.

3.2.2 Disentangling first stars models

I discuss here how to identify PopIII star signals on the basis of the metal abundance ratios measured in the spectra of high-z GRB optical/NIR afterglows. I also discuss which are the most suitable ratios to look at for constraining the PopIII IMF.

Single metal abundance ratio

Firstly, I study the possibility to identify a PopIII-dominated GRBII from a single metal abundance ratio. Indeed, the measure of two or more ratios may be challenging for very high-z objects, requiring deep NIR spectroscopy early after the GRB event.

The probability distribution of PopIII-dominated GRBIIs at $z \gtrsim 5.5$ as a function of one given abundance ratio is given by:

$$P_i(x) = \frac{1}{\int_x \delta\rho_{\mathrm{GRBII},i}(x)} \frac{\delta\rho_{\mathrm{GRBII},i}(x)}{\delta x}, \tag{3.3}$$

where x denotes one abundance ratio and $\delta\rho_{\mathrm{GRBII},i}(x)$ is the class i GRBII rate density in the interval $[x,\, x + \delta x]$.

In Figure 3.3, I show the probability distributions of [Fe/O], [Si/O], [C/O], [Si/Fe], [Fe/C] and [Si/C] for PopIII-dominated GRBIIs in the VMSN, MSN and RSN case. As a reference, I also plot the distribution for PopII-dominated GRBIIs in each panel (the PopII-dominated PDF coincides in the three cases). I note here that, since the PDFs are normalized to their total rate (see eq. 3.3), PopII-dominated GRBIIs always overwhelm in number the PopIII-dominated ones. Therefore, to safely identify PopIII-dominated GRBIIs one should rely only on metal abundance ratio ranges where PopII-dominated GRBIIs are not present.

Let us analyse Figure 3.3 in more detail. I note that PopII-dominated and PopIII-dominated GRBIIs cover the same range in the [C/O] and [Si/Fe] panels. Therefore, these abundance ratios are not suitable to disentangle PopIII-dominated GRBs in any of my models. The VMSN model shows always the smallest dispersion with a sharp peak at [Fe/O] ≈ -0.2, [Si/O] ≈ 0.5 and [C/O] ≈ -0.6. Although the presence of a peak in the probability distribution is a unique feature of the VMSN model, in most cases this can not be identified because it is swamped by normal PopII-dominated GRBIIs. Therefore, the only unique signature for selecting PopIII-dominated GRBIIs is [Si/C] > 0.7, as this characterizes at least 94% of PopIII-dominated GRBIIs.

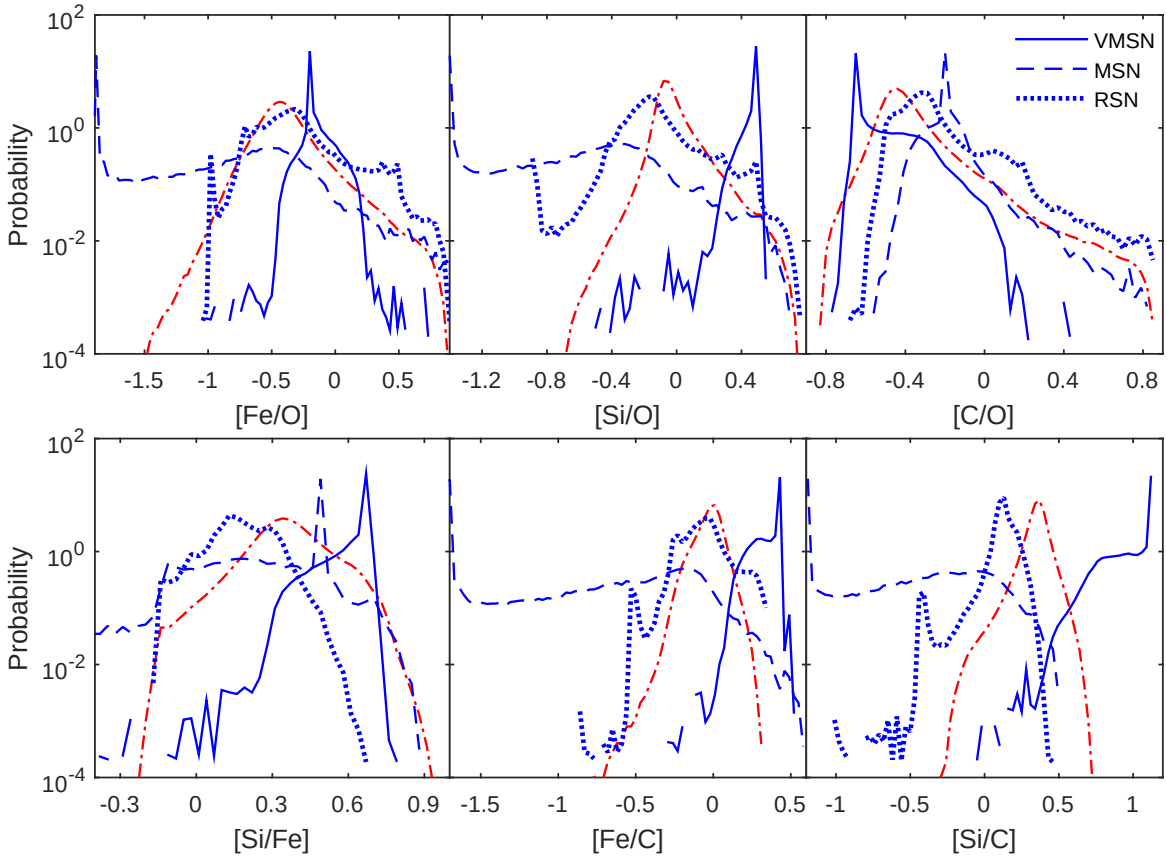

Figure 3.3: Probability distribution of PopIII-dominated GRBIIs given only one abundance ratio (from left to right and top to bottom, it is [Fe/O], [Si/O], [C/O], [Si/Fe], [Fe/C] and [Si/C]) in model VMSN (solid blue lines), MSN (dashed blue lines) and RSN (dotted blue lines). As a reference, the PDF of PopII-dominated GRBIIs is shown as dash-dotted red line in each panel. Note that the PDFs are normalized by the total rate in each class i and therefore, in number, PopII-dominated GRBIIs overwhelm the distribution of PopIII-dominated ones.

The supernova explosions of massive PopIII stars (> 40 M$_\odot$) in the MSN model produce very low iron and silicon yields, but very high carbon and oxygen yields, so that PopIII-dominated GRBIIs in this model peak at very low [Fe/O], [Si/O] and [Fe/C], and can be identified by e.g. [Fe/O] < -1.5, [Si/O] < -1 or [Fe/C] < -0.8. Each of these criteria can discern at least 50-60% of PopIII-dominated GRBIIs. Since the MSN model also includes the contribution from low-mass PopIII stars (with mass < 40 M$_\odot$), it has the largest dispersion in each panel.

Finally, PopIII-dominated GRBIIs in the RSN model have a metal abundance distribution very similar to that of PopII-dominated GRBIIs. Although their distributions are visibly shifted compared to those of PopII-dominated GRBIIs, e.g. in the panel of [Si/O], [C/O] and[Si/C], it would be very difficult to distinguish them from the dominating PopII enriched GRBs.

Two metal abundance ratios

Although I have shown that a single metal abundance ratio could be enough to distinguish PopIII-dominated GRBIIs, their identification would be much easier and more efficient if two or more abundance ratios can be measured.

Figure 3.4 shows the probability density function of hosting a GRBII in environments with given abundance ratios and contribution to metallicity from PopIII stars at redshift $z \gtrsim 5.5$:

$$P_i(x,y) = \frac{1}{\int_x \int_y \delta\rho_{\mathrm{GRBII},i}(x,y)} \frac{\delta\rho_{\mathrm{GRBII},i}(x,y)}{\delta x \delta y}, \tag{3.4}$$

where (x, y) indicate any couple of abundance ratios, while $\delta\rho_{\mathrm{GRBII},i}(x,y)$ is the class i GRBII rate density in the interval $\delta x \times \delta y$ centered in (x, y). Contour levels for probabilities of 25%, 75% and 100%[2] are shown. Left, central and right columns refer to VMSN, MSN and RSN scenarios. Upper, middle and lower rows refer to the bivariate probability distributions for [Si/O] vs [C/O], [Fe/C] vs [Si/C] and [Si/O] vs [O/H], respectively. I note that, since only two metal elements are necessary to plot [Si/O] vs [O/H], the challenge in producing an observational [Si/O] vs [O/H] plot could be the same as that of one single metal abundance ratio, i.e. [Si/O].

Let us consider how different classes of GRBIIs populate the abundance ratio planes for my three simulation runs. I note that the contours for PopII-dominated GRBIIs look very similar in all models, as their metal signature is only little affected ($< 20\%$) by PopIII metal enrichment. In general, the panel [Si/O] vs [C/O] displays [Si/O] values following a roughly linear relation with [C/O], with a peak probability located around [C/O] $= -0.43$ and [Si/O] $= -0.05$. The highest probability in the [Fe/C] vs [Si/C] panels is around solar [Fe/C] and slightly supersolar [Si/C]. The [Si/O] ratios evolve as the local metallicity tracked by [O/H] increases, and they converge to [Si/O] $\simeq -0.05$ for metallicities [O/H] above > -2.

[2]The actual value of the 100% contours is ∼99.8% since in Figure 3.4 I removed particles which are very far away from others.

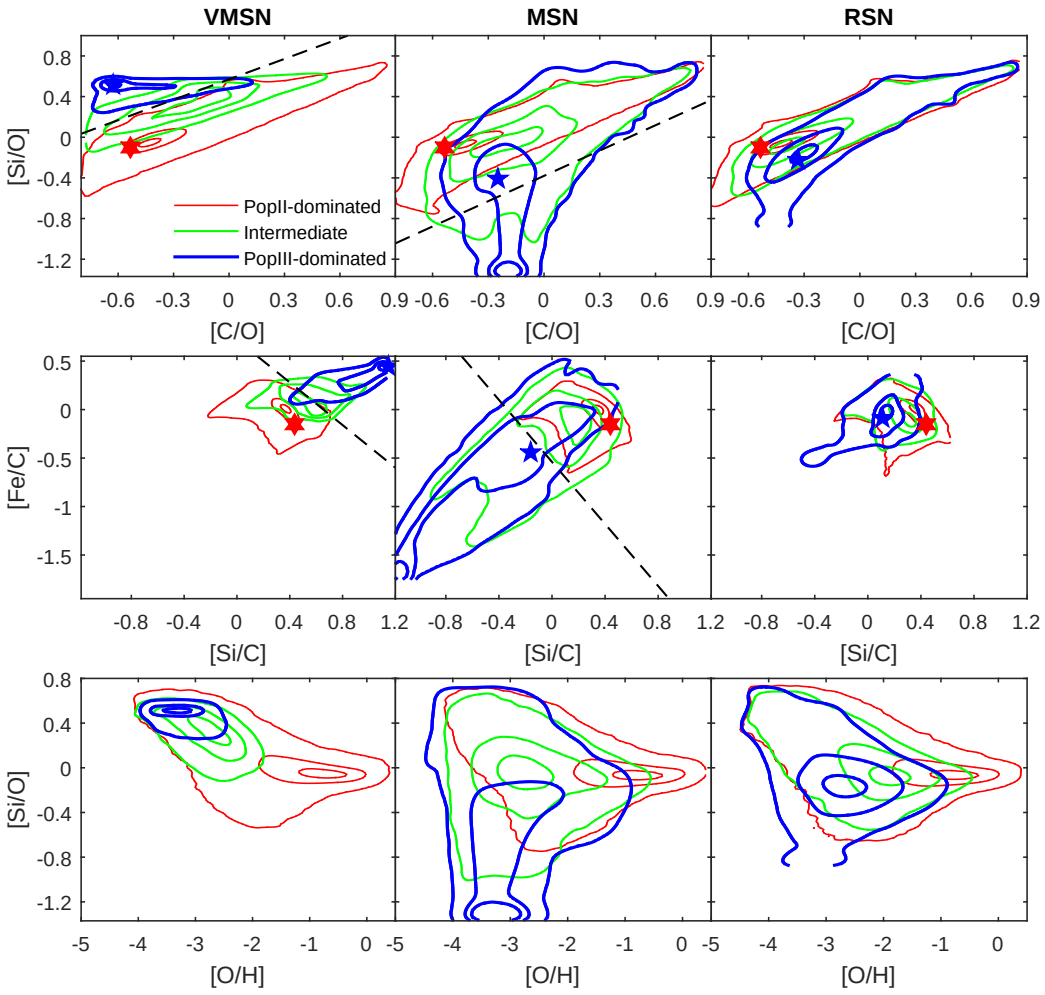

Figure 3.4: Probability of a class i GRBII to have two given abundance ratios in the plane [Si/O] vs [C/O] (top panels), [Fe/C] vs [Si/C] (middle) and [Si/O] vs [O/H] (bottom), for VMSN, MSN and RSN (from left to right) and PopII-dominated (thin red lines), intermediate (green) and PopIII-dominated (thick blue) class. The contours of each color refer to a probability of 25%, 75% and 100% from the innermost to the outermost. The black dashed line in the upper left panel corresponds to [Si/O] = 0.67 [C/O]+0.57, the one in the upper central panel to [Si/O] = 0.83 [C/O]−0.38, the one in the middle left panel to [Fe/C] = −1.1 [Si/C]+0.72, and the one in the middle central panel to [Fe/C] = −1.6 [Si/C]−0.54. The blue pentagrams and red hexagrams denote the IMF-integrated abundance ratios of the stellar yields from PopIII stars and PopII/I stars respectively.

In the VMSN model, PopIII-dominated GRBIIs are located in the upper-left corner of the plane [Si/O] vs [C/O], and can be distinguished from PopII-dominated GRBIIs by selecting those with [Si/O] > 0.67 [C/O]$+0.57$ (black dashed line in the figure). The highest probability to identify a PopIII-dominated GRBII is found around [C/O] ~ -0.62 and [Si/O] ~ 0.51 (almost 75%), which is consistent with the critical conditions [C/O] < -0.5 and [Si/O] > 0 used in the chapter 2 to select GRBIIs enriched by PopIII stars. These can also be identified by selecting [Fe/C] > -1.1 [Si/C]$+0.72$ (black dashed line in the figure), where the probability peaks at [Si/C] ~ 1.11 and [Fe/C] ~ 0.43. The panel [Si/O] vs [O/H] is not able to discriminate PopIII-dominated from PopII-dominated GRBIIs, since the distribution of the latter completely encloses the one of the former.

In the MSN model, [Si/O] and [C/O] values of the PopIII-dominated GRBIIs (upper central panel) have a partial overlap with the PopII-dominated class, although they are also located in different regions. More specifically, at least 70% of them have [Si/O] $<$ 0.83 [C/O]-0.38, since metal yields from PopIII stars with mass [40, 100] $M_\odot$ have high carbon over oxygen yields, but low silicon and iron (Heger & Woosley, 2010). The highest probability is around [C/O] $= -0.19$ and [Si/O] $= -1.37$. The tail distribution of low [Si/C] and [Fe/C] can also be distinguished in the panel [Fe/C] vs [Si/C], with [Fe/C] $<$ -1.6 [Si/C]-0.54. The peak values for the PopIII-dominated objects in the [Si/O] vs [O/H] panel have [Si/O] < -1.2, because the [Si/O] ratio of the metal yields from PopIII stars in the MSN model is much lower than that from PopII/I stars (which have [Si/O] $\simeq 0$), thus the two classes are completely decoupled in such regimes.

In the RSN scenario, the metal yields of PopIII stars are very similar to those from PopII/I stars. As a consequence, the contours of PopIII-dominated class overlap with those of other classes, especially the 100% level, while one can still see some visible, albeit modest, shift for the 25% and 75% contour levels in the same direction as in the MSN case.

Finally, GRBIIs of intermediate class are found to lie between those of the PopII- and PopIII-dominated class in each model.

Irrespectively from the adopted IMF, PopIII-dominated GRBIIs are always found in the low-metallicity range, i.e. at [O/H] $\lesssim -2.0$ (at least for 75% contours) since O traces total metallicity (roughly speaking, about 2/3 of heavy elements is in oxygen species). Going to higher [O/H] values, GRBIIs belong to the intermediate- and PopII-dominated class. This evolution from PopIII- to PopII-dominated class in the different scenarios can be read as a consequence of ongoing mechanical and chemical feedback in the Universe (Maio et al., 2011), which increases the local enrichment level according to the corresponding stellar evolution timescales.

In the panels [Si/O] vs [C/O] and [Fe/C] vs [Si/C], I also show the corresponding IMF-integrated values of the stellar yields from PopIII stars in different models (blue pentagrams) and PopII/I stars (red hexagrams). These values could in principle be used to vaguely identify signatures of PopIII stars, although they rest on limited modeling.

The distribution of abundance ratios, as those obtained with my simulations, are much more powerful tools to characterize environments and yields from different stellar populations. In fact, the advantage of my simulations is that they include a series of physical processes (unaccounted for by simple IMF integration) which could affect the distribu-

tions of GRBIIs and their abundance ratio patterns, e.g. star formation, feedback effects, transition between PopIII and PopII regime, metallicity-dependent stellar lifetimes, metal spreading and so on. On the contrary, the IMF integration only gives one point for each abundance ratio (as shown in Figure 3.4).

3.2.3 GRB host properties

In Figure 3.5, I show the PopIII-dominated and PopII-dominated SFR weighted distributions of the properties of GRBII host galaxies in the three models. I focus on total metallicity Z (top panels), stellar mass $M_\star$ (middle) and SFR (bottom). The weights to the corresponding distributions are computed as $\mathrm{SFR}_{i,k}/\mathrm{SFR}_{i,\mathrm{tot}}$, where $\mathrm{SFR}_{i,k}$ is the total class i SFR of galaxies in the kth bin, and $\mathrm{SFR}_{i,\mathrm{tot}}$ is the integral of class i SFR over all galaxies. Here I include all the host galaxies at redshift $z \gtrsim 5.5$. In each panel of the figure, the blue dashed line shows the probability for a GRBII hosted in a given galaxy to be PopIII-dominated, i.e. $\mathrm{SFR}_{i,k}/\mathrm{SFR}_{\mathrm{tot},k}$, where $\mathrm{SFR}_{\mathrm{tot},k}$ is the total SFR of galaxies in the kth bin.

A simple example can better clarify this: let's consider the VMSN model distribution in terms of SFR (bottom-left box). Although the PopIII-dominated GRBII distribution (solid black line) peaks at $\mathrm{SFR} \sim 10^{-2}\,\mathrm{M_\odot\,yr^{-1}}$, the probability to find a PopIII-dominated GRBII in a galaxy (dashed blue) with $\mathrm{SFR} \sim 10^{-2}\,\mathrm{M_\odot\,yr^{-1}}$ is only 20%. On the other hand, while a rarer event, the identification of a GRBII in a galaxy with $\mathrm{SFR} \leq 10^{-3}\,\mathrm{M_\odot\,yr^{-1}}$ would clearly point towards a PopIII-dominated GRB.

As expected, the different first star models have little effect on the distribution of the properties of PopII-dominated GRBII hosts (dotted red lines), since the PopII/I regime becomes dominant shortly after the onset of star formation. More specifically, most of the PopII-dominated GRBIIs are hosted in galaxies with $Z > 10^{-2.5}\,\mathrm{Z_\odot}$, with a peak at $Z = 10^{-1.5}\,\mathrm{Z_\odot}$. Their stellar mass spans the range $(10^5 - 10^{9.5})\,\mathrm{M_\odot}$, peaking around $10^{7.5}\,\mathrm{M_\odot}$. Finally, their SFR is in the range $(10^{-2.5} - 10)\,\mathrm{M_\odot\,yr^{-1}}$, with a peak at $10^{-0.5}\,\mathrm{M_\odot\,yr^{-1}}$. These results are consistent with those found by Salvaterra et al. (2013) and seem to hold for all models.

The metallicity distribution of PopIII-dominated GRBII hosts (solid black lines) shares similar features among the three models. For example, all of them have a peak at $Z \sim 10^{-2}\,\mathrm{Z_\odot}$ and a second one in the range $Z \sim (10^{-4.6} - 10^{-3.4})\,\mathrm{Z_\odot}$. The presence of the $Z \sim 10^{-2}\,\mathrm{Z_\odot}$ peak can be explained by residual PopIII star formation in the outskirts of already evolved galaxies (e.g. Tornatore et al. 2007a; Maio et al. 2010). These events can push metallicities close to PopII-dominated ones (red dotted lines). However, most PopIII-dominated GRBII hosts show metallicities lower than those of PopII-dominated hosts. In the VMSN and MSN models, the majority of other PopIII-dominated GRBIIs are in galaxies with very low metallicity ($Z \leq 10^{-4}\,\mathrm{Z_\odot}$), while in the RSN model the peak of the distribution is at $Z \sim 10^{-3.5}\,\mathrm{Z_\odot}$. This happens as the SFR of PopIII stars in the RSN model is much higher. Although the metal pollution is delayed, a large number of small mass PopIII stars can enrich the galaxies very fast and thus few galaxies have $Z < 10^{-4}\,\mathrm{Z_\odot}$. For all models, the probability to find a PopIII-dominated GRBII (dashed

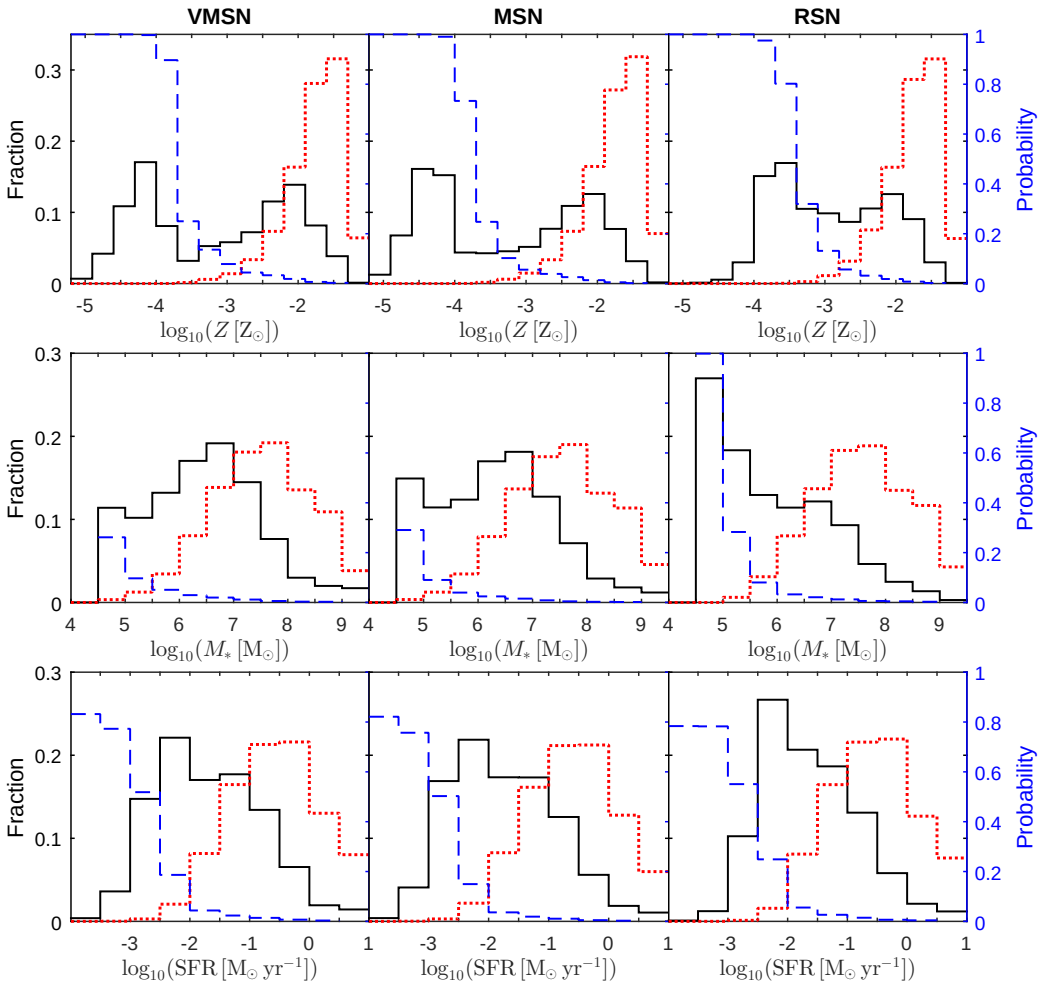

Figure 3.5: From top to bottom, metallicity, stellar mass and SFR distribution of galaxies hosting GRBIIs. The solid black (dotted red) lines are the distributions of galaxies weighted by the PopIII-dominated (PopII-dominated) PopII SFR; while the dashed blue lines refer to the probability for a GRBII hosted in a given galaxy to be PopIII-dominated. From left to right, the columns refer to model VMSN, MSN and RSN.

blue lines) becomes lower than 10% in galaxies with $Z > 10^{-3}\,Z_{\odot}$.

The stellar mass of PopIII-dominated GRBII hosts in all models is distributed mainly within the range $(10^{4.5} - 10^{7.5})$ $M_{\odot}$, lower than that of PopII-dominated GRBII hosts. However, while in the VMSN and MSN models a peak is present at $M_* \sim 10^{6.5}$ $M_{\odot}$, in the RSN model ∼60% of PopIII-dominated GRBIIs are found in galaxies in the lower stellar mass of the range, i.e. $(10^{4.5} - 10^{6})$ $M_{\odot}$, with a prominent peak at 10^5 $M_{\odot}$. For any stellar mass, the probability of a given galaxy to host PopIII-dominated GRBIIs is very low in the VMSN and MSN model, i.e. PopIII-dominated GRBIIs are not sensitive to the stellar mass of their hosts. In the RSN model, instead, galaxies with $M_* < 10^5\,M_{\odot}$ only host PopIII-dominated GRBIIs. In fact, metal enrichment from PopIII stars in the RSN model is weaker and delayed (stellar lifetimes are up to 10 times longer than for VMSN), resulting in the survival of more pristine stars.

The three models also have similar SFR distributions for PopIII-dominated GRBII hosts. The most populated range is $(10^{-3}-10^{-0.5})$ $M_{\odot}\,yr^{-1}$, with a peak at $\sim 10^{-2}$ $M_{\odot}\,yr^{-1}$, about 1 dex lower than that of PopII-dominated GRBII hosts. In all models, the probability of hosting PopIII-dominated GRBIIs goes from 80% for galaxies with SFR $< 10^{-3}$ $M_{\odot}\,yr^{-1}$ to 5% for those with SFR $> 10^{-2}$ $M_{\odot}\,yr^{-1}$, with only a few PopIII-dominated GRBIIs in galaxies with SFR > 1 $M_{\odot}\,yr^{-1}$.

3.3 Discussion and Conclusions

The abundance ratios of PopIII-dominated GRBIIs are expected to be very sensitive to the predicted metal yields from PopIII stars, that in turn depend on a number of physical processes in the stellar cores (differential rotation, the initial composition, magnetic fields, nuclear reaction rates, explosion mechanisms, etc.), which are still theoretically uncertain. For example, massive first stars (i.e. with mass $> 40\,M_{\odot}$ in the MSN model) can explode both as faint supernovae and hypernovae, depending on the angular momentum of the resulting black hole (Nomoto et al., 2013). The former case produces small heavy element yields (e.g. iron; Heger & Woosley 2010; Nomoto et al. 2013), which could explain the abundance ratios of carbon-enriched metal poor (CEMP) stars observed in the Milky Way. In this case, PopIII-dominated GRBIIs in my MSN model can be identified with the abundance ratios and used to study first stars. The latter case has higher silicon and iron yields, and could be the reason for carbon-unenhanced metal poor stars (Umeda & Nomoto, 2005). Their abundance ratios are very similar to those of PopII/I stars, thus it would be difficult to separate those PopIII-dominated GRBIIs from the PopII-dominated ones.

A different PopIII IMF slope may also have an effect on the abundance ratio distributions, especially in the MSN model, by shifting the peak distribution discussed in Section 3.2.2. However, the ranges of abundance ratios which I focus on are only mildly affected, as they are mainly driven by the adopted SN mass range (Maio et al., 2010).

I should additionally note that physical processes in the interstellar medium are described by means of sub-grid models, which have also been tested through simulations of isolated objects (e.g. Maio et al., 2013b). The effects of changing specific model parameters

have been shown to be mild for star formation and enrichment, as long as the gas cooling is properly accounted for both atomic and molecular phases, as in my simulations.

Most of my results are weighted by the GRBII rates in the gas particles of the corresponding classes. I have considered that most PopIII stars are located either in the outskirts of massive galaxies (Tornatore et al., 2007b) or in low-mass galaxies (Maio et al., 2011; Wise et al., 2012; Biffi & Maio, 2013; Maio et al., 2016), i.e. further away from the typical location of PopII stars. This means that GRBIIs exploding in these environments are more likely to retain information from PopIII rather than from PopII/I stars. A weighting by other properties, e.g. the gas or the metal mass of the particles, would give results very similar to those I have presented, especially concerning the criteria to identify the first star signal.

Theoretically, the amplitude of metal absorption lines depends on the GRB afterglow luminosity, the spectral shape and also the ionization status of the interstellar medium. To investigate this in more details, one would need to model the luminosity and spectrum of the afterglow (e.g. Ciardi & Loeb, 2000), as well as the ionization status and dust fraction of the interstellar gas at very high resolution (Mancini et al., 2015, 2016; Bocchio et al., 2016).

Compared to recent afterglow observations of high-z GRBs, e.g. GRB 111008A (Sparre et al., 2014) and GRB 130606A (Hartoog et al., 2015), I find that most of the absorption lines of carbon, oxygen, silicon and iron (except several Fe lines) would be observable even at $z > 10$ with VLT/X-Shooter.

I highlight that I have defined the dominance of a population according to the fraction of heavy elements coming from PopIII stars, $f_{\rm III}$, with PopIII- and PopII-dominated regimes having $f_{\rm III} > 60\%$ and $f_{\rm III} < 20\%$, respectively. Nevertheless, I have verified that the exact boundaries used for my classification (within $\pm 10\%$ variations) do not have a relevant impact on the final outcome.

I can summarize my main results as follows.

- The fraction of second generation GRBs exploded in a medium enriched by PopIII stars (PopIII-dominated GRBIIs) is independent from the adopted first stars model. This fraction rapidly decreases with redshift, accounting for $\sim 30\%$ of GRBII at $z = 15$, 10% at $z = 10$, but only 1% at $z = 6$. Since the PopII SFR is almost independent from the mass spectrum of PopIII stars, also the observable rate of PopIII-dominated GRBIIs is hardly affected by it.

- I have explored the possibility to identify PopIII-dominated GRBIIs from observations of abundance ratios. Although not very efficient, a single ratio could in principle be enough to select PopIII-dominated GRBIIs in the VMSN and MSN model. In the former case, a unique signature is represented by a high [Si/C] ratio, i.e. [Si/C] > 0.7. In the latter, PopIII-dominated GRBIIs can be identified by [Fe/O] < -1.6, [Si/O] < -1, or [Fe/C] < -0.8.

- PopIII-dominated GRBIIs are more easily selected using two abundance ratios. For massive or very massive SN models, the probability distribution shows memory of

the adopted IMF, allowing to distinguish the two. In the VMSN model, PopIII-dominated GRBIIs are found at [Si/O] > 0.67 [C/O]$+0.57$ or [Fe/C] > -1.1 [Si/C]$+0.72$, whereas in the MSN model, at least 70% of them are within the limits of [Si/O] $<$ 0.83 [C/O]-0.38 or [Fe/C] < -1.6 [Si/C]-0.54. On the other hand, as metal yields from PopIII SN explosions in the RSN model are very similar to those of PopII/I SNe, in this case it is not feasible to distinguish PopIII- from PopII-dominated GRBIIs.

- The properties of galaxies hosting PopIII-dominated GRBIIs are not strongly affected by the assumption on the mass of the first stars. Generally, these galaxies have metallicity $(10^{-4.5} - 10^{-1})$ $Z_\odot$, stellar mass $(10^{4.5} - 10^{7.5})$ $M_\odot$ and SFR $(10^{-3} - 10^{-0.5})$ $M_\odot\,yr^{-1}$, all lower than those of the normal PopII-dominated GRBII hosts. Additionally, the GRBIIs observed in host galaxies with $Z < 10^{-4}\,Z_\odot$ are most likely PopIII-dominated.

Chapter 4

Metal enrichment signatures of the first stars on high redshift DLAs

In this chapter, I use the same simulations presented in Chapter 3 to study how gas pollution in primordial gas (in particular DLAs) changes with the properties of the first stars. In the analysis, I only consider galaxies with a minimum of 200 gas particles in order to prevent numerical artifacts (e.g. de Souza et al., 2013; Maio et al., 2013a; Salvaterra et al., 2013). I also exclude metal-free galaxies to focus on the metal enrichment originated by PopIII and PopII/I pollution. Similar to the procedure in chapter 3, I use $f_{\rm III}$ of each galaxy to describe the level of metal enrichment from first stars, i.e. "PopII-dominated" if $f_{\rm III} < 20\%$, "intermediate" if $20\% < f_{\rm III} < 60\%$, and "PopIII-dominated" if $f_{\rm III} > 60\%$.

In the following, the DLA definition and properties are presented in section 4.1, the results for simulated metal abundances of galaxies are shown in section 4.2, and the main conclusions in this chapter are discussed in section 4.3.

4.1 Damped Lyman-Alpha Absorbers

In the following, I first introduce the definition of a DLA in the simulations and then discuss the properties of PopIII/PopII-dominated DLAs as well as their evolution with redshift.

4.1.1 DLA definition

Observationally, a DLA is defined as a structure with column density of neutral hydrogen $N_{\rm HI} > 2 \times 10^{20}\,{\rm cm}^{-2}$ along the line of sight of QSOs (Wolfe et al., 2005). To correctly evaluate the ionization fraction of neutral hydrogen within the cosmic medium in numerical simulations, the radiative transfer of ionizing photons should be accounted for.

Given the ability of the implementation to capture gas physics and chemistry down to very low temperatures, here I prefer to select DLAs in the simulations following the procedure of e.g. Maio et al. (2013a) and Maio & Tescari (2015), i.e. gaseous objects with

gas temperature $T \leq 10^4\,\mathrm{K}$ (consistently with e.g. Cooke et al., 2015). As a reference, early gas objects selected in this way at $z = 7$ have $N_{\mathrm{HI}} \gtrsim 3 \times 10^{20}\,\mathrm{cm}^{-2}$, gas masses $\lesssim 2 \times 10^8\,\mathrm{M}_\odot$ and typical metallicities $Z \lesssim 10^{-3}\,\mathrm{Z}_\odot$.

Alternatively, I also consider the description of DLAs in terms of a mass-dependent neutral hydrogen cross-section (as done in e.g. Kulkarni et al., 2013), which is parametrized through a fit calibrated against $z = 3$ observations (see also Pontzen et al., 2008; Font-Ribera et al., 2012; Kulkarni et al., 2013):

$$\Sigma(M_{\mathrm{halo}}) = \Sigma_0 \left(\frac{M_{\mathrm{halo}}}{M_0}\right)^2 \left(1 + \frac{M_{\mathrm{halo}}}{M_0}\right)^{\alpha-2}, \tag{4.1}$$

where $\alpha = 0.2$, $M_0 = 10^{9.5}\,\mathrm{M}_\odot$ and $\Sigma_0 = 40\,\mathrm{kpc}^2$ at $z = 3$. This fitting function matches very well the column density distribution function observed at low z (Kulkarni et al., 2013). However, I note that a possible bias may appear for high-z DLAs, due to the fact that the fit is calibrated to reproduce data at $z = 3$.

To aid the assessment of the impact of such definitions on my results, I discuss below some general galactic properties. In Fig. 4.1, I present the distribution of PopII-dominated, intermediate and PopIII-dominated galaxies in the three simulations in terms of mass-weighted temperature T vs dark-matter halo mass M_{halo} at redshift $z = 9.5$ (circles), 7.5 (crosses) and 5.5 (diamonds) in the VMSN, MSN and RSN model.

At each redshift, PopII-dominated galaxies show very similar T vs M_{halo} distributions in the three models, i.e. their mass and temperature are weakly affected by the first star model adopted. As expected, more massive galaxies appear with decreasing redshift. E.g. at $z = 5.5$ halo masses are between $10^{8.5}\,\mathrm{M}_\odot$ and $10^{11.5}\,\mathrm{M}_\odot$, with corresponding gas temperatures ranging from $10^3\,\mathrm{K}$ to several $10^5\,\mathrm{K}$, while at $z = 9.5$ the halo masses are $< 10^{10}\,\mathrm{M}_\odot$. The more massive galaxies usually have higher gas temperature, as a consequence of their deeper potential well, higher SFR and stellar mass.

Also the distributions of PopIII-dominated galaxies are very similar in all models, with halo masses $M_{\mathrm{halo}} < 10^{9.6}\,\mathrm{M}_\odot$ and temperatures $T < 10^{4.5}\,\mathrm{K}$, lower than those of the PopII-dominated galaxies. No significant redshift evolution is evident here, since PopIII metal pollution usually dominates in low-mass galaxies, where gas parcels feature mostly pristine composition, irrespectively from redshift. Higher-mass objects are statistically more evolved and have experienced already bursts of star formation and metal spreading.

The halo mass and gas temperature of intermediate galaxies are very close to those of PopIII-dominated galaxies, with a few rare exceptions. The paucity of intermediate-class galaxies is due to the rapidity of metal enrichment, which is quickly dominated by PopII/I star formation (i.e. $f_{\mathrm{III}} < 20\%$). Due to the different stellar lifetimes, metal spreading from first PopIII SNe is delayed in the RSN model with respect to the VMSN and MSN models. Therefore, the PopIII SFR reaches higher levels and more prolonged durations, delaying the transition from intermediate to PopII-dominated galaxies (i.e. more galaxies retain $f_{\mathrm{III}} > 20\%$). For this reason, intermediate galaxies are more abundantly present in the RSN model than in the VMSN and MSN models.

From Fig. 4.1 it is clear that the two theoretical definitions of DLAs are expected to affect the results on the predicted properties. Indeed, since PopIII-dominated objects

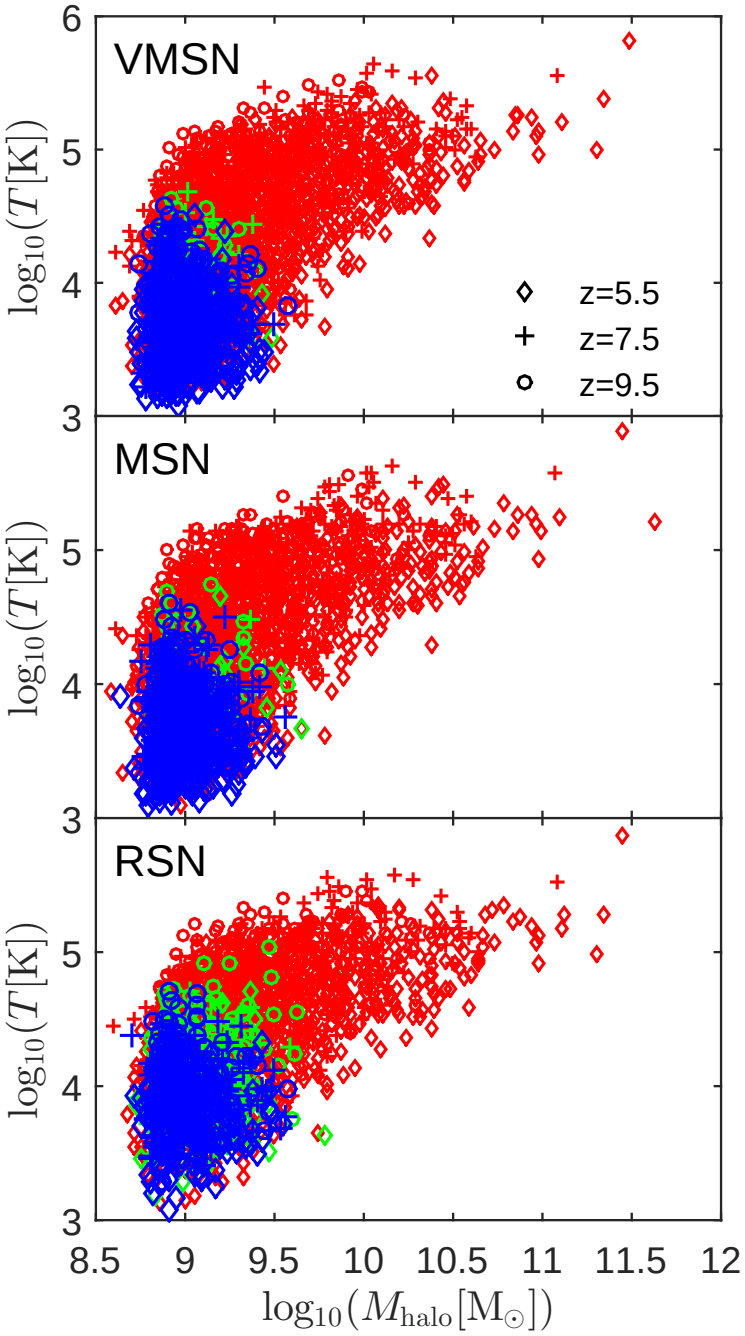

Figure 4.1: Distribution of mass-weighted temperature (T) of PopII-dominated (small red symbols), intermediate (green) and PopIII-dominated (big blue) galaxies as a function of halo mass ($M_{\rm halo}$). The results are shown at $z = 9.5$ (circles), 7.5 (crosses) and 5.5 (diamonds). From top to bottom, the panels refer to the VMSN, MSN and RSN model.

have very low gas temperatures, most of them could be DLA candidates when selected with the temperature threshold $T \leq 10^4\,\mathrm{K}$ (in the following referred to as "temperature selected"), while PopII-dominated ones, populating the high-mass end of the distribution, would dominate the DLAs when selected according to eq. 4.1 ("mass selected"). The differences of these two approaches are also discussed in Morrison et al. (2016). In the following, the evolution and the statistical properties of DLAs selected with both criteria will be shown.

4.1.2 Evolution of PopII/PopIII-dominated DLAs

In Fig. 4.2 I show the evolution of the fraction of PopIII-dominated (top panel) and PopII-dominated (bottom panel) DLAs as a function of redshift, according to both DLA definitions. For temperature selected DLAs (thin lines), the fraction is defined as $N_i(z)/N_{\mathrm{tot}}(z)$, where $N_i(z)$ is the number of class i DLAs and $N_{\mathrm{tot}}(z)$ is the total number of all classes DLAs at redshift z. For mass selected DLAs (thick lines) the fraction of class i is computed as $\Delta_i(z)/\Delta_{\mathrm{tot}}(z)$, where $\Delta_i(z)$ is sum of $\Sigma(M_{\mathrm{halo}})$ of class i galaxies and $\Delta_{\mathrm{tot}}(z)$ is the integral of $\Sigma(M_{\mathrm{halo}})$ of all galaxies at redshift z.

Consistently with what mentioned in the previous section, the fraction of PopIII-dominated DLAs decreases with redshift because of the increasing metal contribution from PopII/I stars. This is almost independent from the first stars model, although the RSN model shows slightly lower PopII-dominated values than the others, as a result of the delayed metal pollution from smaller-mass first stars that have longer stellar lifetimes. On the other hand, while temperature selected DLAs have a very high probability to be PopIII-dominated, e.g. 80% at $z = 10$ and 40% at $z = 6$, the corresponding fraction for mass selected DLAs is only 10% at $z = 10$ and 3% at $z = 6$. The difference is caused by the fact that PopIII-dominated galaxies are likely to have $T \leq 10^4\,\mathrm{K}$ and small hosting halo masses (see Fig. 4.1). These characteristics are strongly disfavoured when using the fit of eq. 4.1 (which gives a larger weight to typically hotter objects with masses $\gtrsim 10^{9.5}\mathrm{M}_\odot$).

The fraction of PopII-dominated DLAs is complementary to that of PopIII-dominated ones. It turns to be very high for mass selected DLAs, with fractions exceeding 80% at $z = 10$ and increasing with decreasing redshift. This trend is due to the adopted fit in eq. 4.1, which favors more massive PopII-dominated galaxies. On the contrary, temperature selected PopII-dominated DLAs feature fractions of just 20% at $z = 10$ and 60% at $z = 5.5$, as more massive galaxies are excluded by the temperature selection criterion.

From these results, I also conclude that the fraction of intermediate DLAs is rather low for both definitions. Precisely, it is $< 4\%$ in the VMSN and MSN models and only slightly larger in the RSN model (see also Fig. 4.1 and Fig. 4.4).

Although the fraction of PopIII-dominated DLAs becomes larger at higher redshifts, the total DLA number density is lower at earlier epochs, because less structures are present. Thus, to predict how many high-z DLAs are observable as PopIII-dominated, I calculate the expected cumulative fraction of all DLAs at $z \geq 5.5$ that are PopIII-dominated. For

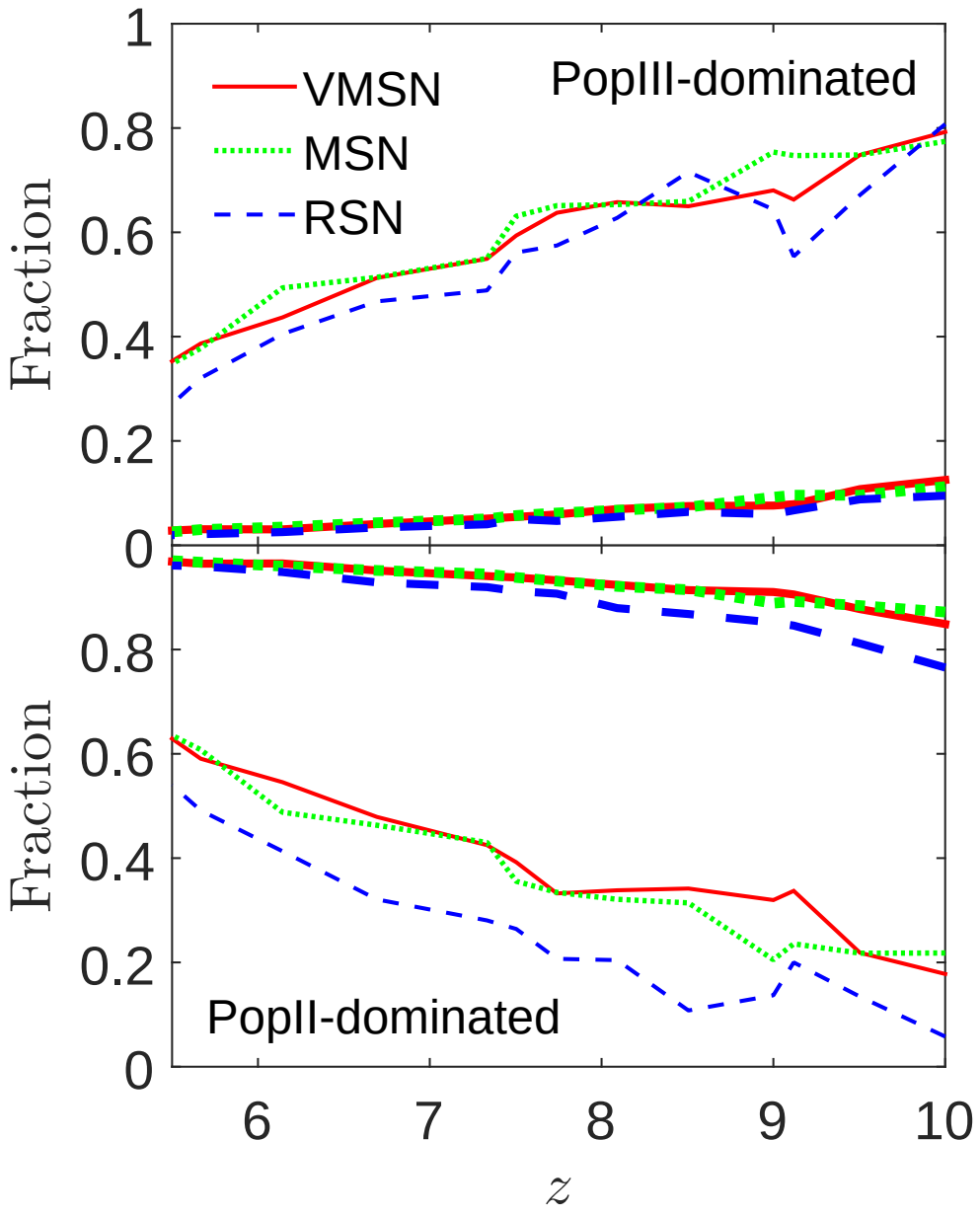

Figure 4.2: Redshift evolution of the fraction of DLAs which are PopIII-dominated (top) and PopII-dominated (bottom) in models VMSN (solid red lines), MSN (dotted green) and RSN (dashed blue). The thin and thick sets of curves refer to temperature selected DLAs and mass selected DLAs, respectively.

temperature selected DLAs, it is computed by:

$$\int_{z>5.5} \mathrm{d}z' \; N_i(z')\Phi(z')\frac{\mathrm{d}V}{\mathrm{d}z'} \Big/ \int_{z>5.5} \mathrm{d}z' \; N_{\mathrm{tot}}(z')\Phi(z')\frac{\mathrm{d}V}{\mathrm{d}z'}, \tag{4.2}$$

where $\Phi(z') \propto 10^{-0.5*z'}$ denotes the quasar number at redshift $> z'$ (Fan et al., 2001), $\mathrm{d}V/\mathrm{d}z' = D^2\frac{\mathrm{d}D}{\mathrm{d}z'}\mathrm{d}\Omega$ indicates the comoving cosmic volume and $D(z')$ is the comoving distance between redshift z' and 0. Considering that the number of observable DLAs also depends on the number of background sources, the cumulative fraction is weighted by the number of background quasars (Fan et al., 2001). I get a value 42.5%, 43.6% and 36.5% for the VMSN, MSN and RSN model, respectively. For mass selected DLAs, this cumulative fraction is expressed as

$$\int_{z>5.5} \mathrm{d}z' \; \Delta_i(z')\Phi(z')(1+z')^2\frac{\mathrm{d}D}{\mathrm{d}z'} \Big/ \int_{z>5.5} \mathrm{d}z' \; \Delta_{\mathrm{tot}}(z')\Phi(z')(1+z')^2\frac{\mathrm{d}D}{\mathrm{d}z'}, \tag{4.3}$$

giving 3.4%, 3.5% and 2.6% for VMSN, MSN and RSN, respectively.

4.1.3 DLA properties

In Fig. 4.3 I show the distribution of halo mass, metallicity and SFR of PopIII-dominated (blue thick lines) and PopII-dominated (red thin lines) DLAs at redshift $z \geq 5.5$, from all the three simulations.

For temperature selected DLAs (solid lines) the distribution is computed by:

$$\int_{z>5.5} \mathrm{d}z' N_{i,j}(z')\Phi(z')\frac{\mathrm{d}V}{\mathrm{d}z'} \Big/ \int_{z>5.5} \mathrm{d}z' N_{i,\mathrm{tot}}(z')\Phi(z')\frac{\mathrm{d}V}{\mathrm{d}z'}, \tag{4.4}$$

where $N_{i,j}(z')$ is the number of class i DLAs in the j-th bin at redshift z', and $N_{i,\mathrm{tot}}(z')$ is the total number of class i DLAs at z'. For mass selected DLAs (dotted lines), the distribution is calculated by:

$$\int_{z>5.5} \mathrm{d}z' \Delta_{i,j}(z')\Phi(z')(1+z')^2\frac{\mathrm{d}D}{\mathrm{d}z'} \Big/ \int_{z>5.5} \mathrm{d}z' \Delta_{i,\mathrm{tot}}(z')\Phi(z')(1+z')^2\frac{\mathrm{d}D}{\mathrm{d}z'}, \tag{4.5}$$

where $\Delta_{i,j}(z')$ is the sum of $\Sigma(M_{\mathrm{halo}})$ of class i DLAs in the j-th bin at z', and $\Delta_{i,\mathrm{tot}}(z')$ is the sum of $\Sigma(M_{\mathrm{halo}})$ of all class i DLAs at z'.

In all the three models, the properties of PopII-dominated DLAs (red lines) feature major differences according to the selection criteria. Specifically, temperature selected PopII-dominated DLAs (solid red lines) have very low halo masses $M_{\mathrm{halo}} < 10^{9.6}\,\mathrm{M}_\odot$, while metallicities are concentrated in the range $10^{-4.5} - 10^{-2}\,\mathrm{Z}_\odot$ and peak around $Z \approx 10^{-3}\,\mathrm{Z}_\odot$. The SFRs are $< 10^{-1.5}\ \mathrm{M}_\odot\,\mathrm{yr}^{-1}$.

Since eq. 4.1 suppresses low-mass structures and imposes a roughly flat trend of neutral hydrogen cross-section for big structures, the mass selected PopII-dominated DLAs (dotted red lines) have flatter halo mass distributions with $M_{\mathrm{halo}} > 10^{8.8}\,\mathrm{M}_\odot$ and a peak at $\approx$

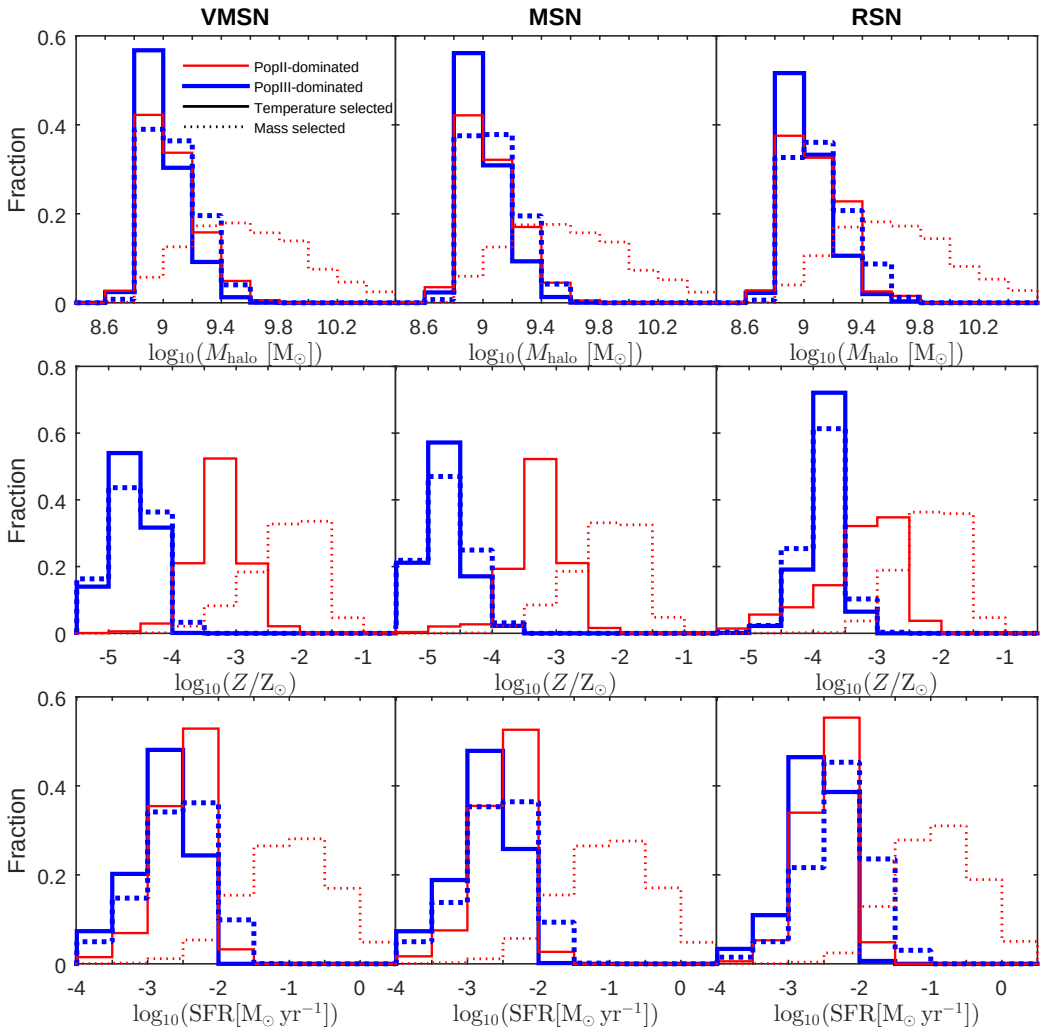

Figure 4.3: From top to bottom, halo mass [$M_\odot$], metallicity [$Z_\odot$] and SFR [$M_\odot$ yr^{-1}] distribution of PopII-dominated (red thin lines) and PopIII-dominated (blue thick lines) DLAs at $z \geq 5.5$, in base-10 logarithmic scale. Solid lines indicate temperature selected DLAs, while dotted lines indicate mass selected DLAs. From left to right, the columns refer to model VMSN, MSN and RSN.

$10^{9.6}\,M_\odot$. Their metallicities are in the range $(10^{-3.5} - 10^{-1})\,Z_\odot$ and peak at $\approx 10^{-2}\,Z_\odot$, which is 1 dex higher than those of temperature selected ones. They also show larger SFRs ($> 10^{-2.5}\,M_\odot\,yr^{-1}$), that peak at $\approx 0.1\,M_\odot\,yr^{-1}$.

As the two DLA definitions select similar samples of PopIII-dominated galaxies (see Fig. 4.1), the distributions of PopIII-dominated DLAs (blue lines) show similar trends, although mass selected ones (dotted lines) have usually slightly higher mass, metallicity and SFR.

In all the first star models, PopIII-dominated DLAs are typically hosted in halos with mass $M_{\rm halo} < 10^{9.6}$ $M_\odot$ (also see Fig. 4.1), consistently with e.g. Kulkarni et al. (2013) and Maio & Tescari (2015), and peak at $\approx 10^9$ $M_\odot$. Their typical metallicities are as expected lower than those of PopII-dominated DLAs, i.e. $Z < 10^{-4}$ $Z_\odot$ in the VMSN and MSN model, and 10^{-5} $Z_\odot < Z < 10^{-3}$ $Z_\odot$ in the RSN model, since the higher small-mass PopIII SFR in the RSN model induces more metal pollution in low-mass galaxies. PopIII-dominated DLAs also have a SFR lower than that of PopII-dominated ones, with SFR $< 10^{-1.5}\,M_\odot\,yr^{-1}$ and a peak around $\approx 10^{-2.5}\,M_\odot\,yr^{-1}$.

In the three models, characteristic trends of PopII/PopIII-dominated DLAs are clearly visible for the mass selected case (dotted lines), no matter in terms of host halo mass, metallicity or SFR. Temperature selected PopII-dominated (red solid lines) DLAs present halo mass and SFR distributions very similar to those of the PopIII-dominated ones (blue solid lines), while they still can be neatly identified through metallicities, though. In fact, most PopIII-dominated DLAs have $Z < 10^{-3.5}\,Z_\odot$, while only a few temperature selected PopII-dominated DLAs reach such low values.

4.2 DLA Metal Abundances

In this section, I present the results for metal abundance ratios of indicative heavy elements extracted by my simulations. I focus on carbon (C), oxygen (O), silicon (Si) and iron (Fe), which are abundant in galaxies and have been detected in high-z DLAs (Becker et al., 2012; Morrison et al., 2016).

4.2.1 Abundance ratios

In Fig. 4.4 I show distributions of abundance ratios at redshift $z = 9.5$, 7.5 and 5.5 for, respectively, 617, 1496 and 2581 metal enriched galaxies in the VMSN model; 608, 1508 and 2590 in the MSN model; and 512, 1332 and 2370 in the RSN model. The RSN model features fewer (by $\approx 16\%$ at $z = 9.5$, $\approx 11\%$ at $z = 7.5$ and $\approx 8\%$ at $z = 5.5$) metal polluted galaxies than the other models due to the longer lifetimes of small-mass first stars that delay the initial phases of cosmic metal enrichment.

All these galaxies are DLA candidates when selected according to the mass criterium, while only 10%-30% of them are DLAs when selected according to their temperature. I have verified that this smaller sample of DLAs retains the same characteristics of the metal ratio distributions of the full sample. This is because the metal abundance ratios of galaxies are

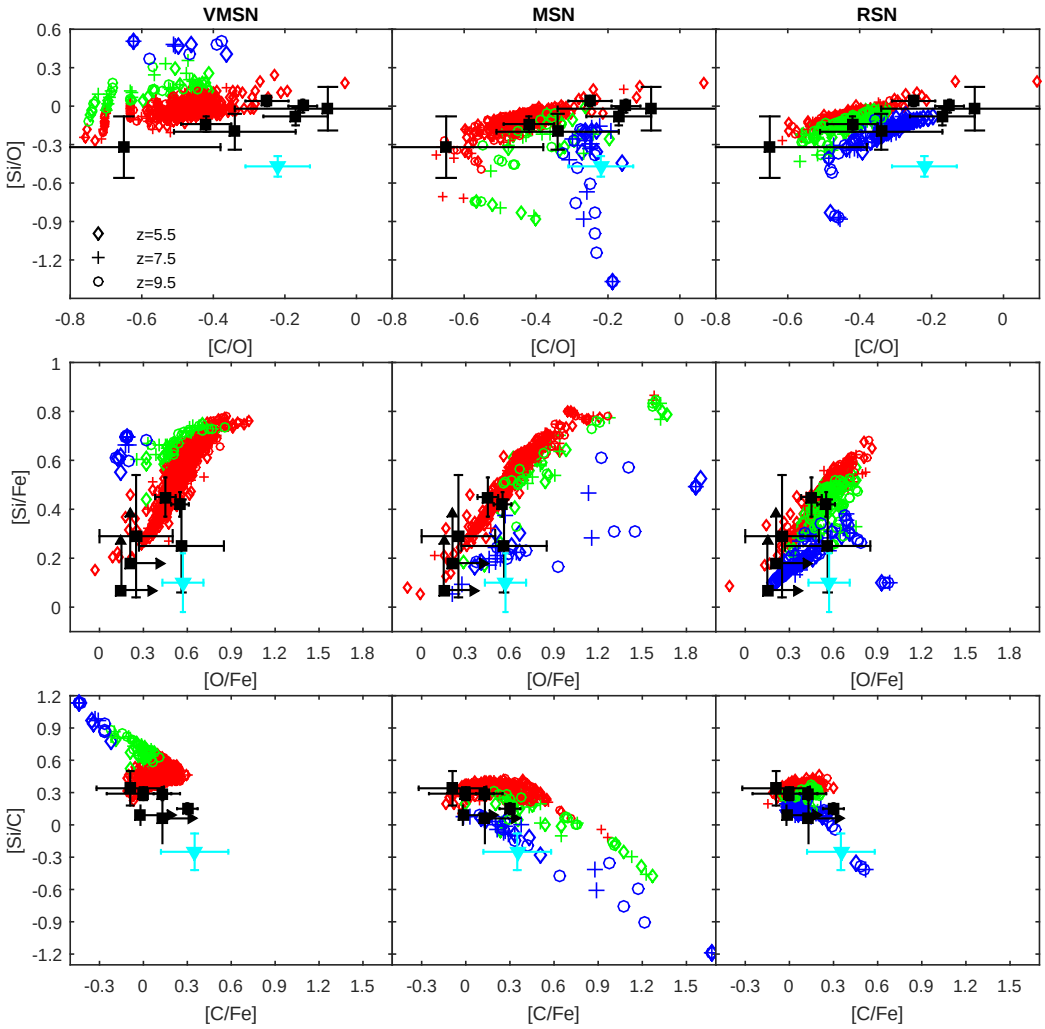

Figure 4.4: Distributions of abundance ratios [Si/O] vs [C/O] (top panels), [Si/Fe] vs [O/Fe] (central) and [Si/C] vs [C/Fe] (bottom). From left to right the columns refer to models: VMSN, MSN and RSN. The symbols denote PopII-dominated (small red), intermediate (green) and PopIII-dominated (big blue) galaxies at $z = 9.5$ (circles), 7.5 (crosses) and 5.5 (diamonds). Black solid squares with error bars (or arrows to denote lower or upper limits) are DLAs observed in the redshift range $5.3 - 6.2$ (Becker et al. 2012), while the cyan solid triangle refers to a DLA at $z = 5$ reported by Morrison et al. (2016).

mainly determined by the yields of the polluting stellar population, and thus are weakly dependent on the halo mass or gas temperature. For this reason, the distributions are representative of the DLA population, independently from the selection. In the remaining of this chapter I will thus refer to abundance ratios of DLAs rather than of galaxies.

From Fig. 4.4 PopII-dominated, intermediate and PopIII-dominated DLAs are clearly separated in the panels [Si/O] vs [C/O], [Si/Fe] vs [O/Fe] and [Si/C] vs [C/Fe] for the VMSN and MSN models, while in the RSN model they mostly overlap.

More specifically, PopII-dominated DLAs (red symbols) have abundance ratios very similar in the three models, indicating their common origin (i.e. pollution by the same PopII generation). A linear correlation between [Si/O] and [C/O] is evident, due to the different metal pollution phase in each galaxies. The [Si/O] ratios of most PopII-dominated DLAs are between -0.2 and 0.1, while typically [C/O] are in the range $[-0.6, -0.3]$. A few cases at $z = 5.5$ have [C/O] > -0.3 due to pollution by local AGB stars, whose contribution becomes relevant at such epochs as a consequence of AGB lifetimes[1]. PopII-dominated DLAs also show a roughly linear relation between [Si/Fe] and [O/Fe], and they are preferentially located in regions where [O/Fe] $= [0.3, 0.9]$ and [Si/Fe] $= [0.2, 0.7]$. Some have very low [O/Fe] and [Si/Fe] ratios at $z = 5.5$, resulting from metal spreading from low-mass stars dying as SNIa (with high iron yields) that becomes increasingly important with decreasing redshift. In the [Si/C] vs [C/Fe] panel, PopII-dominated DLAs in the three models share the region delimited by [C/Fe] $= [-0.1, 0.3]$ and [Si/C] $= [0.2, 0.5]$. Some differences appear, though. E.g. DLAs with [Si/C] > 0.5 are present only in the VMSN model as a result of the high [Si/C] yields (≈ 1.14) from PISN. Then, only the MSN model has some PopII-dominated DLAs with [C/Fe] > 0.3 because of the very low iron yields expected for faint supernovae from massive first stars (Heger & Woosley, 2010).

The distributions of PopIII-dominated DLAs (blue symbols) are visibly different in the three models and do not show obvious time evolution. Thanks to the large explosion energy of PISN and the short lifetime of very massive PopIII stars, PopIII-dominated DLAs in the VMSN model are mostly concentrated in a small region of the [Si/O] vs [C/O] panel with [C/O] ≈ -0.62 and [Si/O] ≈ 0.51. Similarly, these PopIII-dominated DLAs typically have [O/Fe] ≈ 0.18 vs [Si/Fe] ≈ 0.7 and [C/Fe] ≈ -0.44 vs [Si/C] ≈ 1.14. PopIII-dominated DLAs in the VMSN model might have [C/O] and [O/Fe] similar to those of PopII-dominated and intermediate DLAs, but higher [Si/O] and [Si/Fe], e.g. [Si/O] > 0.3.

Since the MSN model includes PopIII metal enrichment both from massive stars ($> 40\,\mathrm{M}_\odot$, that have very high carbon and oxygen but low silicon and iron yields when exploding as faint supernovae), and from regular stars ($< 40\,\mathrm{M}_\odot$, whose metal yields are very similar to those of PopII stars), a number of PopIII-dominated DLAs have [Si/O] ≈ -1.37 and [C/O] ≈ -0.19, and some are closer to PopII-dominated DLAs, while others are located in between, as a result of the combined contribution of massive and low-mass PopIII stars. The same effects also appear in the distribution of [Si/Fe] vs [O/Fe], i.e. some PopII-dominated DLAs have [O/Fe] ≈ 1.9 and [Si/Fe] ≈ 0.5, while others are located around

[1] AGB stars evolve in a few 10^8 yr, hence they can enrich the medium already at $z \sim 6$ by spreading metals via mass loss.

[O/Fe] ≈ 0.5 and [Si/Fe] ≈ 0.2. In the [Si/C] vs [C/Fe] panel, PopIII-dominated DLAs are distributed in the range [C/Fe] $= [0, 1.68]$ and [Si/C] $= [-1.2, 0]$.

The metal yields of pristine supernovae with small-mass progenitors are similar to those from PopII/I stars, thus PopIII-dominated DLAs in the RSN model are located very close to PopII-dominated and intermediate DLAs, although some differences are also visible. For example, given the same [C/O] (or [O/Fe]), PopIII-dominated DLAs present [Si/O] (or [Si/Fe]) ≈ 0.2 dex lower than that of PopII-dominated DLAs, and they also have a smaller [Si/C] (< 0.2).

Intermediate DLAs (green symbols) always locate between PopII-dominated and PopIII-dominated ones. They are relatively few in the VMSN and MSN model when compared to the RSN model, as mentioned earlier. Since massive PopII stars (e.g. with mass $> 30\,\mathrm{M}_\odot$) have stellar lifetimes much shorter than low-mass ones, intermediate DLAs retain some features of the pollution from massive PopII stars, e.g. by having [C/O] ratios lower, but [Si/Fe] ratios higher than the PopIII-dominated DLAs, which are the typical features of PopII stars with mass $> 30\,\mathrm{M}_\odot$.

The unique characteristics shown by PopIII-dominated DLAs in the abundance ratios can be exploited to identify first star signatures and constrain PopIII mass ranges by comparing them to DLAs observed at $z \geq 5$ with high precision abundance ratios (Becker et al. 2012; Morrison et al. 2016). These are listed in Table 4.1 and shown as symbols in Fig. 4.4.

QSO	z	[Si/O]	[C/O]	[Si/C]	[C/Fe]	[O/Fe]	[Si/Fe]
SDSS J1202+3235	5.0	-0.47 ± 0.08	-0.22 ± 0.09	-0.25 ± 0.17	0.35 ± 0.23	0.57 ± 0.14	0.10 ± 0.12
SDSS J0231-0728	5.3380	-0.14 ± 0.06	-0.42 ± 0.07	0.29 ± 0.06	0.13 ± 0.06	0.55 ± 0.06	0.42 ± 0.05
SDSS J0818+1722	5.7911	0.00 ± 0.05	-0.15 ± 0.04	0.15 ± 0.05	0.30 ± 0.07	0.45 ± 0.07	0.45 ± 0.08
SDSS J0818+1722	5.8765	-0.08 ± 0.07	-0.17 ± 0.09	0.09 ± 0.09	> - 0.02	>0.15	>0.07
SDSS J1148+5251	6.0115	0.04 ± 0.04	-0.25 ± 0.06	0.29 ± 0.06	-0.00 ± 0.25	0.25 ± 0.25	0.29 ± 0.25
SDSS J1148+5251	6.1312	-0.32 ± 0.24	-0.65 ± 0.27	0.34 ± 0.16	-0.09 ± 0.23	0.56 ± 0.29	0.25 ± 0.19
SDSS J1148+5251	6.1988	-0.20 ± 0.14	-0.34 ± 0.17	0.14 ± 0.12	...	...	...
SDSS J1148+5251	6.2575	-0.02 ± 0.17	-0.08 ± 0.26	0.06 ± 0.23	>0.13	>0.21	>0.18

Table 4.1: Abundance ratios of DLAs observed at $z \geq 5$. The first measurement is from Morrison et al. (2016), while the others are from Becker et al. (2012).

Most of data points are consistent with PopII-dominated DLAs, although some of them have error bars too large to draw definitive conclusions. Meanwhile, some data points seem to favor the MSN and RSN models, although no observation can clearly discriminate one model over the others.

The DLA at $z = 5.8765$ found along the line-of-sight of QSO SDSS J0818+1722 is very close to the PopIII-dominated DLAs in the RSN model, as indicated by the [Si/O] vs [C/O] panel, as well as by the ratio [Si/C]$= 0.09 \pm 0.09$. Nevertheless, there are only lower limits for its [Si/Fe] and [O/Fe], which can not then be used to set more stringent constraints on its class and progenitors.

The DLA at $z = 5.7911$ is also consistent with PopIII-dominated objects in the RSN model in the [Si/O] vs [C/O] panel, while it clearly locates in the region of PopII-dominated DLAs in the [Si/Fe] vs [O/Fe] panel.

All abundance ratios of the recently observed DLA at $z = 5$ from QSO SDSS J1202+3235 (Morrison et al., 2016) are consistent with PopIII-dominated DLAs in the MSN model, although it does not display the features characteristic of faint supernovae, e.g. very low [Si/O] (< -1) or very high [C/Fe] (> 1). Its abundance ratios are also close to those of PopIII-dominated DLAs in the RSN model in the panel [Si/C] vs [C/Fe], but they are not fully consistent with the same model in the panel [Si/O] vs [C/O].

4.2.2 Evolution of DLA mean abundance ratios

In Fig. 4.5, I show the evolution of the average [C/O], [Si/C] and [C/Fe] for DLAs selected under both definitions. As mass selected DLAs are dominated by massive halos with metal abundances predominantly coming from PopII stars, their mean abundance ratios (thick lines) are weakly dependent on the first stars model and present a mild evolution with redshift (Kulkarni et al., 2013). Instead, the mean abundance ratios of temperature selected DLAs (thin lines) are dramatically different in the three models and show an evident redshift evolution as a result of their larger fraction of PopIII-dominated DLAs.

Specifically, since PopIII stars in all three models have [C/O] yields similar to those of PopII stars, the mean [C/O] ratios of DLAs present differences of only 0.3 dex for the temperature selected ones, and 0.1 dex for the mass selected ones. In most cases, the mean [C/O] rises slowly with decreasing redshift, reaching ≈ -0.4 at $z = 5.5$, as a result of the increasing contribution from AGB stars. In the VMSN model, this behaviour is also partly caused by the low [C/O] yields of PISN (< -0.6). PISN pollution is mostly significant at high redshift, so at $z = 10$ the mean [C/O] is ≈ -0.6 (≈ -0.5) for temperature (mass) selected DLAs. However, temperature selected DLAs in the MSN model show an exception, i.e. their mean [C/O] decreases with decreasing redshift, since the massive first stars, that exploding as faint supernovae with high [C/O] yields (≈ -0.2), result into a high mean [C/O] ratio at $z = 10$, while as redshift decreases the mean [C/O] is gradually reduced by the growing contribution of PopII stars that have low [C/O] yields (≈ -0.4).

PopIII-dominated DLAs have very high (low) [Si/C] in the VMSN (MSN) (see also bottom panels in Fig. 4.4), thus the average [Si/C] values of DLAs feature the largest differences in the three models, e.g. $\approx$ 1.8 dex ($\approx$ 0.4 dex) for temperature selected

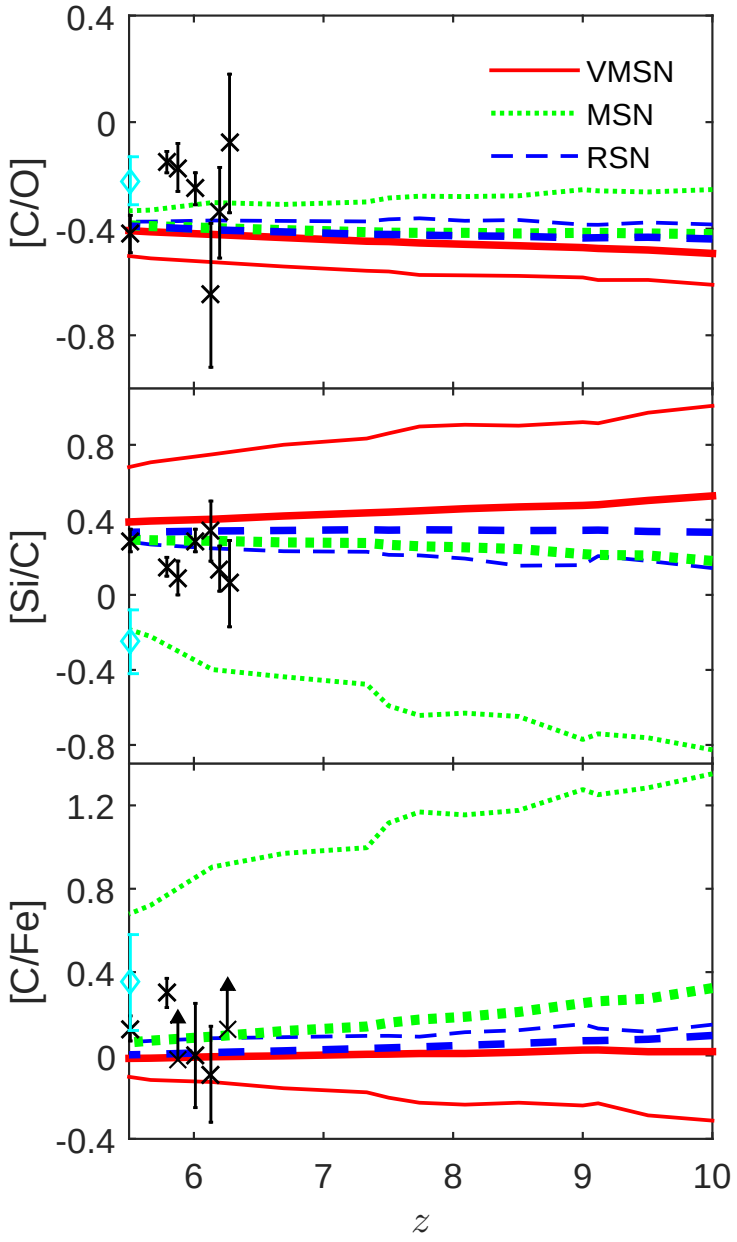

Figure 4.5: Mean value of [C/O] (top), [Si/C] (middle) and [C/Fe] (bottom) in the VMSN (solid red lines), MSN (dotted green) and RSN (dashed blue) models as a function of redshift. The thin and thick curve sets denote temperature selected and mass selected DLAs, respectively. The black crosses with error bars (or arrows) are data for observed DLAs taken from Becker et al. (2012), and the one showed as cyan diamond with error bar is from Morrison et al. (2016).

(mass selected) DLAs at $z = 10$. As redshift decreases, the contribution from PopIII stars becomes less important, hence the [Si/C] ratio in both VMSN and MSN model tends to converge to that of the RSN model, with [Si/C] ≈ 0.3.

The mean [C/Fe] ratios in the RSN model are ≈ 0, but slowly decrease with decreasing redshift. This might be caused by SNIa events that start contributing to metal enrichment at $z \approx 6$ and injecting important amounts of iron. Because of the low [C/Fe] yields of PISN, the temperature selected DLAs in the VMSN model present a low [C/Fe] (≈ -0.3) at $z = 10$, but it increases with decreasing redshift and finally converges to the RSN trend. On the other hand, mass selected DLAs in the VMSN model have [C/Fe] very similar to that of the RSN model, as a result of their smaller fraction of PopIII-dominated DLAs (see Fig. 4.2). With large [C/Fe] yields from faint supernovae, the average [C/Fe] in the MSN model is higher than those in any other model, e.g. [C/Fe] ≈ 1.3 (≈ 0.3) for temperature selected (mass selected) DLAs at $z = 10$. Although [C/O] measurements would not help in discriminating any models, it is possible to infer interesting conclusions from observational data of [Si/C] and [C/Fe]. The predicted mean metal ratios of mass selected DLAs, for all three models, are consistent with the observed high-z DLAs (see also Kulkarni et al., 2013), although they have some difficulties in reproducing the observation by Morrison et al. (2016) for [Si/C] and [C/Fe]. Temperature selected DLAs (thin lines) feature trends similar to the ones obtained by mass selection in the RSN model, while they show higher (lower) mean [Si/C] in the VMSN (MSN) model, as well as higher [C/Fe] in the MSN model. These latter features are in tension with [Si/C] and [C/Fe] data by Becker et al. (2012), but explain the data of Morrison et al. (2016) by MSN enrichment.

I note that the various differences may be caused by a bias in the observations, since PopIII-dominated DLAs with such low metallicity (i.e. $Z < 10^{-3.5}\,\mathrm{Z}_\odot$) are not easy to detect (Wolfe et al., 2005).

4.3 Discussion and Conclusions

In my analysis, I explore the DLAs from simulations with two possible selection criteria: the first one selects DLAs as gaseous objects with mass-weighted temperature $T < 10^4\,\mathrm{K}$ (temperature selected DLAs; e.g. Cooke et al. 2015), and the other one is based on the associated neutral hydrogen cross-section (mass selected DLAs; as in e.g.Kulkarni et al. 2013).

My main results in this chapter can be summarized as follows:

- The fraction of DLAs that are PopIII-dominated decreases quickly with decreasing redshift, almost independently from the first star models. However, it is dramatically affected by the selection criteria for DLAs, as it can be as high as 40% at $z = 6$ for temperature selected DLAs, but only 3% for mass selected ones.

- PopIII-dominated DLAs have very low halo mass ($< 10^{9.6}\mathrm{M}_\odot$), metallicities ($< 10^{-4}\mathrm{Z}_\odot$ in the VMSN and MSN model and $< 10^{-3}\mathrm{Z}_\odot$ in the RSN model) and SFR ($< 0.01\mathrm{M}_\odot\,\mathrm{yr}^{-1}$), without much dependence on the selection criteria.

- PopII-dominated DLAs, instead, display different properties under the two adopted definitions. While temperature selected PopII-dominated DLAs show halo mass and SFR distributions very similar to those of PopIII-dominated ones and ≈ 1 dex larger metallicities, mass selected PopII-dominated DLAs span a larger mass range, i.e. $(10^{8.6} - 10^{10.6})$ $M_\odot$, and favor larger metallicity ($> 10^{-3.5}\,Z_\odot$ and a peak at $10^2\,Z_\odot$) and SFRs ($> 10^{-2.5}\,M_\odot\,yr^{-1}$ and a peak at $0.1\,M_\odot\,yr^1$).

- No matter which definition I adopt, the PopIII-dominated DLAs could be easily identified through their abundance ratios in the VMSN and MSN models (and possibly also in the RSN model), e.g. by comparing [Si/O] vs [C/O], [Si/Fe] vs [O/Fe] or [Si/C] vs [C/Fe]. Besides, the average abundance ratios of DLAs (e.g. [C/O], [Si/C] and [C/Fe]) from all the simulations display a visible difference at high redshift, but converge quickly with decreasing redshift.

- Current DLA observations at $z \geq 5$ (Becker et al., 2012; Morrison et al., 2016) do not support the VMSN model, but at least one is consistent with the first star signatures in the MSN and RSN models. Despite more precise observations are necessary in the future, these results seem consistent with the conclusions drawn from the most metal-poor DLA currently known (Cooke et al., 2017), which point towards enrichment from lower-mass stars to explain observed low-metallicity gas patterns.

Chapter 5

Conclusions and Prospects

Supported by a development of science in general and technology, in the last century astronomy has witnessed a dramatic development as well. One associated benefit is that research of the first stars has become feasible. Although direct observations are still lacking, people can now study the first stars with numerical simulations, as well as indirect observations. From numerical simulations, we know that the first stars are formed at redshift $z \sim 30$. While most simulations show that the first stars are more massive than normal stars, their initial mass function is still matter of a lively debate. Their metal yields and released energy are also predicted from simulations of stellar evolution, and they are expected to be different from those of normal stars. Indirect observations are mostly contributed by metal poor stars in the local Universe, and suggest that the first stars should be massive but not very massive.

As the contribution of the first stars is expected to be much more significant in the early Universe, in this thesis I studied the first star signatures on high-z PopII GRBs and DLAs, using numerical N-body/hydrodynamic simulations. The simulations include large scale evolution, galaxy formation, atomic and molecular cooling and star formation, and also the metal enrichment from stars.

Specifically, in Chapter 2, I presented the results about the high-z GRBs hosted in a medium enriched by first stars (PopIII-dominated). In this chapter, I only concentrated on a very massive first star model ($m_* = [100, 500]\,\mathrm{M}_\odot$), and studied the fraction of GRBs which are PopIII-dominated, their predicted observable rate, and also the properties of the host galaxies. I found that the fraction of PopIII-dominated GRBs decreases quickly with decreasing redshift, e.g. $\sim$10% of GRBs at $z = 10$ are expected to retain signatures from the first stars, but this fraction is only $\sim$1% at $z = 6$. The host galaxies of PopIII-dominated GRBs have very low stellar masses, $\mathrm{M}_\star \sim 10^{4.5} - 10^7\,\mathrm{M}_\odot$, star formation rates, $\mathrm{SFR} \sim 10^{-3} - 10^{-1}\,\mathrm{M}_\odot/\mathrm{yr}$, and metallicities, $Z \sim 10^{-4} - 10^{-2}\,\mathrm{Z}_\odot$. I also compared my results with currently observed high-z GRBs, finding that e.g. GRB 130606A at $z = 5.91$ and GRB 111008A at $z = 5.0$ have no obvious metal features from first stars. One reason could be that the observational accuracy is still not good enough, i.e. the error bar for abundance ratio is still too large. Another reason might be the expected very low fraction of PopIII-dominated GRBIIs ($\sim 1\%$) in this redshift range.

In Chapter 3, I run three simulations with different mass ranges and the corresponding lifetimes and metal yields for the PopIII stars, to study the effects of first star models on the GRB rates and the host galaxies, i.e. (*i*) a Very Massive SN (VMSN) model with mass range [100, 500] $M_\odot$ in which metal pollution is driven by PISN with [140, 260] $M_\odot$; (*ii*) a Massive SN (MSN) model with mass range [0.1, 100] $M_\odot$ where metals are produced by SNe with [10, 100] $M_\odot$; and (*iii*) a Regular SN (RSN) model which is the same as the MSN model, but here the enrichment is done by SNe with masses of [10, 40] $M_\odot$. Interestingly, I found that the fraction of GRBs which are PopIII-dominated is independent from the first star models. In all three first star models, the host galaxies of PopIII-dominated GRBIIs show very low metallicity, SFR and stellar mass. I also studied how to distinguish the first star models using the observations of high-z GRBs. I found that the signatures of first stars with different masses could be identified with the metal abundance ratios derived from the absorption lines in the GRBII afterglow spectra, e.g. [Si/O] vs [C/O] or [Fe/C] vs [Si/C] would distinguish the VMSN and MSN models. In the RSN model the first star signatures are less obvious (and could not be distinguished with observations of metal abundance ratios) because the metal yields of low mass first stars are very close to those of PopII stars.

In Chapter 4, I used the same three simulations to study high-z DLAs that may retain signatures from the first stars. In addition, two different criteria are adopted to select DLAs in the simulations, i.e. based on the mass-weighted temperature being $< 10^4$ K (temperature selected), or defined by the cross-section of neutral hydrogen (mass selected). I found that $\sim 40\%$ ($\sim 3\%$) of DLAs at $z > 5.5$ would contain first stars signatures in the case of temperature selected (mass selected) galaxies. The properties (e.g. halo mass, SFR, and metallicity) of PopIII-dominated DLAs are not sensitive to the selection criteria, although those of PopII-dominated DLAs are. Generally, PopIII-dominated DLAs can only be galaxies with very low metallicity ($< 10^{-3.5}\,Z_\odot$), and their halo masses are typically $< 10^{9.6}\,M_\odot$. The first stars with different masses would leave an imprint on the metal ratios of DLAs, e.g. [Si/O] vs [C/O], [Si/Fe] vs [O/Fe], and [Si/C] vs [C/Fe] could be used to constrain the first star models. By comparing the simulation results with current observations, I found that the observed DLAs at $z > 5$ favor the massive and low mass first star model more than the very massive first star model.

In conclusion, high-z GRBs and DLAs could be excellent tools to study the first stars. With the next generation of telescopes, more objects at high-z will be discovered, making it possible to reveal the nature of the first stars.

However, several important issues are ignored in my thesis, that need my further exploration. First, the first mass IMF may change with the evolution of primordial molecular clouds, that would make metal ratio patterns also evolve with redshift. In this case, abundant samples of observations should be able to constrain the first star evolution, but further research in this direction is still needed to better understand the various details. Second, it is still not known if the PopIII stars enriched regions are large enough to imprint clear signals on the spectra of GRBs or QSOs. In other words, if PopIII stars can not enrich a large enough region to affect the GRB/QSO spectra, we probably could not identify them in the observations. Third, while dust formation and destruction would also change

the metal components in the gas medium, this kind of studies at high-z are still currently missing. These issues could also change the possibility to detect the first star signatures in high-z GRBs/DLAs using current or future telescopes. So, I will continue to work on these topics in the near future.

Bibliography

Abel T., Bryan G. L., Norman M. L., 2002, Science, 295, 93

Akerman C. J., Carigi L., Nissen P. E., Pettini M., Asplund M., 2004, A&A, 414, 931

Asplund M., Grevesse N., Sauval A. J., Scott P., 2009, ARA&A, 47, 481

Bardeen J. M., Bond J. R., Kaiser N., Szalay A. S., 1986, ApJ, 304, 15

Baumgartner W. H., Loewenstein M., Horner D. J., Mushotzky R. F., 2005, ApJ, 620, 680

Becker G. D., Sargent W. L. W., Rauch M., Carswell R. F., 2012, ApJ, 744, 91

Beers T. C., Christlieb N., 2005, ARA&A, 43, 531

Biffi V., Maio U., 2013, MNRAS, 436, 1621

Bocchio M., Marassi S., Schneider R., Bianchi S., Limongi M., Chieffi A., 2016, in Supernova Remnants: An Odyssey in Space after Stellar Death, p. 134

Booth C. M., Theuns T., Okamoto T., 2007, MNRAS, 376, 1588

Bouwens R. J. et al., 2016, ApJ, 833, 72

Bouwens R. J. et al., 2014, ApJ, 795, 126

Bouwens R. J. et al., 2015, ApJ, 803, 34

Bromm V., 2013, Reports on Progress in Physics, 76, 112901

Campana S., Salvaterra R., Ferrara A., Pallottini A., 2015, A&A, 575, A43

Campana S. et al., 2012, MNRAS, 421, 1697

Campana S., Salvaterra R., Tagliaferri G., Kouveliotou C., Grindlay J., 2011, MNRAS, 410, 1611

Campbell S. W., Lugaro M., Karakas A. I., 2010, A&A, 522, L6

Campisi M. A., Maio U., Salvaterra R., Ciardi B., 2011, MNRAS, 416, 2760

Capak P. L. et al., 2015, Nature, 522, 455

Castro-Tirado A. J. et al., 2013, ArXiv:1312.5631

Cescutti G., Matteucci F., McWilliam A., Chiappini C., 2009, A&A, 505, 605

Chen K.-J., Bromm V., Heger A., Jeon M., Woosley S., 2015, ApJ, 802, 13

Chen X., Miralda-Escudé J., 2008, ApJ, 684, 18

Chornock R., Berger E., Fox D. B., Lunnan R., Drout M. R., Fong W.-f., Laskar T., Roth K. C., 2013, ApJ, 774, 26

Ciardi B., Loeb A., 2000, ApJ, 540, 687

Clark P. C., Glover S. C. O., Smith R. J., Greif T. H., Klessen R. S., Bromm V., 2011, Science, 331, 1040

Coe D. et al., 2013, ApJ, 762, 32

Cooke R., Pettini M., Murphy M. T., 2012, MNRAS, 425, 347

Cooke R., Pettini M., Steidel C. C., Rudie G. C., Nissen P. E., 2011, MNRAS, 417, 1534

Cooke R. J., Pettini M., Jorgenson R. A., 2015, ApJ, 800, 12

Cooke R. J., Pettini M., Steidel C. C., 2017, MNRAS

Cucchiara A. et al., 2011, ApJ, 736, 7

Dahlen T. et al., 2004, ApJ, 613, 189

de Souza R. S., Mesinger A., Ferrara A., Haiman Z., Perna R., Yoshida N., 2013, MNRAS, 432, 3218

Dilday B. et al., 2012, Science, 337, 942

Dodelson S., 2003, Modern cosmology

Duncan K. et al., 2014, MNRAS, 444, 2960

Ellis R. S. et al., 2013, ApJ, 763, L7

Fan X. et al., 2001, AJ, 121, 54

Ferrara A., Viti S., Ceccarelli C., 2016, MNRAS, 463, L112

Font-Ribera A. et al., 2012, JCAP, 11, 59

Frebel A., Norris J. E., 2015, ARA&A, 53, 631

Ghirlanda G. et al., 2013, MNRAS, 428, 1410

Ghirlanda G., Nava L., Ghisellini G., Firmani C., 2007, A&A, 466, 127

Greiner J. et al., 2009, ApJ, 693, 1610

Hartoog O. E. et al., 2015, A&A, 580, A139

Heger A., Woosley S. E., 2002, ApJ, 567, 532

Heger A., Woosley S. E., 2010, ApJ, 724, 341

Hirano S., Hosokawa T., Yoshida N., Omukai K., Yorke H. W., 2015, MNRAS, 448, 568

Hirano S., Hosokawa T., Yoshida N., Umeda H., Omukai K., Chiaki G., Yorke H. W., 2014, ApJ, 781, 60

Hummel J. A., Pawlik A. H., Milosavljević M., Bromm V., 2012, ApJ, 755, 72

Iwamoto N., Umeda H., Tominaga N., Nomoto K., Maeda K., 2005, Science, 309, 451

Jonker P. et al., 2013, ArXiv: 1306.2336

Kawai N. et al., 2006, Nature, 440, 184

Kennicutt R. C., Evans N. J., 2012, ARA&A, 50, 531

Kirby E. N., Simon J. D., Geha M., Guhathakurta P., Frebel A., 2008, ApJ, 685, L43

Kistler M. D., Yüksel H., Beacom J. F., Hopkins A. M., Wyithe J. S. B., 2009, ApJ, 705, L104

Kulkarni G., Hennawi J. F., Rollinde E., Vangioni E., 2014, ApJ, 787, 64

Kulkarni G., Rollinde E., Hennawi J. F., Vangioni E., 2013, ApJ, 772, 93

Laporte N., Infante L., Troncoso Iribarren P., Zheng W., Molino A., 14 co-authors, 2016, ApJ, 820, 98

Larson R. B., 1998, MNRAS, 301, 569

Le Floc'h E., Charmandaris V., Forrest W. J., Mirabel I. F., Armus L., Devost D., 2006, ApJ, 642, 636

Ledoux C., Vreeswijk P. M., Smette A., Fox A. J., Petitjean P., Ellison S. L., Fynbo J. P. U., Savaglio S., 2009, A&A, 506, 661

Madau P., Dickinson M., 2014, ARA&A, 52, 415

Maio U., Ciardi B., Dolag K., Tornatore L., Khochfar S., 2010, MNRAS, 407, 1003

Maio U., Ciardi B., Müller V., 2013a, MNRAS, 435, 1443

Maio U., Dolag K., Ciardi B., Tornatore L., 2007, MNRAS, 379, 963

Maio U., Dolag K., Meneghetti M., Moscardini L., Yoshida N., Baccigalupi C., Bartelmann M., Perrotta F., 2006, MNRAS, 373, 869

Maio U., Dotti M., Petkova M., Perego A., Volonteri M., 2013b, ApJ, 767, 37

Maio U., Iannuzzi F., 2011, MNRAS, 415, 3021

Maio U., Khochfar S., 2012, MNRAS, 421, 1113

Maio U., Koopmans L. V. E., Ciardi B., 2011, MNRAS, 412, L40

Maio U., Petkova M., De Lucia G., Borgani S., 2016, MNRAS, 460, 3733

Maio U., Salvaterra R., Moscardini L., Ciardi B., 2012, MNRAS, 426, 2078

Maio U., Tescari E., 2015, MNRAS, 453, 3798

Maio U., Viel M., 2015, MNRAS, 446, 2760

Mancini M., Schneider R., Graziani L., Valiante R., Dayal P., Maio U., Ciardi B., 2016, MNRAS, 462, 3130

Mancini M., Schneider R., Graziani L., Valiante R., Dayal P., Maio U., Ciardi B., Hunt L. K., 2015, MNRAS, 451, L70

Mancuso C., Lapi A., Shi J., Gonzalez-Nuevo J., Aversa R., Danese L., 2016, ApJ, 823, 128

Maoz D., Mannucci F., 2012, PASA, 29, 447

Marri S., White S. D. M., 2003, MNRAS, 345, 561

McKee C. F., Tan J. C., 2008, ApJ, 681, 771

McLure R. J. et al., 2013, MNRAS, 432, 2696

Mészáros P., Rees M. J., 1997, ApJ, 476, 232

Meynet G., Ekström S., Maeder A., 2006, A&A, 447, 623

Morrison S., Kulkarni V. P., Som D., DeMarcy B., Quiret S., Péroux C., 2016, ApJ, 830, 158

Nandra K. et al., 2013, ArXiv:1306.2307

Naoz S., Yoshida N., Gnedin N. Y., 2012, ApJ, 747, 128

Nomoto K., Kobayashi C., Tominaga N., 2013, ARA&A, 51, 457

Nomoto K., Tominaga N., Umeda H., Kobayashi C., Maeda K., 2006, Nuclear Physics A, 777, 424

Oesch P. A. et al., 2013, ApJ, 773, 75

Oesch P. A. et al., 2014, ApJ, 786, 108

Ohkubo T., Umeda H., Maeda K., Nomoto K., Suzuki T., Tsuruta S., Rees M. J., 2006, ApJ, 645, 1352

Pettini M., 2011, Proceedings of the Royal Society of London Series A, 467, 2735

Pontzen A. et al., 2008, MNRAS, 390, 1349

Press W. H., Schechter P., 1974, ApJ, 187, 425

Rafelski M., Wolfe A. M., Prochaska J. X., Neeleman M., Mendez A. J., 2012, ApJ, 755, 89

Rahmati A., Schaye J., Crain R. A., Oppenheimer B. D., Schaller M., Theuns T., 2016, MNRAS, 459, 310

Ricotti M., 2016, MNRAS, 462, 601

Rowan-Robinson M. et al., 2016, MNRAS, 461, 1100

Rydberg C.-E., Zackrisson E., Lundqvist P., Scott P., 2013, MNRAS, 429, 3658

Salvadori S., Ferrara A., 2009, MNRAS, 395, L6

Salvaterra R. et al., 2012, ApJ, 749, 68

Salvaterra R. et al., 2009, Nature, 461, 1258

Salvaterra R., Maio U., Ciardi B., Campisi M. A., 2013, MNRAS, 429, 2718

Schaefer B. E., Pagnotta A., 2012, Nature, 481, 164

Schaye J. et al., 2015, MNRAS, 446, 521

Schaye J., Dalla Vecchia C., 2008, MNRAS, 383, 1210

Schmidt M., 1959, ApJ, 129, 243

Schneider R., Ferrara A., Natarajan P., Omukai K., 2002, ApJ, 571, 30

Simcoe R. A., Sullivan P. W., Cooksey K. L., Kao M. M., Matejek M. S., Burgasser A. J., 2012, Nature, 492, 79

Smith R. J., Iocco F., Glover S. C. O., Schleicher D. R. G., Klessen R. S., Hirano S., Yoshida N., 2012, ApJ, 761, 154

Sparre M. et al., 2014, ApJ, 785, 150

Springel V., 2005, MNRAS, 364, 1105

Springel V., Frenk C. S., White S. D. M., 2006, Nature, 440, 1137

Springel V., Hernquist L., 2003, MNRAS, 339, 289

Stacy A., Bromm V., 2014, ApJ, 785, 73

Stacy A., Pawlik A. H., Bromm V., Loeb A., 2014, MNRAS, 441, 822

Starkenburg E., Oman K. A., Navarro J. F., Crain R. A., Fattahi A., Frenk C. S., Sawala T., Schaye J., 2017, MNRAS, 465, 2212

Starling R. L. C., Willingale R., Tanvir N. R., Scott A. E., Wiersema K., O'Brien P. T., Levan A. J., Stewart G. C., 2013, MNRAS, 431, 3159

Suda T., Aikawa M., Machida M. N., Fujimoto M. Y., Iben, Jr. I., 2004, ApJ, 611, 476

Suda T., Fujimoto M. Y., 2010, MNRAS, 405, 177

Suwa Y., Ioka K., 2011, ApJ, 726, 107

Thielemann F.-K. et al., 2003, Nuclear Physics A, 718, 139

Thielemann F.-K., Brachwitz F., Höflich P., Martinez-Pinedo G., Nomoto K., 2004, New Astronomy Review, 48, 605

Thöne C. C. et al., 2013, MNRAS, 428, 3590

Tolstoy E., Hill V., Tosi M., 2009, ARA&A, 47, 371

Toma K., Sakamoto T., Mészáros P., 2011, ApJ, 731, 127

Toma K., Yoon S.-C., Bromm V., 2016, ssr

Tornatore L., Borgani S., Dolag K., Matteucci F., 2007a, MNRAS, 382, 1050

Tornatore L., Ferrara A., Schneider R., 2007b, MNRAS, 382, 945

Tseliakhovich D., Hirata C., 2010, Phys. Rev. D, 82, 083520

Tumlinson J., 2006, ApJ, 641, 1

Umeda H., Nomoto K., 2003, Nature, 422, 871

Umeda H., Nomoto K., 2005, ApJ, 619, 427

van den Hoek L. B., Groenewegen M. A. T., 1997, A&A Supp., 123, 305

Wang F. Y., Bromm V., Greif T. H., Stacy A., Dai Z. G., Loeb A., Cheng K. S., 2012, ApJ, 760, 27

Wang F. Y., Dai Z. G., 2009, MNRAS, 400, L10

Wei J.-J., Wu X.-F., Melia F., Wei D.-M., Feng L.-L., 2014, MNRAS, 439, 3329

Whalen D. J., Fryer C. L., Holz D. E., Heger A., Woosley S. E., Stiavelli M., Even W., Frey L. H., 2013a, ApJ, 762, L6

Whalen D. J., Joggerst C. C., Fryer C. L., Stiavelli M., Heger A., Holz D. E., 2013b, ApJ, 768, 95

Widrow L. M., Ryu D., Schleicher D. R. G., Subramanian K., Tsagas C. G., Treumann R. A., 2012, ssr, 166, 37

Wise J. H., Abel T., 2008, ApJ, 685, 40

Wise J. H., Demchenko V. G., Halicek M. T., Norman M. L., Turk M. J., Abel T., Smith B. D., 2014, MNRAS, 442, 2560

Wise J. H., Turk M. J., Norman M. L., Abel T., 2012, ApJ, 745, 50

Wolfe A. M., Gawiser E., Prochaska J. X., 2005, ARA&A, 43, 861

Woosley S. E., Weaver T. A., 1995, ApJS, 101, 181

Woźniak P. R., Vestrand W. T., Panaitescu A. D., Wren J. A., Davis H. R., White R. R., 2009, ApJ, 691, 495

Xu H., Wise J. H., Norman M. L., 2013, ApJ, 773, 83

Yajima H., Khochfar S., 2015, MNRAS, 448, 654

Yoshida N., Omukai K., Hernquist L., 2007, ApJ, 667, L117

Yue B., Ferrara A., Salvaterra R., Xu Y., Chen X., 2013, MNRAS, 433, 1556

Zheng W. et al., 2012, Nature, 489, 406

Acknowledgments

I would like to express thanks to the people who help me complete this thesis. Firstly, I would thank my supervisor Benedetta Ciardi. She helped me a lot during my PhD, gave me a lot of suggestions and instructions, and patiently helped me improve the writing of my thesis. Without her, I could not finish my projects and this thesis. The code of simulations used in this thesis is from Umberto Maio, who also helped me to run the simulations and analyse the results. Another collaborator Ruben Salvaterra also gave me a lot of suggestions and comments. I thank them very much. I would also thank MPA directors Pro. Simon White and Pro. Eiichiro Komatsu who allowed me to have my PhD at MPA, especially Eiichiro gave me many very creative ideas for my PhD and also my thesis.

Besides, I would thank the people who help me to have a better life in Munich, especially my office mate Ricard Ardevol, he encouraged me to join in the foreigner groups and also help me to improve my oral English. My Chinese friends Xiaoling Zhang, Yangfang Li, Dong Li, Hailiang Chen, Yu Luo, Shi Shao, Shi Jia, Xiaping Tang and Wenda Zhang also help me to solve a lot problems to live in Germany. Without these friends, I can not enjoy my life in the last three and half years.

Finally, I would also thank my parents and my girlfriend who support me to study and live in a place far away from my hometown.